

¹ SEARCH FOR EXOTIC HIGGS DECAYS TO LIGHT
² NEUTRAL SCALARS IN FINAL STATES WITH
³ BOTTOM QUARKS AND TAU LEPTONS

⁴ KA YU STEPHANIE KWAN

⁵ A DISSERTATION
⁶ PRESENTED TO THE FACULTY
⁷ OF PRINCETON UNIVERSITY
⁸ IN CANDIDACY FOR THE DEGREE
⁹ OF DOCTOR OF PHILOSOPHY

¹⁰ NOT YET RECOMMENDED FOR ACCEPTANCE
¹¹ BY THE DEPARTMENT OF PHYSICS
¹² ADVISER: ISOBEL OJALVO

¹³ MAY 2024

¹⁴

© Copyright by Ka Yu Stephanie Kwan, 2024.

¹⁵

All Rights Reserved

Abstract

Open questions in particle physics may be addressed by the existence of an extended Higgs sector beyond the Standard Model Higgs boson with mass 125 GeV, which was discovered in 2012 at the Large Hadron Collider (LHC) by the CMS and ATLAS experiments. Many properties of a potential extended Higgs sector remain unconstrained by current measurements, making direct searches of exotic Higgs decays a powerful probe of new physics. The decay of the 125 GeV Higgs boson into two light neutral scalar particles ($h \rightarrow aa$) is allowed in extensions of the Standard Model, such as Two Higgs Doublet Models extended with a scalar singlet (2HDM+S). We present a search at CMS for exotic decays of the 125 GeV Higgs boson to two light neutral scalars, which decay to two bottom quarks and two tau leptons ($h \rightarrow aa \rightarrow bb\tau\tau$). This analysis is combined with a different search where the light scalars decay to two bottom quarks and two muons. The results from the $bb\tau\tau$ analysis and the combined analyses are interpreted in 2HDM+S scenarios. In a different extension of the Standard Model, the Two Real Singlet Model (TRSM), the 125 GeV Higgs boson can decay to two light scalars with unequal mass ($h \rightarrow a_1a_2$). This decay has not been searched for to date at CMS. We present ongoing work on a search for $h \rightarrow a_1a_2$, where the a_2 decays into two a_1 , resulting in four bottom quarks and two tau leptons in the final state, in the $\mu\tau_h$ channel of the $\tau\tau$ decay. Such searches for rare processes will directly benefit from the increased datasets that will be generated by the High-Luminosity LHC (HL-LHC), which is scheduled to increase the LHC’s number of simultaneous proton-proton collisions by a factor of five to seven. To contribute to the performance of the CMS Level-1 Trigger in selecting collisions with interesting physics, this thesis presents an upgraded algorithm for reconstructing electrons and photons in the barrel calorimeter, which will use information with higher spatial granularity to distinguish genuine electrons and photons from background.

⁴²

Acknowledgements

⁴³ Placeholder acknowledgements.

⁴⁵ Contents

⁴⁶	Abstract	iii
⁴⁷	Acknowledgements	iv
⁴⁸	List of Tables	xi
⁴⁹	List of Figures	xiii
⁵⁰	1 Introduction	1
⁵¹	1.1 History of the Standard Model	1
⁵²	1.2 The Standard Model as a gauge theory	3
⁵³	1.3 The Higgs Mechanism	6
⁵⁴	1.4 Two-Higgs Doublet Models	8
⁵⁵	1.5 Two Real Singlet Model	11
⁵⁶	2 The Large Hadron Collider and the CMS Experiment	15
⁵⁷	2.1 The Large Hadron Collider	16
⁵⁸	2.2 Luminosity and pile-up	17
⁵⁹	2.3 The High-Luminosity LHC	20
⁶⁰	2.4 The CMS Detector	21
⁶¹	2.5 Sub-detectors of CMS	23
⁶²	2.5.1 Inner tracking system	23
⁶³	2.5.2 ECAL	24
⁶⁴	2.5.3 HCAL	25

65	2.5.4 Muon detectors	27
66	2.5.5 The Level-1 Trigger	28
67	2.5.6 The High-Level Trigger	32
68	2.5.7 Particle reconstruction	33
69	2.5.8 Data storage and computational infrastructure	34
70	3 The Phase-2 Upgrade of CMS	35
71	3.1 The High-Luminosity LHC	35
72	3.2 The Phase-2 Level-1 Trigger	36
73	3.3 Standalone Barrel Calorimeter electron/photon reconstruction	39
74	3.3.1 Phase-2 geometry of the ECAL Barrel trigger	40
75	3.3.2 Phase-2 electron/photon reconstruction algorithm	40
76	4 Datasets and Monte Carlo samples	49
77	4.1 Datasets used	49
78	4.2 Monte Carlo samples	50
79	4.3 Embedded samples	51
80	5 Object reconstruction and corrections applied	54
81	5.1 Object reconstruction	55
82	5.1.1 Taus	55
83	5.1.2 Muons	58
84	5.1.3 Electrons	59
85	5.1.4 Jets	61
86	5.1.5 B-flavored jets	62
87	5.2 Reconstruction of the $\tau\tau$ mass	63
88	5.2.1 Original SVFit “standalone”: maximum likelihood	64
89	5.2.2 “Classic SVFit” with matrix element	65
90	5.2.3 FastMTT: optimized SVFit	65

91	5.3 Corrections applied to simulation	66
92	5.3.1 Tau energy scale	67
93	5.3.2 Muon energy scale	68
94	5.3.3 Electron energy scale	68
95	5.3.4 τ_h identification efficiency	68
96	5.3.5 Trigger efficiencies	69
97	5.3.6 Tau trigger efficiencies	70
98	5.3.7 Single muon trigger efficiencies	71
99	5.3.8 Single electron trigger efficiencies	72
100	5.3.9 $e\mu$ cross-trigger efficiencies	73
101	5.3.10 Electrons and muons faking τ_h : energy scales	74
102	5.3.11 Electrons and muons faking τ_h : misidentification efficiencies .	75
103	5.3.12 Electron ID and tracking efficiency	76
104	5.3.13 Muon ID, isolation, and tracking efficiencies	76
105	5.3.14 Recoil corrections	78
106	5.3.15 Drell-Yan corrections	79
107	5.3.16 Pile-up reweighing	79
108	5.3.17 Pre-firing corrections	80
109	5.3.18 Top p_T spectrum reweighing	80
110	5.3.19 B-tagging efficiency	80
111	5.3.20 Jet energy resolution and jet energy smearing	81
112	6 Event selection	82
113	6.1 General procedure for all channels	82
114	6.2 Event selection in the $\mu\tau_h$ channel	84
115	6.3 Event selection in the $e\tau_h$ channel	86
116	6.4 Event selection in the $e\mu$ channel	88
117	6.5 Extra lepton vetoes in all channels	89

¹¹⁸	7 Background estimation	92
¹¹⁹	7.1 Z+jets	92
¹²⁰	7.2 W+jets	93
¹²¹	7.3 $t\bar{t}$ + jets	93
¹²²	7.4 Single top	94
¹²³	7.5 Diboson	94
¹²⁴	7.6 Standard Model Higgs	94
¹²⁵	7.7 Jet faking τ_h	95
¹²⁶	7.8 QCD multijet background	96
¹²⁷	8 Systematic uncertainties	98
¹²⁸	8.1 Uncertainties in the lepton energy scales	99
¹²⁹	8.2 Uncertainties from other lepton corrections	100
¹³⁰	8.3 Uncertainties from jet energy scale and resolution	101
¹³¹	8.4 Uncertainties from b-tagging scale factors	102
¹³²	8.5 Uncertainties from MET	102
¹³³	8.6 Uncertainties associated with samples used	102
¹³⁴	8.7 Other uncertainties	103
¹³⁵	8.8 Pulls and impacts	104
¹³⁶	9 Event categorization and signal extraction	106
¹³⁷	9.1 B-tag jet multiplicity	106
¹³⁸	9.2 DNN-based event categorization	107
¹³⁹	9.3 Methodology for signal extraction	109
¹⁴⁰	9.3.1 Model building and parameter estimation	110
¹⁴¹	9.3.2 Hypothesis testing	112
¹⁴²	9.3.3 Confidence intervals	113
¹⁴³	9.3.4 Profile likelihood ratio	114

¹⁴⁴	9.3.5 Modified frequentist method: CL_S	116
¹⁴⁵	10 Results	117
¹⁴⁶	10.1 Results from $bb\tau\tau$	117
¹⁴⁷	10.2 Combination with $bb\mu\mu$ final state	119
¹⁴⁸	11 Asymmetric exotic Higgs decays	130
¹⁴⁹	11.1 Signal masses	130
¹⁵⁰	11.2 Cascade scenario signal studies	131
¹⁵¹	11.3 Current control plots for $\mu\tau_h$ channel	133
¹⁵²	12 Conclusion and outlook	137

¹⁵³ List of Tables

¹⁵⁴	4.1	Expected event composition after selecting two muons in the embedded technique, before additional cuts (i.e. inclusive), and after adding a requirement on the di-muon mass $m_{\mu\mu} > 70$ GeV, or a requirement on the number of b-tag jets in the event.	53
¹⁵⁵			
¹⁵⁶			
¹⁵⁷			
¹⁵⁸	5.1	Energy scales applied to genuine hadronic tau decays τ_h by data-taking year/era and decay mode, along with systematic errors.	67
¹⁵⁹			
¹⁶⁰	5.2	Energy scales and systematic errors applied to genuine muons.	68
¹⁶¹			
¹⁶²	5.3	Energy scales and systematic errors applied to electrons in embedded samples by data-taking year/era.	68
¹⁶³			
¹⁶⁴	5.4	Tau ID efficiency for the DeepTau vs. jet medium working point, with central, up, and down values for 2018, binned in the tau p_T	69
¹⁶⁵			
¹⁶⁶	5.5	Energy scales and up/down systematic uncertainties applied to electrons misidentified as hadronic taus.	74
¹⁶⁷			
¹⁶⁸	5.6	Tau mis-identification efficiency for the DeepTau Tight and Very Loose (VLoose) working points vs. muons in 2018.	75
¹⁶⁹			
¹⁷⁰	5.7	Tau mis-identification efficiency for the DeepTau Tight and Very Loose (VLoose) working points vs. electrons in 2018.	75

171	6.1	Trigger thresholds used for the leptons in the $bb\mu\mu$ analysis and the 172 $bb\tau\tau$ analysis (the focus of this work). The thresholds for the three $bb\tau\tau$ 173 channels ($e\mu$, $e\tau_h$, and $\mu\tau_h$) are listed separately, with some channels 174 and years taking the logical OR of two triggers with different thresholds.	84
175	6.2	Summary of requirements applied to the leptons in the $bb\mu\mu$ analysis 176 and the $bb\tau\tau$ analysis (the focus of this work). $\Delta R = \sqrt{(\Delta\eta)^2 + (\Delta\phi)^2}$ 177 is a measure of spatial separation. Relative isolation is defined in 178 Eqn. 5.2Muonsequation.5.1.2 and Section 5.1.2Muonssubsection.5.1.2. 179 The b-tag jets are required to pass the listed DeepFlavour working 180 points (WP), which are described in Section 5.1.5B-flavored jetssub- 181 section.5.1.5. In the $bb\tau\tau$ analysis, the required $ \eta $ of the hadronic 182 taus are listed for the single and cross triggers respectively. The $bb\mu\mu$ 183 analysis requires two b-tag jets in all events, while the $bb\tau\tau$ analysis 184 only requires one.	85
185	6.3	High-Level Trigger (HLT) paths used to select data and simulation 186 events in 2016 for the three $\tau\tau$ channels.	89
187	6.4	High-Level Trigger (HLT) paths used to select data and simulation 188 events in 2017 for the three $\tau\tau$ channels.	90
189	6.5	High-Level Trigger (HLT) paths used to select data and simulation 190 events in 2018 for the three $\tau\tau$ channels. In 2018 a HLT trigger path 191 using the hadron plus strips (HPS) tau reconstruction algorithm be- 192 came available.	91
193	9.1	Event categorization based on DNN scores for events with exactly 1 194 b-tag jet (1bNN), for the three $\tau\tau$ channels and three eras.	109
195	9.2	Event categorization based on DNN scores for events with 2 b-tag jets 196 (2bNN), for the three $\tau\tau$ channels and three eras.	110

¹⁹⁷ List of Figures

¹⁹⁸ 1.1	Table of Standard Model particles showing the grouping of the fermions into three generations of matter and the bosons, responsible for carrying the three fundamental forces in the Standard Model. The masses, charges, and spins of the particles are shown. The antimatter counter- parts of the fermions are not shown. The possible interactions between the fermions and gauge bosons are highlighted.	3
²⁰⁴ 1.2	An illustration of the Higgs potential.	8
²⁰⁵ 1.3	Branching ratios of a singlet-like pseudoscalar in Type II 2HDM+S for $\tan \beta = 0.5$ (left) and $\tan \beta = 5$ (right).	11
²⁰⁷ 1.4	Benchmark plane BP1 for benchmark scenario 1, for the decay signa- ture $h_{125} \rightarrow h_1 h_2$ with $h_{125} \equiv h_3$, defined in the (M_1, M_2) plane. . . .	14
²⁰⁹ 2.1	Aerial view of the Large Hadron Collider (LHC).	18
²¹⁰ 2.2	Distribution of the mean number of inelastic collisions per bunch cross- ing (pile-up) in data, for proton-proton collisions in 2016-2018 . . .	20
²¹² 2.3	Sketch of particle trajectories of muons, electrons, charged and neutral hadrons, and photons in a transverse cross-section of the CMS detector.	22
²¹⁴ 2.4	Cross section of the current Phase-1 CMS tracker.	24
²¹⁵ 2.5	Longitudinal view of the CMS detector showing the hadron calorimeter barrel (HB), endcap (HE), outer (HO), and forward (HF) calorimeters.	26

217	2.6	Layout of the CMS barrel muon drift tube (DT) chambers in one of the five wheels.	28
219	2.7	Dataflow for the Phase-1 Level-1 Trigger.	29
220	2.8	Schematic of the calorimeter trigger after Long Shutdown 2. The Layer-1 calorimeter trigger is implemented in CTP7 cards, which send time-multiplexed outputs to the Layer-2 MP7 cards. The Layer-2 cards handle the data in a round-robin style and the outputs are de- multiplexed, producing one output data stream to the Global Trigger.	31
224			
225	3.1	Functional diagram of the CMS L1 Phase-2 upgraded trigger design. .	37
226	3.2	Summary of the links between the trigger primitives, the trigger ob- jects, the Level-1 algorithms, and the physics channels in the Phase-2 menu.	39
227			
229	3.3	Schematic of the geometry of the Phase-2 ECAL barrel in the Regional Calorimeter Trigger (RCT), showing the division of the barrel region into 36 Regional Calorimeter Trigger (RCT) cards (<i>red</i>). Each card spans 17×4 towers in $\eta \times \phi$ (<i>green</i>), and each tower is 5×5 in single crystals in $\eta \times \phi$. Towers in the overlap region (<i>shaded yellow</i>) are read out to both the barrel and endcap.	43
231			
232	3.4	Schematic of two example RCT cards in the negative eta (<i>top</i>) and positive eta (<i>center</i>) regions of the ECAL barrel. Each RCT card is divided into five regions: four regions are of size 3×4 towers in $\eta \times \phi$ (<i>bottom left</i>), and a fifth smaller overlap region of size 2×4 towers (<i>bottom right</i>). Each tower is 5×5 ($\eta \times \phi$) in crystals.	44
234			
235			
236			
237			
238			
239			

240	3.5 Schematic of the Phase-2 ECAL barrel in the Global Calorimeter Trig-	
241	ger (GCT), which will process the outputs of the Regional Calorimeter	
242	Trigger (RCT) in three cards (<i>magenta highlights</i>). Each card in the	
243	GCT processes the equivalent of sixteen RCT cards, with the center	
244	twelve being unique to that GCT card (<i>shaded pink</i>), and the remain-	
245	ing four processed in overlap with the other GCT cards.	45
246	3.6 Illustration of an example electron/photon (e/γ) cluster in the Phase-	
247	2 Level-1 Trigger standalone barrel e/γ reconstruction, in a region of	
248	15×20 crystals (3×4 towers). Each small pink square is one crystal,	
249	the highest-granularity ECAL trigger primitives available to the L1	
250	Trigger in Phase-2. The core cluster consists of the energy sum in a	
251	3×5 window of crystals, (<i>shaded light blue</i>) centered around the seed	
252	crystal (<i>red</i>). Bremsstrahlung corrections are checked in the adjacent	
253	3×5 windows in the ϕ direction (<i>shaded light yellow</i>). The relative	
254	energies in windows of size 2×5 and 5×5 in crystals (<i>dashed dark blue</i>	
255	<i>and dark red</i>) are used to compute shower shape variables to identify	
256	true e/γ objects. Lastly, an isolation sum is computed in a window of	
257	size 7×7 in towers (not shown in figure).	46
258	3.7 Efficiency of the standalone barrel e/γ reconstruction, as a function of	
259	the true electron's transverse momentum p_T	47
260	3.8 Rates of the standalone barrel e/γ reconstruction measured as a func-	
261	tion of the minimum energy (E_T) required of the reconstructed e/γ	
262	object in each event.	48
263	4.1 Cumulative delivered and recorded luminosity versus time for 2015-	
264	2018 at CMS, in proton-proton collision data only, at nominal center-	
265	of-mass energy.	50

266	4.2	Schematic view of the four main steps of the embedding technique for				
267		τ leptons.	52			
268	5.1	Distributions of $m_{\tau\tau}$ reconstructed by the classic SVFit algorithm, and				
269		masses of visible tau decay products (before SVFit).	66			
270	5.2	Electron/photon energy scale factors and uncertainties for 2018. . . .	69			
271	5.3	Hadronic tau leg efficiency of the cross-triggers for $\mu\tau_h$ (<i>left</i>) and $e\tau_h$ (<i>right</i>) triggers as a function of offline tau p_T for 2016, 2017, and 2018.	71			
273	5.4	Trigger efficiencies in data (<i>top panels</i>) and ratio of efficiencies af- ter/before a HLT muon reconstruction update (<i>bottom panels</i>) for the				
275		muon in the isolated single muon trigger with threshold $p_T > 24$ GeV				
276		in the data-taking year 2018, as functions of the muon p_T (<i>left</i>) and				
277		muon $ \eta $ (<i>right</i>).	72			
278	5.5	Trigger efficiencies in data and the data/MC ratio for the electron in				
279		the single electron trigger with threshold $p_T > 32$ GeV in the data- taking year 2018, as functions of the electron p_T (<i>left</i>) and electron $ \eta $				
281		(<i>right</i>).	73			
282	5.6	Efficiencies of the electron leg vs. p_T (<i>left</i>) and the muon log vs. η (<i>right</i>), for the HLT path with online thresholds of 12 GeV for the				
283		electron and 23 GeV for the muon, with the data-taking years 2016				
284		through 2018 overlaid.	74			
286	5.7	Efficiencies in data (<i>top panels</i>) and the ratio of efficiencies in data/MC (<i>bottom panels</i>), for the electron multivariate analysis (MVA) identifi- cation (<i>left</i>) and for the Gaussian-sum filter (GSF) tracking (<i>right</i>). .	76			
288	5.8	Muon identification efficiencies in 2015 data and MC as a function of				
290		the muon p_T for the loose ID (<i>left</i>) and tight ID (<i>right</i>) working points.	77			
291	5.9	Muon isolation efficiencies in Run-2 data as a function of the muon p_T (<i>left</i>) and $ \eta $ (<i>right</i>).	78			

293	5.10 Muon tracking efficiencies as a function of $ \eta $ for standalone muons in	
294	Run-2 data (<i>black</i>) and Drell-Yan (<i>blue</i>) MC simulation.	79
295	7.1 Leading-order Feynman diagrams of Higgs production.	95
296	8.1 Top sixty pulls and impacts for the combination of all channels and	
297	years.	105
298	9.1 Schematic of the Neyman construction for confidence intervals.	115
299	10.1 Postfit final observed and expected $m_{\tau\tau}$ distributions in the $\mu\tau_h$ chan-	
300	nel, for the 1 b-tag jet and 2 b-tag jet signal and control regions.	121
301	10.2 Postfit final observed and expected $m_{\tau\tau}$ distributions in the $e\tau_h$ chan-	
302	nel, for the 1 b-tag jet and 2 b-tag jet signal and control regions.	122
303	10.3 Postfit final observed and expected $m_{\tau\tau}$ distributions in the $e\mu$ channel.	123
304	10.4 Observed 95% CL exclusion limits (<i>black, solid lines</i>) and expected 95%	
305	CL and 68% CL limits (<i>shaded yellow and green</i>) on the branching	
306	fraction $B(h \rightarrow aa \rightarrow bb\tau\tau)$ in percentages, assuming the Standard	
307	Model production for the 125 GeV Higgs (h). Limits are shown for the	
308	$\mu\tau_h$ channel (<i>top left</i>), the $e\tau_h$ channel (<i>top right</i>), and the $e\mu$ channel	
309	(<i>bottom left</i>), and lastly the combination of all three channels (<i>bottom</i>	
310	<i>right</i>) The dataset corresponds to 138 fb^{-1} of data collected in the	
311	years 2016-2018 at a center-of-mass energy 13 TeV.	124
312	10.5 Observed 95% CL upper limits on $B(h \rightarrow aa)$ in %, for the $bb\tau\tau$ final	
313	state (<i>left</i>) and $bb\mu\mu$ final state (<i>right</i>) using the full Run 2 integrated	
314	luminosity of 138 fb^{-1} in 2HDM+S type I (<i>blue</i>), type II with $\tan\beta =$	
315	2.0 (<i>orange dashed</i>), type III with $\tan\beta = 2.0$ (<i>dotted green</i>), and type	
316	IV with $\tan\beta = 0.6$ (<i>red dashed</i>).	125

317	10.6 Observed 95% CL upper limits on the branching fraction of the 125	
318	GeV Higgs boson to two pseudoscalars, $B(h \rightarrow aa)$, in percentages,	
319	as a function of the pseudoscalar mass m_a , in 2HDM+S type I (<i>blue</i>),	
320	type II with $\tan\beta = 2.0$ (<i>orange dashed</i>), type III with $\tan\beta = 2.0$	
321	(<i>dotted green</i>), and type IV with $\tan\beta = 0.6$ (<i>red dashed</i>), for the	
322	combination of $bb\mu\mu$ and $bb\tau\tau$ channels using the full Run 2 integrated	
323	luminosity of 138 fb^{-1}	126
324	10.7 Observed 95% CL upper limits on $\mathcal{B}(h \rightarrow aa)$ in %, for the combination	
325	of $bb\mu\mu$ and $bb\tau\tau$ channels using the full Run 2 integrated luminosity	
326	of 138 fb^{-1} for Type II (<i>left</i>), Type III (<i>middle</i>), and Type IV (<i>right</i>)	
327	2HDM+S in the $\tan\beta$ vs. m_a phase space.	127
328	10.8 Summary plot of current observed and expected 95% CL limits on the	
329	branching ratio of the 125 GeV Higgs boson to two pseudoscalars, nor-	
330	malized to the Standard Model Higgs production cross-section, $\frac{\sigma(h)}{\sigma_{\text{SM}}} \times$	
331	$B(h \rightarrow aa)$, in the 2HDM+S type I scenario, obtained at CMS with	
332	data collected at 13 TeV.	127
333	10.9 Summary plot of current observed and expected 95% CL limits on the	
334	branching ratio of the 125 GeV Higgs boson to two pseudoscalars, nor-	
335	malized to the Standard Model Higgs production cross-section, $\frac{\sigma(h)}{\sigma_{\text{SM}}} \times$	
336	$B(h \rightarrow aa)$, in the 2HDM+S type II scenario with $\tan\beta = 2.0$, ob-	
337	tained at CMS with data collected at 13 TeV.	128
338	10.10 Summary plot of current observed and expected 95% CL limits on the	
339	branching ratio of the 125 GeV Higgs boson to two pseudoscalars, nor-	
340	malized to the Standard Model Higgs production cross-section, $\frac{\sigma(h)}{\sigma_{\text{SM}}} \times$	
341	$B(h \rightarrow aa)$, in the 2HDM+S type III scenario with $\tan\beta = 2.0$, ob-	
342	tained at CMS with data collected at 13 TeV.	129

343	11.1 Generator-level b-flavor jet transverse momenta p_T , for $h \rightarrow a_1 a_2$ cas-	
344	cade scenario in the $4b2\tau$ final state, for mass hypotheses $(m_{a_1}, m_{a_2}) =$	
345	$(100, 15)$ GeV (<i>left</i>) and $(40, 20)$ GeV (<i>right</i>). In each plot the generator-	
346	level p_T of the leading (<i>black</i>), sub-leading (<i>red</i>), third (<i>blue</i>), and	
347	fourth (<i>light green</i>) are overlaid.	132
348	11.2 Distributions (arbitrary units) of transverse momentum p_T resolution	
349	and ΔR between the two closest generator-level b jets, treated as one	
350	object, and the nearest reconstructed AK4 jet, for two different $h \rightarrow$	
351	$a_1 a_2$ mass hypotheses $(m_{a_1}, m_{a_2}) = (100, 15)$ GeV (<i>top left, top right</i>)	
352	and $(40, 20)$ GeV (<i>bottom left, bottom right</i>) in the ggH production of	
353	the 125 GeV h . In the $(40, 20)$ GeV mass point, the longer p_T resolution	
354	tail (<i>bottom left</i>) indicates that the reconstructed jet underestimates	
355	the generator b-flavor jets' energy, and the significant fraction of events	
356	with larger ΔR values (<i>bottom right</i>) indicate worse matching.	133
357	11.3 Kinematic properties of the leading muon and τ_h in the $\mu\tau_h$ channel: p_T	
358	(<i>top row</i>), η (<i>second row</i>), and ϕ (<i>third row</i>). The visible 4-momenta	
359	of the muon and τ_h are summed, giving the visible di-tau mass m_{vis}	
360	and transverse momentum $p_{T,\text{vis}}$. The errors shown in the figures only	
361	include statistical errors and only several of the full set of systematic	
362	errors (only those associated with the lepton energy scales and τ_h iden-	
363	tification efficiency).	135
364	11.4 Kinematic properties of the leading and sub-leading b-tag jets in the	
365	$\mu\tau_h$ final state: jet p_T (<i>top row</i>), η (<i>second row</i>), ϕ (<i>third row</i>), as well	
366	as the missing transverse energy magnitude and azimuthal direction	
367	(<i>bottom row</i>). The errors shown in the figures only include statistical	
368	errors and only several of the full set of systematic errors (only those	
369	associated with the lepton energy scales and τ_h identification efficiency).	136

³⁷⁰ Chapter 1

³⁷¹ Introduction

³⁷² The Standard Model is the current prevailing theoretical framework that encompasses
³⁷³ all known elementary particles to date and describes their interactions, yet falls short
³⁷⁴ of describing open problems in physics. Here, we describe the history of the Standard
³⁷⁵ Model and its particle content (Section 1.1), and provide a mathematical motivation of
³⁷⁶ the SM as a gauge theory (Section 1.2). We introduce the Higgs mechanism (Section
³⁷⁷ 1.3), and outline two groups of theoretical extensions to the Standard Model that
³⁷⁸ feature extended Higgs sectors (Sections 1.4 and 1.5).

³⁷⁹ 1.1 History of the Standard Model

³⁸⁰ The building blocks of our modern-day understanding of particle physics were estab-
³⁸¹ lished over the course of many decades by experimental discoveries and theoretical
³⁸² advances, culminating in the development of a theoretical framework known as the
³⁸³ Standard Model (SM). In the 1880s, the electron was the first subatomic particle to
³⁸⁴ be identified, through measurements of particles produced by ionizing gas. By the
³⁸⁵ 1930s, atoms were known to consist mostly of empty space, with protons and neutrons
³⁸⁶ concentrated at the center and orbited by electrons. Spurred by advances in parti-
³⁸⁷ cle accelerator technology, the experimental discoveries of the positron, the muon,

and the pion, painted an increasingly complicated picture of particle physics that could not be described solely with atomic physics [1]. Quantum field theory (QFT) began to be developed in the early 20th century as an extension of the conceptual framework of quantum mechanics to electromagnetic fields [2]. In 1927, Dirac coined the name quantum electrodynamics (QED), which was the first part of QFT that was developed. QED quantized the electromagnetic field and supplied a relativistic theory of the electron, and could be applied to concrete physical processes such as the scattering of high-frequency photons by free electrons (Compton scattering), and the production of electron-positron pairs by photons [2]. In the 1940s the QED-only picture was challenged by the realization that the four-fermion theory of weak interactions had infinities at higher orders of perturbation theory which could not be removed via the technique of renormalization [3], i.e. shifting divergences into parts of the theory that do not influence empirical measurements [2].

In the 1950s and 1960s, QFT was extended to describe not only the electromagnetic force, but also the strong and weak force, with the final picture forming the Standard Model. This took place in the development and maturation of three principles: the quark model, the idea of gauge (or local) symmetry, and spontaneously broken symmetry [3]. In the fully fledged QFT, Lagrangians had to be formed that contained new classes of quantum fields, or particles [2].

The particle content of the Standard Model is summarized in Fig. 1.1. Particles are grouped into fermions, which comprise all known matter, and bosons, which mediate the interactions between particles. Fermions consist of quarks and leptons, and are grouped into three generations. For example, the electron belongs to the first generation of leptons. The second and third generation counterparts of the electron are the muon and the tau lepton, and are over 200 and 30,000 times heavier than the electron respectively. The quarks are also organized into three generations (top and bottom quarks, charm and strange quarks, and up and down quarks), and

415 carry fractional electric charge. Bosons are force carriers; the interaction of fermions
416 with bosons corresponds to fundamental forces. The Standard Model describes the
417 electromagnetic force, the strong nuclear force, and the weak nuclear force. Through
418 the strong force, quarks can form composite particles known as hadrons. Familiar
419 examples of hadrons are the protons and neutrons in the nucleus of an atom.

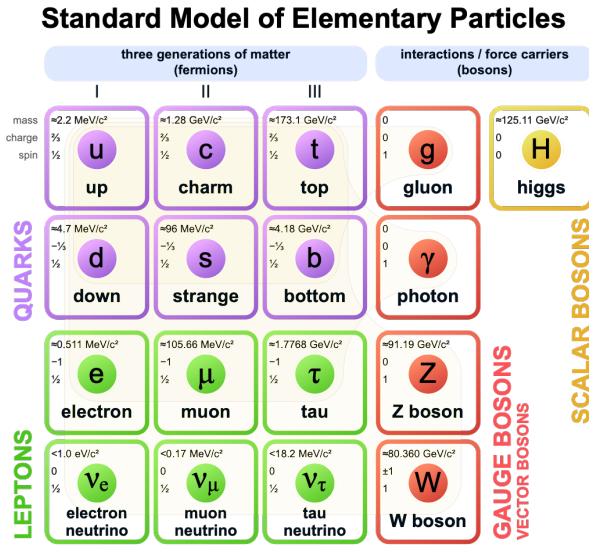


Figure 1.1: Table of Standard Model particles showing the grouping of the fermions into three generations of matter and the bosons, responsible for carrying the three fundamental forces in the Standard Model. The masses, charges, and spins of the particles are shown. The antimatter counterparts of the fermions are not shown. The possible interactions between the fermions and gauge bosons are highlighted.

1.2 The Standard Model as a gauge theory

421 In this section we lay the theoretical foundations of the Standard Model as a gauge
422 theory, starting from the principle of gauge invariance (gauge symmetry), with local
423 gauge symmetries giving rise to interactions between particles.

⁴²⁴ Gauge theories of elementary particle interactions originate from a freedom of
⁴²⁵ choice in the mathematical description of particle fields which has no effect on the
⁴²⁶ particles' physical states [4]. The existence and form of the particles' interactions,

427 can be deduced from the existence of physically indeterminate, gaugable quantities.

428 An example of this gauge invariance is classical physics is the electromagnetic
429 interaction, where the fundamental field is the four-vector potential A^μ [4]. The
430 physical electromagnetic fields and Maxwell's equations arise from the elements of
431 the tensor $F_{\mu\nu}(x) = \partial_\mu A_\nu(x) - \partial_\nu A_\mu(x)$. Any two choices of A^μ that are related by a
432 transformation of the form

$$A_\mu \rightarrow A_\mu + \partial_\mu \alpha \quad (1.1)$$

433 for any real, differentiable function $\alpha(x)$, describe the same physical configuration,
434 and has no effect on Maxwell's equations. This "redundancy" in the choice of gauge
435 in Eqn. 1.1 is called a gauge symmetry.

436 One important consequence of gauge symmetry comes from the application of
437 Noether's theorem, which states that for every global transformation under which the
438 Lagrangian density is invariant, there exists a conserved quantity. If $\mathcal{L}(\Psi(x), \partial_\mu \Psi(x))$
439 is invariant under the transformation of the wave function $\Psi(x) \rightarrow \Psi'(x)$, where
440 $\Psi'(x) = \Psi(x) + \delta\Psi(x)$, then there exists a conserved current

$$\partial_\mu \left(\frac{\partial \mathcal{L}(x)}{\partial (\partial_\mu \Psi(x))} \delta\Psi(x) \right) = 0 \quad (1.2)$$

441 In classical mechanics, the conservation of linear momentum, angular momentum,
442 and energy follows from translational invariance, rotational variance, and invariance
443 under translations in time [4]. Likewise, charge conservation can be shown to arise
444 from the invariance of the Dirac Lagrangian density $\mathcal{L}_{\text{Dirac}} = \bar{\Psi}(i\gamma^\mu \partial_\mu - m)\Psi$ under the
445 particle wavefunction's phase transformation, $\Psi'(x) = \exp(i\epsilon\chi)\Psi(x)$. Thus Noether's
446 theorem establishes a correspondence between a gauge symmetry and a conserved
447 internal property (e.g. charge or momentum).

448 Interactions between particles arise if we modify the wave function with a phase

449 transformation $\Psi'(x) = \exp(ie\chi)\Psi(x)$, and allow the phase χ to be a function of
450 spacetime [4]. A wave function of the form

$$\Psi'(x) = \exp(ie\chi(x))\Psi(x) \quad (1.3)$$

451 can be verified to *not* be a solution to the Dirac equation for free particles: $(i\gamma^\mu\partial_\mu -$
452 $m)\Psi(x) = 0$. This necessitates a modified Dirac equation, where the derivative takes
453 into account that the vector field $V(x)$ needs to be compared at two displaced space-
454 time points in a curvilinear coordinate system:

$$\mathcal{D}_\mu \equiv \lim_{\Delta x^\mu \rightarrow 0} \frac{V_{||}(x + \Delta x) - V(x)}{\Delta x^\mu} \quad (1.4)$$

455 We define a covariant derivative,

$$D_\mu = \partial_\mu + ieA_\mu \quad (1.5)$$

456 where $A_\mu(x)$ is a 4-vector potential. Thus the modified Dirac equation reads:

$$(i\gamma^\mu\mathcal{D}_\mu - m)\Psi(x) = 0 \quad (1.6)$$

457 The simultaneous gauge transformation $A'_\mu(x) = A_\mu(x) - \partial_\mu\chi(x)$ and wavefunction
458 transformation $\Psi'(x) = \exp(ie\chi(x))\Psi(x)$ leaves the covariant-derivative form of the
459 Dirac equation (Eqn 1.1) invariant.

460 The generalization of this result is as follows: if a theory is invariant for unitary
461 transformations U of the particle states according to

$$\Psi' = U\Psi \quad (1.7)$$

462 One must define a derivative of the form

$$D^\mu = \partial^\mu + igB^\mu \quad (1.8)$$

463 to keep the theory invariant under Eqn. 1.7. The four-potential B^μ represents the
464 interacting four-potential which must be added to keep the theory invariant.

465 In the case of the Standard Model, the theory is built around the gauge trans-
466 formations $G = SU(3) \times SU(2) \times U(1)$. $SU(3)$ is associated to the strong force
467 (subscripted C); $SU(2)$ is associated to the weak force (subscripted L); and $U(1)$ is
468 hypercharge (subscripted Y). The gauge-covariant derivative is

$$\mathcal{D}_\mu = \partial_\mu - ig'B_\mu \frac{Y}{2} - igW_\mu^\alpha \frac{\tau_a}{2} - ig_s G_\mu^k \frac{\lambda_k}{2} \quad (1.9)$$

469 • In the $U(1)_Y$ term, B_μ is the weak hypercharge field.

470 • In the $SU(2)_L$ term, $W_\mu(x) = (W_\mu^1(x), W_\mu^2(x), W_\mu^3(x))$ are a triplet of four-
471 potentials. $\tau/2$ are the Pauli matrices, generators of the $SU(2)$ transformation.

472 • In the $SU(3)_C$ term, the gluon (color) field is G_μ . λ_k are the Gell-Man matrices,
473 generators of the $SU(3)$ transformation.

474 The invariance of the Standard Model under $SU(3)_C \times SU(2)_L \times U(1)_Y$ requires
475 massless fermions and massless force carriers.

476 1.3 The Higgs Mechanism

477 To introduce mass into the theory, i.e. to change the propagation of the gauge par-
478 ticles and all the fermions, the physical vacuum cannot have all the symmetries of
479 the Standard Model Lagrangian [4]. The symmetries of the physical vacuum must
480 be spontaneously broken, without affecting gauge invariance in the Lagrangian. The

481 Higgs mechanism proposes the existence of a scalar field, or fields, with nonzero vac-
 482 um expectation values, which reduce the gauge symmetries of the physical vacuum
 483 from $SU(3)_C \times SU(2)_L \times U(1)_Y$ down to $SU(3)_C \times U(1)_{EM}$.

484 The Higgs field interacts with the gauge bosons and fermions throughout space,
 485 impeding their free propagation. The resulting broken symmetry correctly predicts
 486 the mass ratio of the neutral (Z) and charged (W) massive electroweak bosons, and
 487 predicts that at least one physical degree of freedom in the Higgs field is a particle
 488 degree of freedom, called the Higgs boson. The location of the minimum of the Higgs
 489 potential can be constrained from previously measured Standard Model parameters,
 490 but the shape of the mass distribution of the Higgs boson must be experimentally
 491 measured.

492 The minimal choice of Higgs field comes from the breaking of $SU(2)_L \times U(1)_Y$
 493 down to $U(1)_{EM}$. The smallest $SU(2)$ multiplet is the doublet. The existence of three
 494 massive electroweak bosons leads the Higgs sector to have at least three degrees of
 495 freedom. The minimal single-doublet complex scalar Higgs field is

$$\Phi(x) = \begin{pmatrix} \phi^+(x) \\ \phi^0(x) \end{pmatrix} = \frac{1}{\sqrt{2}} \begin{pmatrix} \phi_1^+(x) + i\phi_2^+(x) \\ \phi_1^0(x) + i\phi_2^0(x) \end{pmatrix} \quad (1.10)$$

496 where ϕ_1^+ , ϕ_2^+ , ϕ_1^0 , and ϕ_2^0 are real (four degrees of freedom). By convention, the
 497 nonzero vacuum expectation value is assigned to ϕ_1^0 .

498 The minimal self-interacting Higgs potential that is invariant under $SU(2)_L \times$
 499 $U(1)_Y$ is given by

$$V(\Phi^\dagger \Phi) = -\mu^2 \Phi^\dagger \Phi + \lambda (\Phi^\dagger \Phi)^2, \quad \mu^2 > 0, \lambda > 0 \quad (1.11)$$

500 where λ is the coupling strength of the four-point Higgs interaction. The potential

501 energy is minimized at

$$\Phi_{\min} = \frac{1}{\sqrt{2}} \begin{pmatrix} 0 \\ v \end{pmatrix}, \text{ where } v = \sqrt{\mu^2/\lambda} \quad (1.12)$$

502 Choosing a fixed orientation of $\langle \Phi \rangle$ out of a continuous set of possible ground states
 503 spontaneously breaks the symmetry of the physical vacuum, as illustrated in Fig 1.2.

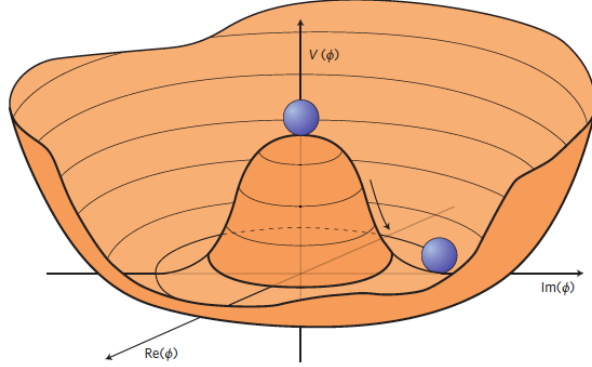


Figure 1.2: An illustration of the Higgs potential [5]. Choosing any of the points at the bottom of the potential breaks spontaneously the rotational $U(1)$ symmetry.

504 The excitations of the Higgs field with respect to the minimum Φ_{\min} are parame-
 505 terized by

$$\Phi(x) = \exp(i\xi(x) \cdot \tau) \frac{1}{\sqrt{2}} \begin{pmatrix} 0 \\ v + H(x) \end{pmatrix} \quad (1.13)$$

506 Three degrees of freedom are coupled directly to the electroweak gauge bosons; this
 507 is often referred to as the gauge bosons “eating” the Goldstone bosons to form the
 508 longitudinal polarizations of the massive spin-1 boson states. The $H(x)$ excitation is
 509 in the radial direction and corresponds to the free particle state of the Higgs boson.

510 1.4 Two-Higgs Doublet Models

511 One of the simplest possible extensions to the Standard Model is adding a doublet
 512 to the minimal Higgs sector of the Standard Model, which is a $SU(2)_L$ doublet H

513 with hypercharge $Y = +\frac{1}{2}$, denoted here as $H \sim 2_{+1/2}$. These extensions are found
514 in several theories such as supersymmetry. A general 2HDM can be extended with a
515 light scalar (2HDM+S) to obtain a rich set of exotic Higgs decays [6].

The charges of the Higgs fields are chosen to be $H_1 \sim 2_{-1/2}$ and $H_2 \sim 2_{+1/2}$, which acquire vacuum expectation values $v_{1,2}$ which are assumed to be real and aligned [6]. Expanding about the minima yields two complex and four real degrees of freedom:

$$H_1 = \frac{1}{\sqrt{2}} \begin{pmatrix} v_1 + H_{1,R}^0 + iH_{1,I}^0 \\ H_{1,R}^- + iH_{1,I}^- \end{pmatrix} \quad (1.14)$$

$$H_2 = \frac{1}{\sqrt{2}} \begin{pmatrix} H_{2,R}^+ + iH_{2,I}^+ \\ v_2 + H_{2,R}^0 + iH_{2,I}^0 \end{pmatrix} \quad (1.15)$$

516 The charged scalar and pseudoscalar mass matrices are diagonalized by a rotation
517 angle β , defined as $\tan \beta = v_2/v_1$. One charged (complex) field and one neutral
518 pseudoscalar combination of $H_{1,2,I}^0$ are eaten by the SM gauge bosons after electroweak
519 symmetry breaking [6]. The other complex field yields two charged mass eigenstates
520 H^\pm , which are assumed to be heavy. The remaining three degrees of freedom yield
521 one neutral pseudoscalar mass eigenstate

$$A = H_{1,I}^0 \sin \beta - H_{2,I}^0 \cos \beta \quad (1.16)$$

522 and two neutral scalar mass eigenstates (where $-\pi/2 \leq \alpha \leq \pi/2$)

$$\begin{pmatrix} h \\ H^0 \end{pmatrix} = \begin{pmatrix} -\sin \alpha & \cos \alpha \\ \cos \alpha & \sin \alpha \end{pmatrix} \begin{pmatrix} H_{1,R}^0 \\ H_{2,R}^0 \end{pmatrix} \quad (1.17)$$

523 We assume that the 2HDM is near or in the decoupling limit: $\alpha \rightarrow \pi/2 - \beta$, where the
524 lightest state in the 2HDM is h , which we identify as the 125 GeV Higgs particle [6].
525 In this limit, the fermion couplings of h become identical to the Standard Model

526 Higgs, while the gauge boson couplings are very close to Standard Model-like for
527 $\tan \beta \gtrsim 5$. All of the properties of h can be determined by just two parameters: $\tan \beta$
528 and α , and the fermion couplings to the two Higgs doublets.

529 2HDM can be extended by a scalar singlet (2HDM+S) [6]:

$$S = \frac{1}{\sqrt{2}}(S_R + iS_I) \quad (1.18)$$

530 If this singlet only couples to the Higgs doublets $H_{1,2}$ and has no direct Yukawa
531 couplings, all of its couplings to SM fermions result from mixing with $H_{1,2}$. Under
532 these simple assumptions, exotic Higgs decays $h \rightarrow ss \rightarrow X\bar{X}Y\bar{Y}$ or $h \rightarrow aa \rightarrow$
533 $X\bar{X}Y\bar{Y}$, and $h \rightarrow aZ \rightarrow X\bar{X}Y\bar{Y}$ are permitted, where $s(a)$ is a (pseudo)scalar mass
534 eigenstate mostly composed of $S_R(S_I)$, and X, Y are Standard Model fermions or
535 gauge bosons. There are two pseudoscalars in the 2HDM+S, and the mostly singlet-
536 like pseudoscalar can be chosen to be the one lighter than the SM-like Higgs. For
537 $m_a < m_h - m_Z \sim 35$ GeV, the exotic Higgs decay $h \rightarrow Za$ is possible, and for
538 $m_a < m_h/2 \approx 63$ GeV, the exotic Higgs decay $h \rightarrow aa$ is possible.

539 In 2HDM, and by extension 2HDM+S, there are four types of fermion couplings
540 commonly discussed in the literature that forbid flavor-changing neutral currents at
541 tree level [6]. These are referred to as Type I (all fermions couple to H_2), Type II
542 (MSSM-like, d_R and e_R couple to H_1 , u_R to H_2), Type III (lepton-specific, leptons
543 and quarks couple to H_1 and H_2 respectively) and Type IV (flipped, with u_R , e_R
544 coupling to H_2 and d_R to H_1). The exact branching ratios of the pseudoscalars to
545 Standard Model particles vary depending on the 2HDM+S model and the value of
546 $\tan \beta$ (e.g. Fig. 1.3).

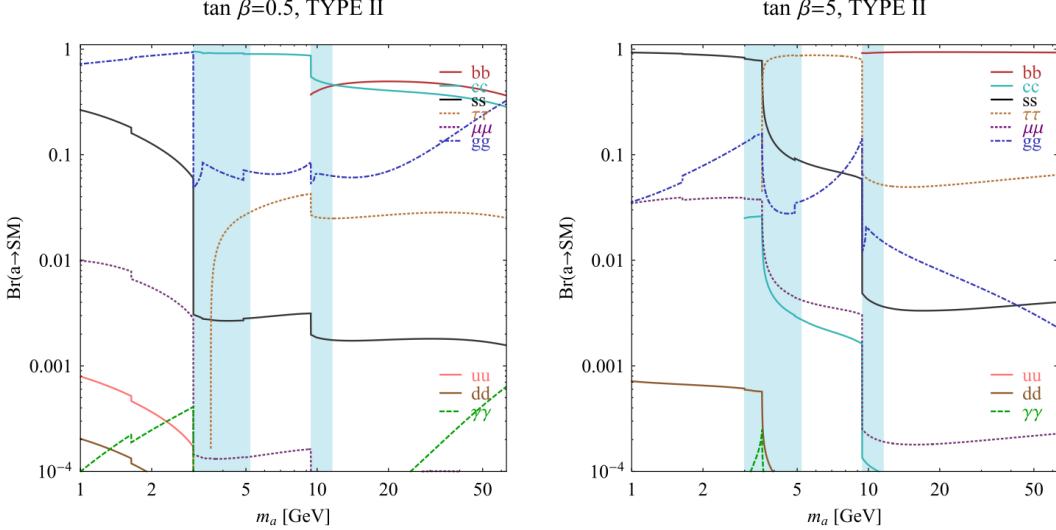


FIG. 7 (color online). Branching ratios of a singletlike pseudoscalar in the 2HDM + S for type-II Yukawa couplings. Decays to quarkonia likely invalidate our simple calculations in the shaded regions.

Figure 1.3: Branching ratios of a singlet-like pseudoscalar in Type II 2HDM+S for $\tan\beta = 0.5$ (left) and $\tan\beta = 5$ (right) from [6], showing the dependence of the branching ratios on $\tan\beta$, as well as the prominence of the branching ratios to bb and $\tau\tau$, the channels searched for in the analysis presented here.

1.5 Two Real Singlet Model

The two real singlet model (TRSM) adds two real singlet degrees of freedom to the Standard Model. These are written as two real singlet fields S and X . Depending on the vacuum expectation values acquired by the scalars, different phases of the model can be realized [7]. To reduce the number of free parameters, two discrete \mathbb{Z}_2 symmetries are introduced. The fields are decomposed as

$$\Phi = \begin{pmatrix} 0 \\ \frac{\phi_h + v}{\sqrt{2}} \end{pmatrix}, S = \frac{\phi_S + v_S}{\sqrt{2}}, X = \frac{\phi_X + v_X}{\sqrt{2}} \quad (1.19)$$

To achieve electroweak-breaking symmetry, $v = v_{SM} \sim 246$ GeV is necessary. If the vacuum expectation values $v_S, v_X \neq 0$ the \mathbb{Z}_2 are spontaneously broken, and the fields $\phi_{h,S,X}$ mix into three physical scalar states. This is called the broken phase and leads to the most interesting collider phenomenology.

557 The mass eigenstates $h_{1,2,3}$ are related to the fields $\phi_{h,S,X}$ through a 3×3 orthogonal
558 mixing matrix denoted R . The mass eigenstates are assumed to be ordered $M_1 \leq$
559 $M_2 \leq M_3$. R is parameterized by the three mixing angles θ_{hS} , θ_{hX} , θ_{SX} . The nine
560 parameters of the scalar potential can be expressed in terms of the three physical
561 Higgs masses, the three mixing angles, and the three vacuum expectation values.

562 After fixing one of the Higgs masses to the mass of the observed Higgs boson, and
563 fixing the Higgs doublet vacuum expectation value to its Standard Model value, there
564 are seven remaining free parameters of the TRSM [7].

565 In one benchmark scenario of TRSM [7], the heaviest scalar state h_3 is identified
566 with the 125 GeV Higgs, h_{125} , and it can decay asymmetrically $h_{125} \rightarrow h_1 h_2$, which
567 we also denote $h \rightarrow a_1 a_2$ to highlight the similarity with the symmetric decay $h \rightarrow aa$
568 typically interpreted in 2HDM+S as discussed. The parameter values in TRSM are
569 chosen such that the coupling of h_3 to Standard Model particles are nearly identical
570 to the Standard Model predictions.

571 In benchmark scenario 1 (benchmark plane 1, or BP1) (Fig. 1.4) [7], the maximal
572 branching ratios for $h_3 \rightarrow h_1 h_2$ reach up to 7 – 8% which translates into a signal
573 rate of around 3 pb. These maximal branching ratios are reached in the intermediate
574 mass state for h_2 , $M_2 \sim 60 – 80$ GeV. For $M_2 < 40$ GeV, although phase space opens
575 up significantly for light decay products, the branching ratio becomes smaller.

576 If the decay channel $h_2 \rightarrow h_1 h_1$ is kinematically open (i.e. $M_2 > 2M_1$), it is the
577 dominant decay mode leading to a significant rate for the $h_1 h_1 h_1$ final state, in a
578 “cascade” decay. In BP1, $BR(h_2 \rightarrow h_1 h_1) \simeq 100\%$ above the red line in Fig. 1.4. If,
579 in addition, $M_1 \gtrsim 10$ GeV, the h_1 decays dominantly to $b\bar{b}$ leading to a sizable rate
580 for the $b\bar{b}b\bar{b}b\bar{b}$ final state as shown in Fig. 1.4 (*bottom right*).

581 If the $h_2 \rightarrow h_1 h_1$ decay is kinematically closed (i.e. $M_2 < 2M_1$), both scalars decay
582 directly to Standard Model particles, with branching ratios identical to a Standard
583 Model-like Higgs boson, i.e. with the $b\bar{b}b\bar{b}$ final state dominating, as shown in Fig. 1.4

584 (*bottom left*), while at smaller masses, combinations with τ leptons and eventually
585 final states with charm quarks and muons become relevant [7].

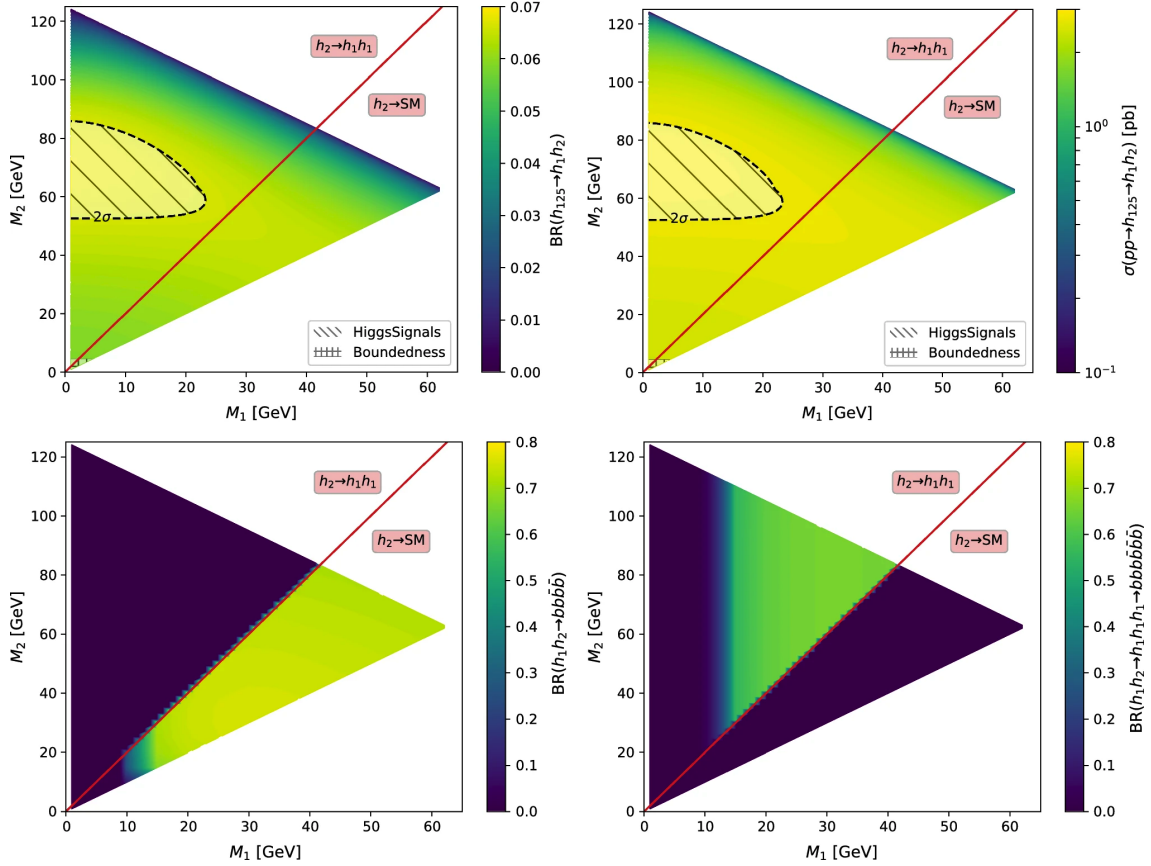


Figure 1.4: Benchmark plane BP1 for benchmark scenario 1 from [7], for the decay signature $h_{125} \rightarrow h_1 h_2$ with $h_{125} \equiv h_3$, defined in the (M_1, M_2) plane. The color code shows $\text{BR}(h_3 \rightarrow h_1 h_2)$ (*top left*) and the 13 TeV LHC signal rate for $pp \rightarrow h_3 \rightarrow h_1 h_2$ (*top right*). The red line separates the region $M_2 > 2M_1$, where $\text{BR}(h_2 \rightarrow h_1 h_1) \sim 100\%$, from the region $M_2 < 2M_1$, where $\text{BR}(h_2 \rightarrow F_{SM}) \sim 100\%$. The *bottom left* and *right* show the branching ratio of the $h_1 h_2$ into (respectively) $b\bar{b}b\bar{b}$, and through a $h_2 \rightarrow h_1 h_1$ cascade to $b\bar{b}b\bar{b}b\bar{b}$. The hatched region indicates where the decay rate slightly exceeds the 2σ upper limit inferred from the LHC Higgs rate measurements, though the region depends on the parameter choices and experimental searches should cover the whole mass range.

⁵⁸⁶ **Chapter 2**

⁵⁸⁷ **The Large Hadron Collider and the**
⁵⁸⁸ **CMS Experiment**

⁵⁸⁹ This chapter introduces the key aspects of the CERN Large Hadron Collider (LHC)
⁵⁹⁰ and the Compact Muon Solenoid (CMS) experiment where the work for this thesis was
⁵⁹¹ conducted. Section 2.1 describes the history of accelerator developments at CERN
⁵⁹² that led to the construction of the LHC, the current LHC configuration, and the
⁵⁹³ largest experiments located at the LHC. The concepts of beam luminosity and pile-
⁵⁹⁴ up, which are critical for understanding and measuring high-energy particle collisions,
⁵⁹⁵ are described in Section 2.2 and discussed in the context of the High-Luminosity
⁵⁹⁶ LHC (HL-LHC) upgrade in Section 2.3. Lastly, Section 2.4 describes the design
⁵⁹⁷ and function of CMS and its subdetectors, and terminates in a description of data
⁵⁹⁸ processing at CMS, beginning from online event filtering in the Level-1 Trigger, to
⁵⁹⁹ processing in the High-Level Trigger, to offline particle reconstruction, and finally
⁶⁰⁰ long-term storage and processing of measured events.

601 2.1 The Large Hadron Collider

602 CERN, the European Organization for Nuclear Research, is an international organiza-
603 tion based in Meyrin, Switzerland which operates the world's largest particle physics
604 laboratory, and is the site of the Large Hadron Collider (LHC) [8]. The very first
605 accelerator built at CERN was the 600 MeV Synchrocyclotron (SC), which initially
606 provided beams for CERN's first experiments. The newer and more powerful Proton
607 Synchrotron (PS), which could accelerate particles to an energy of 28 GeV, began op-
608 erations in 1959 and is still in use today. The first hadron collider at CERN was the
609 Intersecting Storage Rings (ISR), which consisted of two interlaced rings each with a
610 diameter of 200. The ISR collided protons at a center-of-mass energy of 62 GeV and
611 began measuring collisions in 1971. In 1968 CERN began to accelerate heavy ions
612 in the Super Proton Synchrotron (SPS), which is 7 kilometers in circumference and
613 was the first of CERN's giant underground rings to be built. The SPS became the
614 forefront of CERN's particle physics program in 1976, and in 1981 was converted into
615 a proton-antiproton collider. The final and largest underground ring constructed at
616 CERN was the Large Electron-Positron (LEP) collider, which was commissioned in
617 July 1989 and hosted 5176 magnets and 128 accelerating cavities located around a
618 27-kilometer circumference. Over 11 years of research, four detectors, ALEPH, DEL-
619 PHI, L3, and OPAL measured the collisions, with collision energies reaching up to
620 209 GeV in the year 2000. In November 2000, LEP was closed down to make way for
621 the construction of the LHC in the same tunnel.

622 In its current configuration, the LHC accelerator complex at CERN is a suc-
623 cession of machines that accelerate particles in stages until they reach their final energy
624 of 6.5 TeV per beam [9] [10]. In Linear accelerator 4 (Linac4), negative hydrogen
625 ions (hydrogen atoms with an additional electron) are accelerated to 160 MeV, and
626 stripped of their two electrons, leaving only protons, before entering the Proton Syn-
627 chrotron Booster (PSB). These protons are accelerated to 2 GeV, then to 26 GeV in

628 the Proton Synchrotron (PS), and 450 GeV in the Super Proton Synchrotron (SPS).
629 The protons are transferred to the two beam pipes of the Large Hadron Collider
630 (LHC). The LHC is a 27-kilometer ring of superconducting magnets, inside which
631 one beam circulates clockwise and the other counterclockwise. Each LHC ring takes
632 4 minutes and 20 seconds to fill, and it takes about 20 minutes for the protons to
633 reach their maximum energy. During normal operating conditions, beams circulate
634 for many hours inside the LHC ring.

635 The beams of particles in the LHC are made to collide at a center-of-mass energy
636 of up to 14 TeV, at four positions at particle detector experiments located around
637 the ring: ATLAS, CMS, ALICE, and LHCb. An aerial view of the four major
638 experiments' locations is shown in Fig. 2.1 [11]. ATLAS and CMS are the two
639 general-purpose detectors with broad physics programmes spanning Standard Model
640 measurements and searches for signatures of new physics [12] [13]. The two experi-
641 ments use different technical solutions and different magnet system designs. ALICE
642 is a general-purpose detector dedicated to measuring LHC heavy-ion collisions, and
643 is designed to address the physics of strongly interacting matter, and the properties
644 of quark-gluon plasma [14]. The LHCb experiment specializes in investigating CP vi-
645 olation through measuring the differences in matter and antimatter, by using a series
646 of subdetectors to detect mainly forward particles close to the beam direction [15].

647 2.2 Luminosity and pile-up

648 In order to search for rare processes, such as those resulting from a Higgs, W, or Z
649 boson, a large number of parton interactions per second are required at the LHC.
650 The number of events generated per second by the LHC collisions is given by

$$N_{event} = \mathcal{L} \cdot \sigma_{event} \quad (2.1)$$

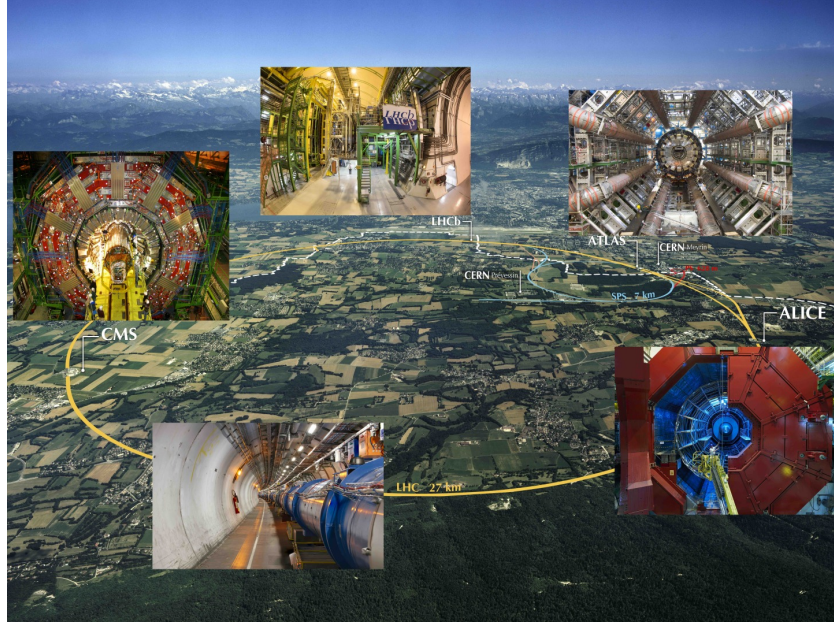


Figure 2.1: Aerial view of the Large Hadron Collider (LHC) spanning the border of France and Switzerland, and the four major experiments located around the ring: CMS (Compact Muon Solenoid), LHCb (LHC beauty), ATLAS (A Toroidal LHC Apparatus), and ALICE (A Large Ion Collider Experiment) [11].

where σ_{event} is the cross-section for the event under study, and \mathcal{L} the instantaneous luminosity. The instantaneous luminosity is measured in units of $\text{cm}^{-2} \text{ s}^{-1}$, and depends only on the beam parameters, and can be written for a Gaussian beam distribution as:

$$\mathcal{L} = \frac{N_b^2 n_b f_{rev} \gamma_r}{4\pi \epsilon_n \beta^*} F \quad (2.2)$$

where the parameters are as defined, along with some example typical nominal values in Phase-1 of the LHC [16] [17]:

- N_b is the number of particles per bunch ($N_b \approx 1.15 \times 10^{11}$ protons per bunch)
- n_b is the number of bunches per beam (maximum 2808),
- f_{rev} is the revolution frequency ($\approx 11 \text{ kHz}$),
- γ_r is the relativistic gamma factor,

- ϵ_n is the normalized transverse beam emittance (area in a transverse plane occupied by the beam particles),
 - β^* is the beta function at the collision point ($\beta^* = 0.55$ m),
 - and F is the geometric luminosity reduction factor due to the crossing angle at the interaction points ($F \approx 0.84$ for Phase-1. Note that complete overlap would give $F = 1$).

667 Peak luminosity at interaction points 1 and 5 reach values of $\sim 1.0 \times 10^{34} \text{ cm}^{-2} \text{ s}^{-1}$,
 668 with peak luminosity per bunch crossing reaching $\sim 3.56 \times 10^{34} \text{ cm}^{-2} \text{ s}^{-1}$.

Per Eqn. 2.1, the integrated luminosity over time is proportional to the number of events produced, and the size of LHC datasets is commonly presented in terms of integrated luminosity. Collider operation aims to optimize the integrated luminosity. Thus the exploration of rare events in the LHC collisions requires both high beam energies and high beam intensities.

The interaction vertex corresponding to the hard scattering of the protons is called the primary interaction vertex, or primary vertex (PV). The LHC's nominal beam luminosities are sufficiently large for multiple proton-proton collisions to occur in the same time window of 25 nanoseconds in which proton bunches collide [18]. To measure a proton-proton collision, the primary vertices must be separated from overlapping collisions, called “pile-up” collisions.

The pile-up is defined as the average number of pp collisions per bunch crossing, and can be estimated from the inelastic pp cross section of $\sigma_{\text{inel}} = 68.6$ millibarns at a center-of-mass energy of $\sqrt{s} = 13$ TeV [19]:

$$\text{Pile-up} = \frac{\mathcal{L} \times \sigma_{\text{inel}}}{n_b \cdot f} \sim 22 \quad (2.3)$$

⁶⁸³ A distribution of pile-up in the data-taking years 2016-2018 is shown in Fig. 2.2.

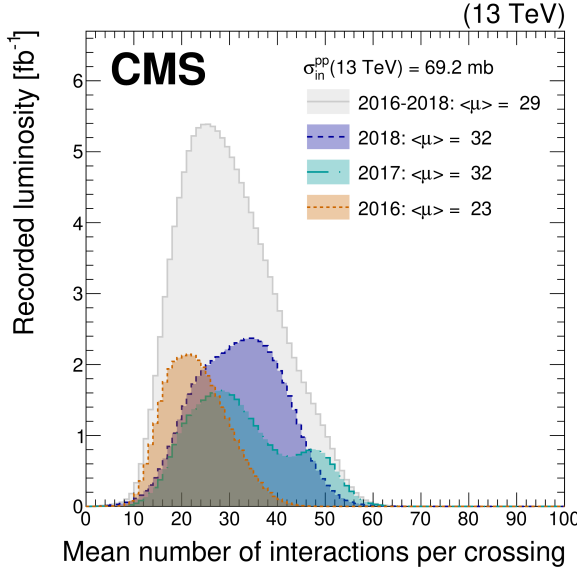


Figure 2.2: Distribution of the mean number of inelastic collisions per bunch crossing (pile-up) in data [18], for proton-proton collisions in 2016 (*dotted orange*), 2017 (*dotted light blue*), 2018 (*dotted dark blue*), and integrated over 2016-2018 (*solid grey*). A cross-section of inelastic proton-proton collisions of 69.2 mbarns is assumed. In the running conditions of the High-Luminosity LHC, pile-up will reach unprecedented levels of up to 200 per bunch crossing [20].

These multiple collisions will lead to higher occupancies in the detector, and particles originating from the pile-up interactions can be confused with those originating from the primary vertex. Thus, higher luminosities create more intense pile-up conditions, posing a greater challenge to detector performance and particle reconstruction and identification.

2.3 The High-Luminosity LHC

The High-Luminosity LHC (HL-LHC) is a major upgrade of the LHC scheduled to take place in the late 2020s, that will increase the instantaneous luminosity by a factor of five beyond the original design value, and the integrated luminosity by a factor of ten [20]. This will be accomplished through accelerator technological advances: for instance, reduction of the interaction point β^* from 0.55 m down to 0.15

695 m by installation of new final-focusing magnets, and improvements in the geometric
696 luminosity loss factor $F \approx 1$ through the installation of crab cavities that optimize
697 the orientation of colliding bunches. A further discussion of the HL-LHC upgrades
698 for the CMS detector follows in Chapter 3.

699 2.4 The CMS Detector

700 We give a brief overview of the Compact Muon Solenoid (CMS) experiment here
701 and discuss each of the subdetectors in more detail in the following sections. The
702 CMS experiment was conceived to study proton-proton and lead-lead collisions at
703 a center-of-mass energy of 14 TeV (5.5 TeV nucleon-nucleon) and at luminosities up
704 to $10^{34} \text{ cm}^{-2} \text{ s}^{-1}$ ($10^{27} \text{ cm}^{-2} \text{ s}^{-1}$) [21] [22]. Starting from the beam interaction region
705 at the center of the CMS detector, particles first pass through a silicon pixel and
706 strip tracker, in which charged-particle trajectories (tracks) and origins (vertices)
707 are reconstructed from signals (hits) in the sensitive layers. The tracker, electro-
708 magnetic calorimeter (ECAL), and hadronic calorimeter (HCAL) are immersed in a
709 high-magnetic-field superconducting solenoid that bends the trajectories of charged
710 particles. After passing through the tracker, electrons and photons are then absorbed
711 in the electromagnetic calorimeter (ECAL) comprised of lead-tungstate scintillating-
712 crystals. The corresponding electromagnetic showers are detected as clusters of energy
713 recording in neighboring cells, from which the direction and energy of the particles can
714 be determined. Charged and neutral hadrons may initiate a hadronic shower in the
715 ECAL as well, which is then fully absorbed in the hadron calorimeter (HCAL). The
716 resulting clusters are used to estimate their direction and energies. Muons and neu-
717 trinos pass through the calorimeters with little to no interactions. Neutrinos escaped
718 undetected; muons produce hits in additional gas-ionization chamber muon detectors
719 housed in the iron yoke of the flux-return. A sketch of example particle interactions

in a transverse slice of the CMS detector is shown in Fig. 2.3. The collision data is recorded with the use of the Level-1 (L1) trigger (discussed in greater detail in 2.5.5), the High-Level Trigger (HLT), and data acquisition systems ensuring high efficiency in selecting physics events of interest.

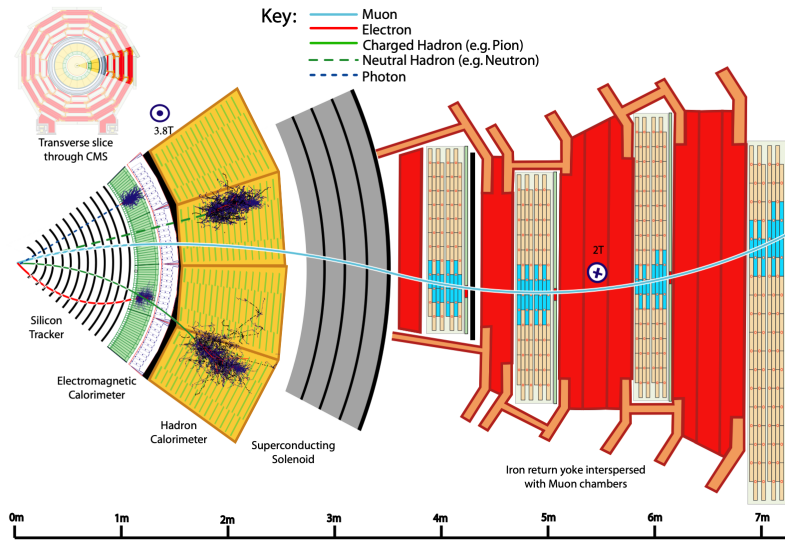


Figure 2.3: Sketch of particle trajectories of muons, electrons, charged and neutral hadrons, and photons in a transverse cross-section of the CMS detector [22].

CMS uses a right-handed coordinate system [21]. The origin is centered at the nominal collision point inside the experiment. The x axis points towards the center of the LHC, and the y axis points vertically upwards. The z axis points along the beam direction. The azimuthal angle, ϕ , is measured from the x axis in the x - y plane, and the radial coordinate in this plane is denoted by r . The polar angle, θ , is measured from the z axis. The pseudorapidity, η , is defined as $\eta = -\ln \tan(\theta/2)$. The momentum and energy transverse to the beam direction, denoted by p_T and E_T respectively, are computed from the x and y components. The momentum imbalance in the transverse plane is called the missing transverse momentum, and its magnitude is denoted by E_T^{miss} .

734 2.5 Sub-detectors of CMS

735 This section details the sub-detectors of CMS that operate to identify and precisely
736 measure muons, electrons, photons, and jets over a large energy range.

737 2.5.1 Inner tracking system

738 The CMS Tracker performs robust tracking and detailed vertex reconstruction in the
739 4 T magnetic field of the superconducting solenoidal magnet. The primary sensors
740 used in the tracker are p^+ on n -bulk devices, which allow high voltage operation and
741 are radiation-resistant [23] [24]. The active envelope of the CMS Tracker extends to a
742 radius of 115 cm, over a length of approximately 270 cm on each side of the interaction
743 point [23]. Charged particles in the region $|\eta| \lesssim 1.6$ benefit from the full momentum
744 measurement precision. In this region, a charged particle with p_T of 1000 GeV has a
745 sagitta of ~ 195 μm . The Tracker acceptance extends further to $|\eta| = 2.5$, with a
746 reduced radius of approximately 50 cm.

747 The high magnetic field of CMS causes low p_T charged particles to travel in helical
748 trajectories with small radii. The majority of events contain particles with a steeply
749 falling p_T spectrum, resulting in a track density which rapidly decreases at higher
750 radii.

751 A schematic view of the current Phase-1 CMS tracker [25], including the pixel
752 detector, is shown in Fig. 2.4. The Phase-1 pixel detector consists of three barrel
753 layers (BPIX) at radii of 4.4 cm, 7.3 cm, and 10.2 cm, and two forward/backward disks
754 (FPIX) at longitudinal positions of ± 34.5 cm and ± 46.5 cm, and extending in radius
755 from about 6 cm to 15 cm. These pixelated detectors produce 3D measurements along
756 the paths of charged particles with single hit resolutions between 10-20 μm .

757 After the pixel and on their way out of the tracker, particles pass through the
758 silicon strip tracker which reaches out to a radius of 130 cm (Fig. 2.4). The sensor el-

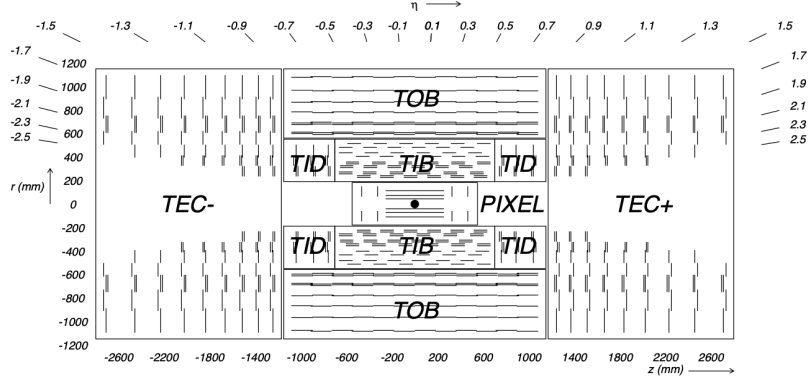


Figure 2.4: Cross section of the current Phase-1 CMS tracker [25]. Each line represents a detector module. Double lines indicate back-to-back modules which deliver two-dimensional (stereo) hits in the strip tracker.

ements in the strip tracker are single-sided p -on- n type silicon micro-strip sensors [21]. The silicon strip detector consists of four inner barrel (TIB) layers assembled in shells, with two inner endcaps (TID), each composed of three small discs. The outer barrel (TOB) consists of six concentric layers. Two endcaps (TEC) close off the tracker on either end.

2.5.2 ECAL

The electromagnetic calorimeter (ECAL) of CMS measures electromagnetic energy deposits with high granularity. One of the driving criteria in the design was the capability of detecting the Standard Model Higgs boson decay to two photons (in fact, the channel in which the 125 GeV Higgs boson was discovered at CMS). ECAL is a hermetic homogeneous calorimeter comprised of 61,200 lead tungstate (PbWO_4) crystals mounted in the central barrel, with 7,324 crystals in each of the two endcaps [21]. A preshower detector is located in front of the endcap crystals. Avalanche photodiodes (APDs) are used as photodetectors in the barrel and vacuum phototriodes (VPTs) in the endcaps.

The design of the ECAL is driven by the behaviour of high-energy electrons, which

775 predominantly lose energy in matter via bremsstrahlung, and high-energy photons
776 by e^+e^- pair production. The characteristic amount of matter traversed for these
777 interactions is the radiation length X^0 , usually measured in units of g cm $^{-2}$. The
778 radiation length is also the mean distance over which a high-energy electron loses all
779 but $1/e$ of its energy via bremsstrahlung [26]. Thus high granularity in η and ϕ , and
780 the length of the ECAL crystals, is designed to capture the shower of e/γ produced
781 by electrons and photons.

782 The barrel part of the ECAL (EB) covers the pseudorapidity range $|\eta| < 1.479$ [21].
783 The barrel granularity is 360-fold in ϕ and (2×85) -fold in η . The crystal cross-section
784 corresponds to approximately 0.0174×0.0174 in $\eta - \phi$ or 22×22 mm 2 at the front
785 face of the crystal, and 26×26 mm 2 at the rear face. The crystal length is 230 mm,
786 corresponding to $25.8 X_0$.

787 The ECAL read-out acquires the signals of the photodetectors [21]. At each bunch
788 crossing, digital sums representing the energy deposit in a trigger tower, comprising
789 5×5 crystals in $\eta \times \phi$, are generated and sent to the Level-1 trigger system (detailed
790 in Section 2.5.5).

791 2.5.3 HCAL

792 The hadronic calorimeter (HCAL) of CMS measures hadronic energy, which is key to
793 characterizing the presence of apparent missing transverse energy which could arise
794 from hadron jets and neutrinos or exotic particles [21]. A schematic of the components
795 of HCAL are shown in Fig. 2.5. The HCAL barrel (HB) and endcaps (HE) are located
796 outside of the tracker and the ECAL, spanning a radius of 1.77 m (outer extent of
797 ECAL) up to 2.95 m (inner extent of the magnet coil). An outer hadron calorimeter
798 (HO) is placed outside the solenoid to complement the barrel calorimeter. Beyond
799 $|\eta| = 3$, the forward hadron calorimeter (HF) at 11.2 m from the interaction point
800 extend the pseudorapidity coverage to $|\eta| = 5.2$.

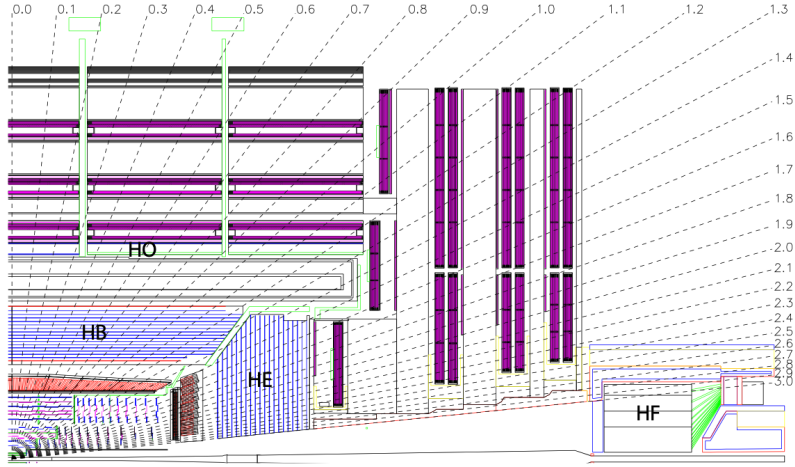


Figure 2.5: Longitudinal view of the CMS detector showing the hadron calorimeter barrel (HB), endcap (HE), outer (HO), and forward (HF) calorimeters from [21].

801 The HB is a sampling calorimeter covering the pseudorapidity range $|\eta| < 1.3$ [21].
 802 It consists of 36 identical azimuthal wedges which form two half-barrels (HB+ and HB-
 803), with a segmentation of $(\Delta\eta, \Delta\phi) = (0.087, 0.087)$. The HE covers pseudorapidity
 804 $1.3 < |\eta| < 3$. The HB and endcap HE calorimeters are sampling calorimeters which
 805 use brass as the absorber and plastic scintillator as the active material. Light from
 806 the plastic scintillator is wavelength-shifted and captured in optic fibers which are
 807 read out by front-end electronics [27].

808 In the central pseudorapidity region, the combined stopping power of EB plus the
 809 HB is insufficient to contain hadron showers [21]. To ensure adequate sampling depth,
 810 the hadron calorimeter is extended with a tail catcher, the HO. The size and position
 811 of the tiles are designed to roughly map the layers of the HB to make towers with
 812 the same granularity of 0.087×0.087 in η and ϕ . HO uses the same active material
 813 as the HB and HE calorimeters, but uses the steel return yoke and magnet material
 814 of CMS as absorbers [27].

815 The HF is a Cherenkov calorimeter based on a steel absorber and quartz fibers
 816 which run longitudinally through the absorber and collect Cherenkov light, primarily
 817 from the electromagnetic component of showers developed in the calorimeter [27].

818 Photomultiplier tubes are used to collect light from the quartz fibers. The HF is
819 designed to survive in the harsh radiation conditions and high particle flux of the for-
820 ward region. On average, 760 GeV per proton-proton interaction is deposited into the
821 two forward calorimeters, compared to only 100 GeV for the rest of the detector [21].
822 Furthermore, this energy has a pronounced maximum at the highest rapidities.

823 **2.5.4 Muon detectors**

824 The CMS muon system is designed to have the capability of reconstructing the mo-
825 mentum and charge of muons over the kinematic range of the LHC, since muons are a
826 powerful handle on signatures of interesting processes over the high background rate
827 of the LHC [21]. For instance, the decay of the Standard Model Higgs boson into
828 ZZ , which in turn decay to 4 leptons, can be reconstructed with high 4-particle mass
829 resolution if all the leptons are muons, since muons are less affected than electrons
830 by radiative losses in the tracker material.

831 The muon system consists of a cylindrical barrel section and two planar endcap
832 regions [21]. The barrel muon detector consists of drift tube (DT) chambers covering
833 the pseudorapidity region $|\eta| < 1.2$ (Fig. 2.6). The DTs can be used as tracking
834 detectors due to the barrel region’s characteristic low neutron-induced backgrounds,
835 low muon rate, and relatively uniform 4T magnetic field contained in the steel yoke.

836 In the two endcap regions, the muon rates and background levels are high and the
837 magnetic field is large and non-uniform [21]. Here, the muon system uses cathode
838 strip chambers (CSCs) to identify muons between $0.9 < |\eta| < 2.4$. The cathode strips
839 of each chamber run radially outwards and provide a precision measurement in the
840 $r - \phi$ bending plane. The anode wires run approximately perpendicular to the strips
841 and are read out in order to measure η and the beam-crossing time of a muon.

842 In addition to the DT and CSC, a dedicated trigger system consisting of resistive
843 plate chambers (RPCs) in the barrel and endcap regions provide a fast, independent,

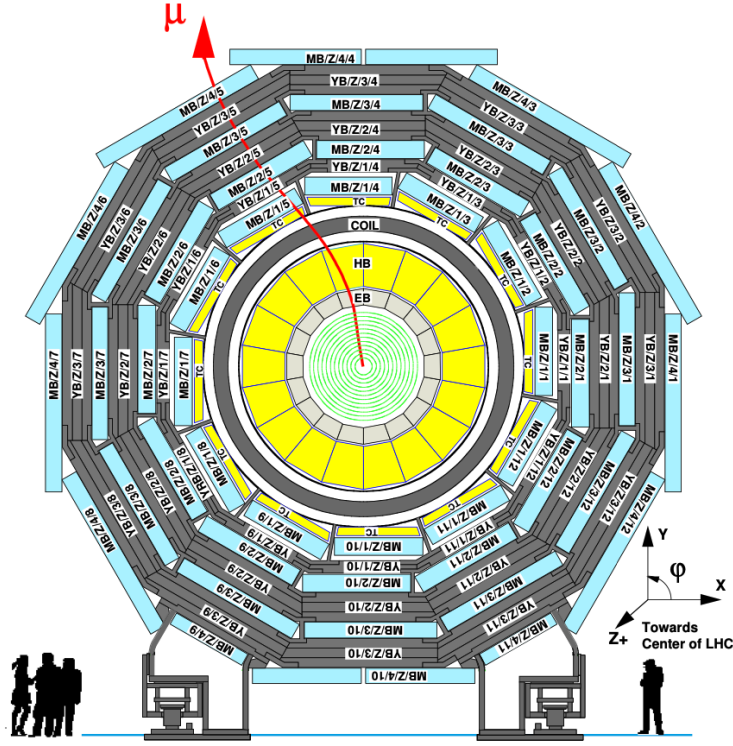


Figure 2.6: Layout of the CMS barrel muon drift tube (DT) chambers in one of the five wheels from [21]. The DTs are organized in 12 sectors of the yoke barrel (YB). In each of the 12 sectors of the yoke, there are 4 muon chambers per wheel (MB1, MB2, MB3, and MB4).

and highly-segmented trigger with a sharp p_T threshold over a large portion of the pseudorapidity range ($|\eta| < 1.6$) of the muon system [21]. RPCs have good time resolution but coarser position resolution compared to the DTs or CSCs. The RPCs also play a role in resolving ambiguities in reconstructing tracks from multiple hits in a chamber.

2.5.5 The Level-1 Trigger

The design performance of the LHC corresponds to an instantaneous luminosity of $10^{34} \text{ cm}^{-2} \text{ s}^{-1}$ with a 25 ns bunch crossing rate, giving an average pile-up (number of simultaneous events) of 25 per bunch crossing [28]. However, during Run 2, in 2017

and 2018 the LHC was able to surpass this goal with a mean number of 32 interactions per bunch crossing, and reaching over 50 interactions in short periods (Fig. 2.2). The large number of events from inelastic collisions (minimum bias events) per bunch crossing, combined with the small cross-sections of possible physics discovery signatures, necessitates a sophisticated event selection system for filtering this large event rate, as it is impossible to save all events. This data filtering system is implemented by CMS in two stages. The first stage is the Level-1 (L1) Trigger, which is deployed in custom electronic hardware systems and is responsible for reducing the event rate to around 100 kHz. The second stage is the High-Level Trigger (HLT) which is described in Section 2.5.6. This section describes the Phase-1 configuration of the Level-1 Trigger.

The L1 Trigger data flow of Phase-1 is shown in Fig. 2.7 [28], with organization into the L1 calorimeter trigger, the L1 muon trigger, and the L1 Global Trigger (GT).

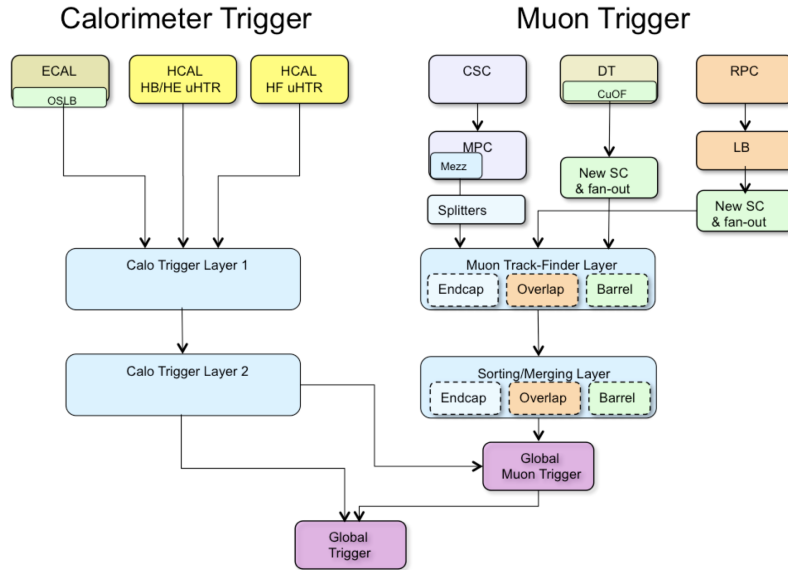


Figure 2.7: Dataflow for the Phase-1 Level-1 Trigger [28], which is implemented in custom hardware and is responsible for reducing the event rate from the LHC bunch crossing frequency of 400 MHz (bunch crossings every 25 ns) to a maximum rate of 100 kHz. In Phase-1, the Level-1 Trigger has access to information from the calorimeter and muon detectors.

866 The L1 calorimeter trigger begins with trigger tower energy sums formed by the
867 ECAL, HCAL, and HF Trigger Primitive Generator (TPG) circuits from the indi-
868 vidual calorimeter cell energies. In the original configuration, the ECAL energies
869 were accompanied by a bit indicating the transverse extent of the electromagnetic
870 energy deposits, and the HCAL energies were accompanied by a bit indicating the
871 presence of minimum ionizing energy [29]. During Long Shutdowns 1 and 2 (LS1
872 and LS2), HF was upgraded to provide finer granularity information to the trigger,
873 and the HCAL barrel and endcap front-end electronics were upgraded to provide
874 high-precision timing information and depth segmentation information.

875 In the original design of the L1 calorimeter trigger, the trigger primitives are pro-
876 cessed by the Regional Calorimeter Trigger (RCT, upgraded to Calo Layer 1 after
877 LS2) which finds isolated and non-isolated electron/photon candidates [28]. At this
878 stage, electrons/photons candidates are treated together since they cannot be defini-
879 tively distinguished at this stage due to lack of tracking information in the L1 trigger.
880 The Global Calorimeter Trigger (GCT, upgraded to Calo Layer 2 after LS2) sorts
881 further the candidate electrons/photons, finds jets (classified as central, forward, and
882 tau) using the E_T sums and performs calibration of the clustered jet energies, and
883 calculates global quantities such as missing E_T . It sends the top four candidates of
884 each type to the Global Trigger [28].

885 During LS2 and before Run-2, the legacy calorimeter trigger was upgraded to be
886 more flexible, maintainable, and performant [30] [31] [32]. These upgrades included
887 the replacement of legacy VME-based electronics with the microTCA modern tele-
888 coms standard, and system-wide usage of the latest generation of FPGAs, Xilinx
889 Virtex 7. Parallel copper links were replaced in almost all cases with serial optical
890 links, allowing link speeds to increase from 1 Gb/s to 10 Gb/s [30]. A schematic of
891 the current calorimeter trigger is shown in Fig. 2.8. The calorimeter Layer-1 is imple-
892 mented in 18 Calorimeter Trigger Processor (CTP7) boards, with each card spanning

893 4 out of 72 towers in ϕ and all of η . Tower-level operations are performed in Layer-1,
 894 such as the sum of ECAL and HCAL energies, energy calibration, and the compu-
 895 tation of the ratio of HCAL to ECAL energies. The Layer-1 cards each transmit 48
 896 output links at 10 Gb/s to the nine Layer-2 Master Processor cards (MP7) cards,
 897 which host calorimeter algorithms that find particle candidates and compute global
 898 energy sums. Each MP7 takes 72 input links and has access to the whole event at
 899 trigger tower granularity, such that the algorithms are fully pipelined and start pro-
 900 cessing as soon as the minimum amount of data is received. The trigger candidates
 901 are sent to a demultiplexer (demux) board, also a MP7, which formats the data for
 902 the upgraded Global Trigger, also called the microGT (μ GT).

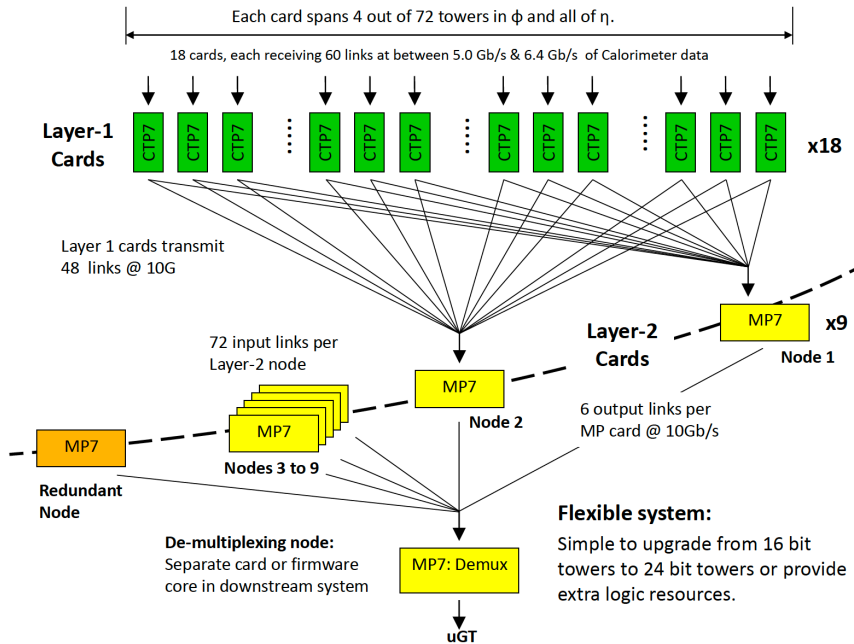


Figure 2.8: Schematic of the calorimeter trigger after Long Shutdown 2 [30]. The Layer-1 calorimeter trigger is implemented in CTP7 cards, which send time-
 multiplexed outputs to the Layer-2 MP7 cards. The Layer-2 cards handle the data in
 a round-robin style and the outputs are de-multiplexed, producing one output data
 stream to the Global Trigger.

903 Each of the L1 muon triggers has its own trigger logic [29]. The RPC strips are
 904 connected to a Pattern Comparator Trigger (PACT), which forms trigger segments

905 that are used to build tracks and calculate p_T . The RPC logic also provides some
906 hit data to the CSC trigger system to resolve ambiguities caused by two muons in
907 the same CSC. The CSCs form local charged tracks (LCTs) from the cathode strips,
908 which are combined with the anode wire information. LCTs are combined into full
909 muon tracks and assigned p_T values.

910 The Global Muon Trigger (GMT) sorts the RPC, DT, and CSC muon tracks,
911 converts these tracks to the same η , ϕ , and p_T scale, and validates the muon sign [29].
912 It improves the trigger efficiency by merging muon candidates that were detected
913 in two complementary sub-systems (i.e. DT+RPC, or CSC+RPC). The GMT also
914 contains logic to correlate the found muon tracks with an $\eta-\phi$ grid of quiet calorimeter
915 towers to determine if the muons are isolated, as well as logic to remove duplicate
916 candidates originating in the overlap regions from both DT and CSC systems. The
917 final collection of muons are sorted based on their initial quality, correlation, and p_T ,
918 and the top four muons are sent to the Global Trigger [29].

919 The Global Trigger (GT) receives information from the GCT and GMT, and
920 makes the Level-1 Accept (L1A) decision to either discard or accept the bunch cross-
921 ing [29]. This is accomplished by sorting ranked trigger objects that are accompanied
922 by positional information in η and ϕ , permitting the trigger to applying criteria with
923 thresholds that can vary based on the location of the trigger objects, and/or to re-
924 quire trigger objects to be close to or opposite from each other. The GT L1A decision
925 arrives at the detector front end with a $3.8 \mu\text{s}$ latency after the interaction at a rate
926 which is required to be less than 100 kHz, and triggers a full readout of the detector
927 for further processing.

928 2.5.6 The High-Level Trigger

929 The HLT is implemented in software running on a large computer farm of fast com-
930 mercial processors [33] [34]. The algorithms in HLT have access to full data from

931 all CMS sub-detectors, including the tracker, with full granularity and resolution.
932 The HLT reconstruction software is similar to what is used offline for full CMS data
933 analysis. As a result, the HLT can calculate quantities with a resolution compara-
934 ble to the final detector resolution, compared to the L1 Trigger. The HLT performs
935 more computationally-intensive algorithms, such as combining tau-jet candidates in
936 the calorimeter with high- p_T stubs in the tracker, to form a hadronic tau trigger. The
937 maximum HLT input rate from the L1 Trigger is 100 kHz, and the HLT output rate
938 is approximately 100 Hz.

939 The HLT contains trigger paths, each corresponding to a dedicated trigger [35].
940 A path consists of several steps implemented as software modules. Each HLT trigger
941 path must be seeded by one or more L1 trigger bits: the first module always looks
942 for a L1 seed, consisting of L1 bit(s) and L1 object(s). Each module performs a well-
943 defined task such as unpacking (raw to digitized quantities), reconstruction of physics
944 objects (electrons, muons, jet, missing transverse energy, etc.), making intermediate
945 decisions that trigger more detailed reconstruction modules, and calculating the final
946 decision for the trigger path. If an intermediate filter decision is negative, the rest of
947 the path is not executed, and the trigger rejects the event.

948 **2.5.7 Particle reconstruction**

949 To build a description of the physics objects present in the particle collision, the
950 basic elements from the detector layers (tracks and clusters of energy) are correlated
951 to identify each particle in the final state. Measurements from different sub-detectors
952 are combined to reconstruct the particle properties. This approach is called particle-
953 flow (PF) reconstruction [22]. Key to the success of the PF reconstruction is the
954 fine spatial granularity of the detector layers. Coarse-grained detectors can cause
955 the signals from different particles to merge, especially within jets. However, if the
956 subdetectors are sufficiently segmented to separate individual particles, it becomes

957 possible to produce a global event description that identifies all physics objects with
958 high efficiencies and resolution.

959 **2.5.8 Data storage and computational infrastructure**

960 The LHC generates over 15 petabytes (15 million gigabytes) of data every year, neces-
961 sitating a flexible computing system that can be accessed by researchers working at
962 the four main LHC experiments: ALICE, ATLAS, CMS, and LHCb. The Worldwide
963 LHC Computing Grid (WLCG) [36] is a global collaboration of computer centers that
964 links thousands of computers and storage systems in over 170 centers across 41 coun-
965 tries. These centers are arranged in “tiers”, and provide near real-time access to users
966 processing, analyzing, and storing LHC data. One of the final stages of data analy-
967 sis at LHC experiments is large-scale data processing taking place over distributing
968 computing, for instance, with the use of Condor [37], a distributed, scalable, flexible
969 batch processing system which accepts a computing job, allocates a resource to it,
970 executes it, and returns the result back to a user transparently.

₉₇₁ **Chapter 3**

₉₇₂ **The Phase-2 Upgrade of CMS**

₉₇₃ This chapter gives an overview of the High-Luminosity LHC upgrade of the LHC in
₉₇₄ Section 3.1, and the upgrades for the Phase-2 CMS Level-1 (L1) Trigger in Section
₉₇₅ 3.2. One of the major upgrades is the new availability of calorimeter crystal-level
₉₇₆ information to the L1 calorimeter trigger, compared to the current trigger which only
₉₇₇ has access to tower-level information (a tower being 5 by 5 in crystals). To capitalize
₉₇₈ on the increased spatial granularity of this information, an upgraded algorithm is
₉₇₉ presented which reconstructs and identifies electron and photon candidates in the the
₉₈₀ Layer-1 Calorimeter Trigger. A description of the algorithm and a validation of its
₉₈₁ performance in Phase-2 conditions is given in Section 3.3.

₉₈₂ **3.1 The High-Luminosity LHC**

₉₈₃ In order to sustain and extend the LHC’s physics discovery program and maintain
₉₈₄ operability for a decade or more, the LHC is undergoing a major upgrade to the High-
₉₈₅ Luminosity LHC (HL-LHC). In its final configuration, the HL-LHC will deliver a peak
₉₈₆ luminosity of $7.5 \times 10^{34} \text{ cm}^{-2} \text{ s}^{-1}$, potentially leading to total integrated luminosity
₉₈₇ of 4000 fb^{-1} after ten years of operations, scheduled to begin in 2027 [38]. This
₉₈₈ integrated luminosity is about ten times the predicted luminosity reach of the LHC

989 in its initial configuration. To enable the CMS experiment to continue operations and
990 data-taking and to maximize the discovery potential of the unprecedented amount
991 of data, the CMS detector is undergoing Phase-2 upgrades in order to perform high-
992 precision measurements and searches for physics beyond the Standard Model in the
993 intense running conditions of the HL-LHC.

994 3.2 The Phase-2 Level-1 Trigger

995 To achieve the goals of the HL-LHC program and to ensure the collection of information-
996 rich datasets in the HL-LHC, the Phase-2 upgrade of the CMS Level-1 Trigger [38]
997 must be upgraded in conjunction with the CMS sub-detectors and their readouts, to
998 maintain physics selectivity. The HL-LHC will produce an intense hadronic environ-
999 ment corresponding to 200 simultaneous collisions per beam crossing, necessitating
1000 comprehensive upgrades of the trigger system outlined below.

1001 In order to cope with the increased pile-up and high occupancies of the HL-LHC,
1002 the latency of the L1 trigger system (time available to produce a L1 Accept signal) will
1003 be increased significantly from $3.8 \mu\text{s}$ to $12.5 \mu\text{s}$, with an increased maximum output
1004 bandwidth of 750 kHz [38]. With the increased latency, in addition to information
1005 from calorimeters and muon detectors (as in the Phase-1 system), information from
1006 the new tracker and high-granularity endcap calorimeter can also be included at L1
1007 for the first time. This is illustrated in the functional diagram of the architecture of
1008 the Phase-2 trigger system in Fig. 3.1.

1009 The key feature of the Phase-2 L1 Trigger is the introduction of a correlator layer,
1010 where algorithms produce higher-level trigger objects by combining information from
1011 sub-detectors, with a selectivity approaching that of offline reconstruction in the
1012 HLT [38]. Four independent data processing paths (grouped together in Fig. 3.1) are
1013 implemented: tracking, calorimetry, muon systems, and particle-flow techniques:

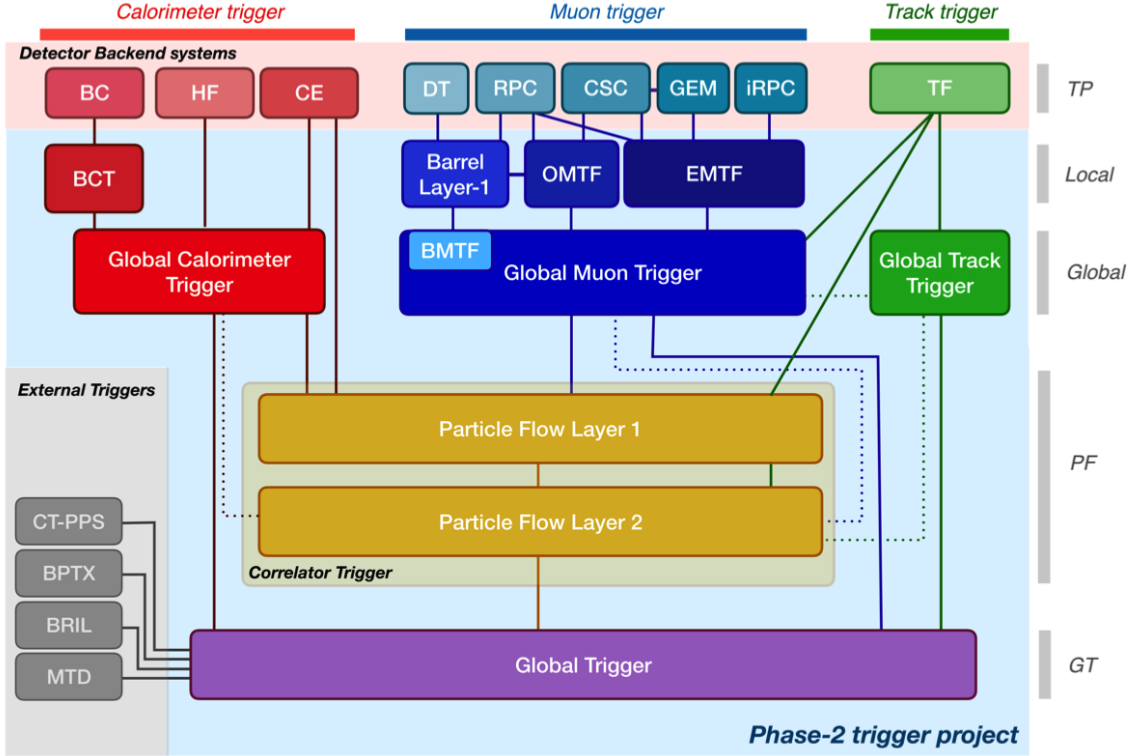


Figure 3.1: Functional diagram of the CMS L1 Phase-2 upgraded trigger design [38], showing the four trigger paths: calorimeter, muon, track, and Particle Flow. For the first time, tracking information will be available as early as the L1 Trigger.

- **Calorimeter Trigger path:** (red, Fig. 3.1) A barrel calorimeter trigger (BCT) and the HGCAL backend are used to process crystal-level information from the calorimeters to produce high-resolution clusters and identification variables used for later processing. Outputs from the BCT, HGCAL, and the HF are sent to a global calorimeter trigger (GCT), where calorimeter-only objects such as e/γ candidates, hadronically decaying tau lepton candidates, jets, and energy sums are built.
- **Track Trigger path:** (green, Fig. 3.1) Tracks from the Outer Tracker are reconstructed in the track finder (TF) processors as part of the detector backend. A global track trigger (GTT) will reconstruct the primary vertices of the event, along with tracker-only based objects, such as jets and missing transverse momentum.

- **Muon Trigger path:** (*blue*, Fig. 3.1) Trigger primitives are processed by muon track finder algorithms, again separated into the barrel (barrel muon track finder, BMTF), overlap (overlap muon track finder, OMTF), and endcap (endcap muon track finder, EMTF). Standalone muons and stubs containing information such as position, bend angle, and timing, as well as L1 tracks, are sent to the global muon trigger (GMT).
- **Particle-Flow Trigger path:** (*yellow*, Fig. 3.1) The correlator trigger (CT) aims to approach the performance of offline Particle Flow, and is implemented in two layers. “Layer-1” produces the particle-flow candidates from matching calorimeter clusters and tracks. “Layer 2” builds and sorts final trigger objects and applies additional identification and isolation criteria.

The outputs from the above trigger paths are combined in the Global Trigger (GT) (*purple*, Fig. 3.1), which calculates the final trigger decision (Level-1 Accept), transmitting it to the Trigger Control and Distribution System (TCDS), which distributes it to the detector backend systems, initiating the readout to the DAQ. The GT also provides the interface to external triggers (*grey*, Fig. 3.1), such as triggers for the precision proton spectrometer (PPS), beam position and timing monitors (BPTX), and luminosity and beam monitoring (BRIL) detectors [38]. The design of the Phase-2 Level-1 Trigger allows for future inclusion of triggering information, for instance information about minimum ionizing particles (MIPs) from the MIP Timing Detector (MTD) [39].

3.3 Standalone Barrel Calorimeter electron/photon reconstruction

The reconstruction and identification of electrons and photons (e/γ) begin with the trigger primitives of the barrel ECAL and HCAL detectors and endcap HGCAL calorimeters, covering the pseudorapidity region $|\eta| < 3$. The barrel and endcap regions of the detector are intrinsically different enough to warrant different approaches to e/γ reconstruction. This work focuses on the Standalone Calorimeter e/γ reconstruction taking place in the barrel (Fig. 3.2).

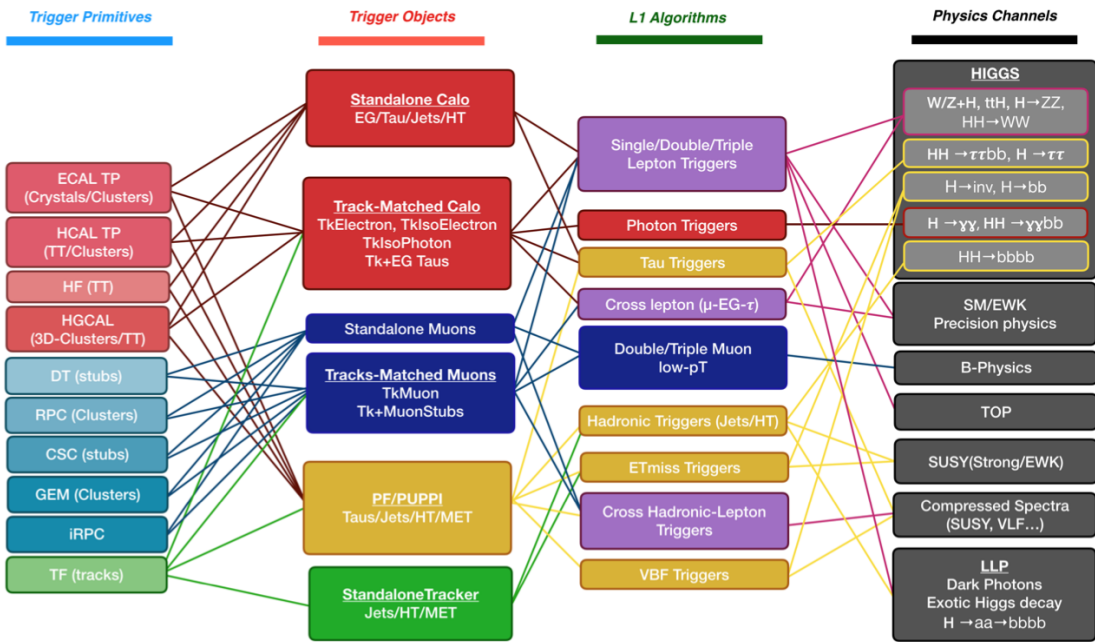


Figure 3.2: Summary of the links between the trigger primitives (*first column*), the trigger objects (*second column*), the Level-1 algorithms used in the menu (*3rd column*), and the physics channels (*4th column*), from [38], where a full description of the Phase-2 L1 algorithms can be found. This work focuses on developments for the Standalone Calorimeter electron and photon ("EG") reconstruction algorithm.

1055 **3.3.1 Phase-2 geometry of the ECAL Barrel trigger**

1056 In Phase-2, the upgrade of both on-detector and off-detector electronics for the barrel
1057 calorimeters trigger primitive generator (TPG) will stream single crystal data from
1058 the on-detector to the backend electronics, in contrast to the lower-granularity output
1059 of the Phase-1 ECAL TPG that is restricted to providing trigger tower sums of 5×5
1060 crystals [38]. A schematic representation of the geometry of the ECAL barrel in the
1061 Regional Calorimeter Trigger (RCT) is shown in Fig. 3.3. The barrel is spanned by
1062 36 RCT cards, each spanning 17×4 towers in $\eta \times \phi$. Each RCT card is subdivided
1063 into five “regions” as shown in Fig. 3.4. After initial clustering and processing, the
1064 outputs of the RCT card are sent to the Global Calorimeter (GCT) trigger, which is
1065 processed in three cards as shown in Fig. 3.5.

1066 **3.3.2 Phase-2 electron/photon reconstruction algorithm**

1067 The standalone barrel algorithm for reconstructing and identifying electrons and pho-
1068 tons in the Phase-2 Level-1 Trigger takes as input the digitized response of each crystal
1069 of the barrel ECAL, with a granularity 0.0175×0.0175 in $\eta \times \phi$, which is 25 times
1070 higher than the input to the Phase-1 trigger, which consisted of trigger towers with
1071 a granularity of 0.0875×0.0875 . In HCAL the tower size of 0.0875×0.0875 is un-
1072 changed. The trigger algorithm is designed to closely reproduce the algorithm used in
1073 the offline reconstruction, with limitations and simplifications due to trigger latency.

1074 In the RCT, an initial requirement of $p_T > 0.5$ GeV is imposed on the input
1075 trigger primitives (i.e. energies from the ECAL crystals and HCAL towers) to reject
1076 contribution from pile-up. In one of the regions inside a RCT card (Fig. 3.4), the
1077 crystal containing the highest energy deposit is identified as the seed crystal, as shown
1078 in Fig. 3.6. The energy in the crystals in a window of size 3×5 in $\eta \times \phi$ around
1079 the seed cluster is added into a cluster. The energy is considered “clustered”. The
1080 process is repeated with the remaining “unclustered” energy, until up to four clusters

1081 are produced in the region.

1082 To improve e/γ identification and to reduce background contributions, identifica-
1083 tion and reconstruction algorithms are implemented at this stage:

1084 • Shower shape: The energy deposit sums around the seed crystal is computed in
1085 windows of size 2×5 and 5×5 (Fig. 3.6, *dashed lines*), with true e/γ clusters
1086 tending to produce showers that deposit most of their energy in a 2×5 region.

1087 • Bremsstrahlung recovery: e/γ tend to spread in the ϕ direction due to charged
1088 particles being bent by the magnetic field of the CMS solenoid. If sufficient
1089 energy comparable to the core 3×5 cluster is found in the adjacent 3×5
1090 windows (Fig. 3.6, *shaded yellow*), the energy is added to the core cluster and
1091 no longer considered unclustered energy.

1092 After parallel processing in the regions, the clusters in a RCT card are stitched
1093 together if they are located directly along the borders of a region (Fig. 3.3). The
1094 remaining unclustered ECAL energy is summed into ECAL towers.

1095 From each RCT card, the twelve highest-energy clusters, as well as any remaining
1096 unclustered energy, are sent to the GCT. Since each GCT card has information from
1097 sixteen RCT cards (Fig. 3.5), final stitching across the boundaries of the RCT cards
1098 is performed. One more identification algorithm is performed at this stage:

1099 • Isolation: One handle to reject backgrounds from e.g. pile-up, comes from the
1100 tendency for background to be spread more uniformly across a large area in the
1101 detector, whereas genuine e/γ are expected to produce showers concentrated in
1102 the 3×5 crystal window. The energy sum in a large window of 7×7 in towers
1103 is computed and used to reject background.

1104 The performance of the standalone barrel e/γ algorithm in Phase-2 conditions is
1105 summarized in the efficiency and rates. The efficiencies are measured with a simulated
1106 Monte Carlo sample containing electrons. The rates are measured with a simulated

1107 minimum bias sample intended to closely mimic generic proton-proton collisions in
1108 the CMS detector. The performance of the Phase-2 emulator discussed in this work,
1109 which closely mimics the firmware logic and uses fixed-precision integers, is shown to
1110 be comparable to the previous emulator which used floats and idealized logic.

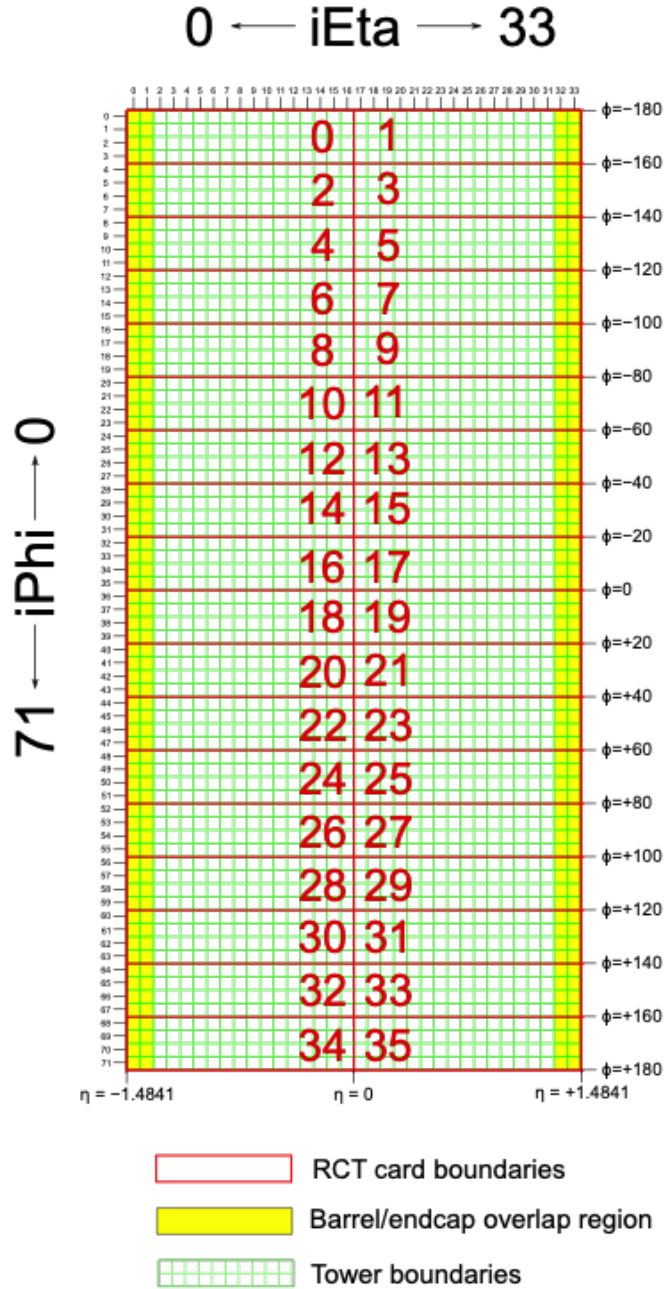


Figure 3.3: Schematic of the geometry of the Phase-2 ECAL barrel in the Regional Calorimeter Trigger (RCT), showing the division of the barrel region into 36 Regional Calorimeter Trigger (RCT) cards (*red*). Each card spans 17×4 towers in $\eta \times \phi$ (*green*), and each tower is 5×5 in single crystals in $\eta \times \phi$. Towers in the overlap region (*shaded yellow*) are read out to both the barrel and endcap.

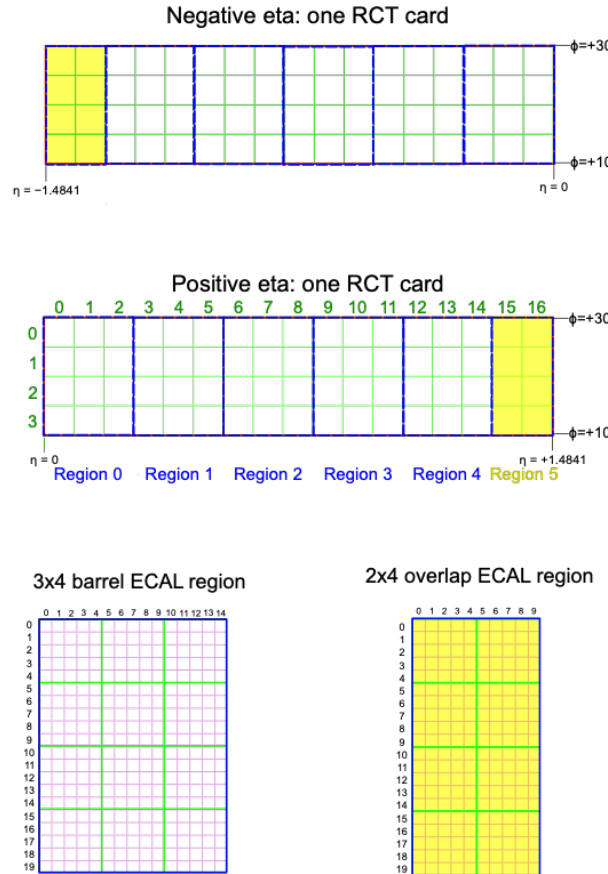


Figure 3.4: Schematic of two example RCT cards in the negative eta (*top*) and positive eta (*center*) regions of the ECAL barrel. Each RCT card is divided into five regions: four regions are of size 3×4 towers in $\eta \times \phi$ (*bottom left*), and a fifth smaller overlap region of size 2×4 towers (*bottom right*). Each tower is 5×5 ($\eta \times \phi$) in crystals.

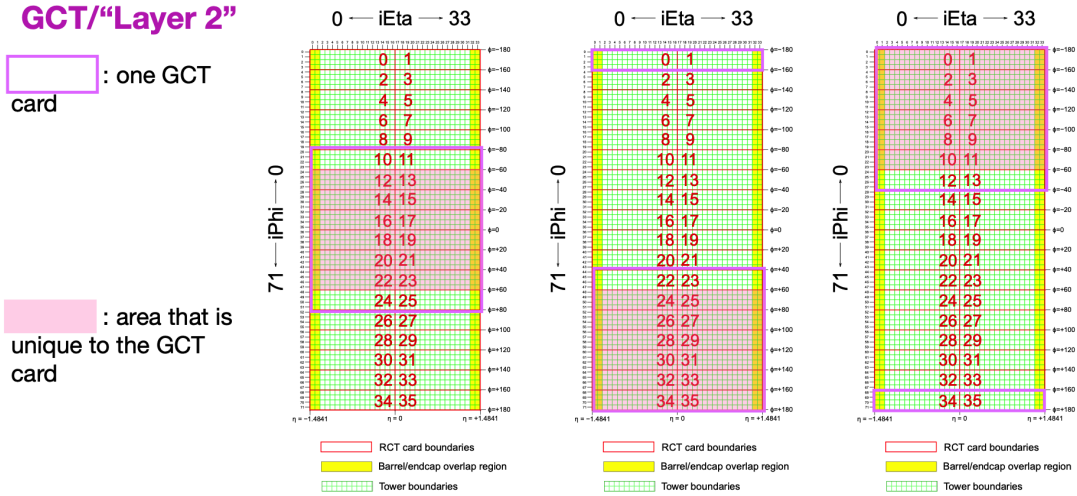


Figure 3.5: Schematic of the Phase-2 ECAL barrel in the Global Calorimeter Trigger (GCT), which will process the outputs of the Regional Calorimeter Trigger (RCT) in three cards (*magenta highlights*). Each card in the GCT processes the equivalent of sixteen RCT cards, with the center twelve being unique to that GCT card (*shaded pink*), and the remaining four processed in overlap with the other GCT cards.

3x4 barrel ECAL region

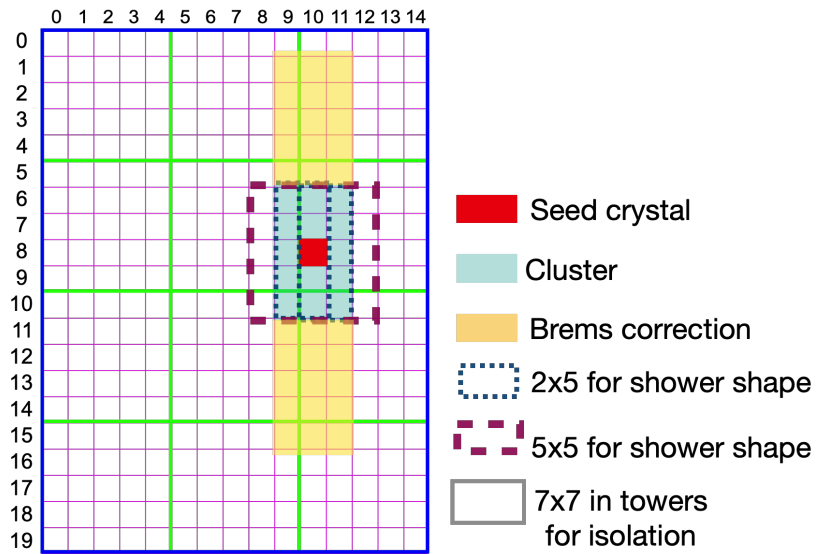


Figure 3.6: Illustration of an example electron/photon (e/γ) cluster in the Phase-2 Level-1 Trigger standalone barrel e/γ reconstruction, in a region of 15×20 crystals (3×4 towers). Each small pink square is one crystal, the highest-granularity ECAL trigger primitives available to the L1 Trigger in Phase-2. The core cluster consists of the energy sum in a 3×5 window of crystals, (*shaded light blue*) centered around the seed crystal (*red*). Bremsstrahlung corrections are checked in the adjacent 3×5 windows in the ϕ direction (*shaded light yellow*). The relative energies in windows of size 2×5 and 5×5 in crystals (*dashed dark blue and dark red*) are used to compute shower shape variables to identify true e/γ objects. Lastly, an isolation sum is computed in a window of size 7×7 in towers (not shown in figure).

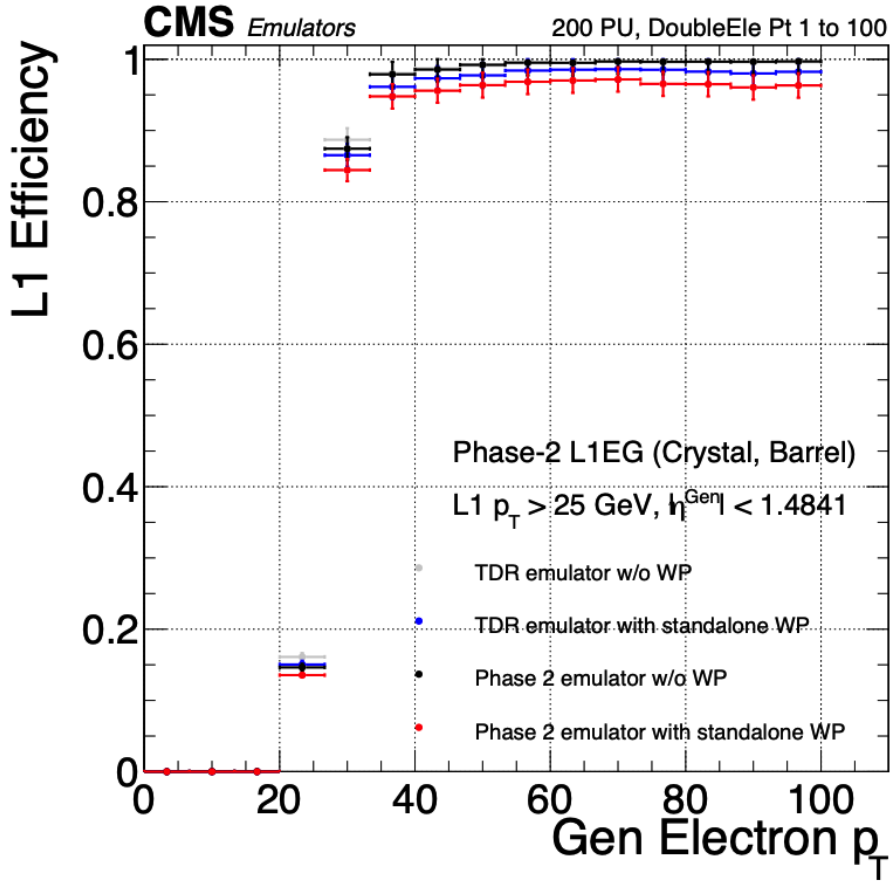


Figure 3.7: Efficiency of the standalone barrel e/γ reconstruction, measured in a simulated sample of electrons, as a function of the true electron's transverse momentum p_T . The performance of the previous, idealized algorithm as shown in the 2021 Phase-2 TDR [38] with and without the isolation and shower shape discrimination variables (“standalone working point/ WP”) (*dark blue, grey*). The Phase-2 emulator discussed in this work with and without the same working point (*black, red*) is shown to have comparable performance.

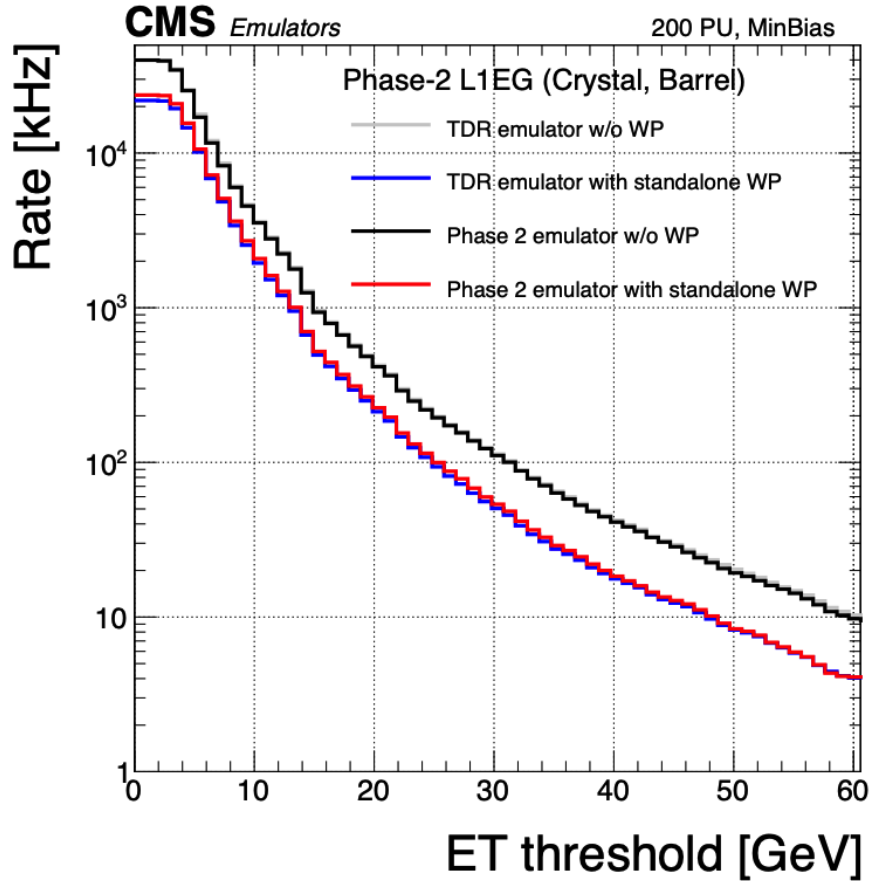


Figure 3.8: Rates of the standalone barrel e/γ reconstruction, evaluated on a minimum bias sample, measured as a function of the minimum energy (E_T) required of the reconstructed e/γ object in each event. The performance of the previous, idealized algorithm as shown in the 2021 Phase-2 TDR [38] with and without the isolation and shower shape discrimination variables (“standalone working point/ WP”) (*dark blue, grey*). The Phase-2 emulator discussed in this work with and without the same working point (*black, red*) is shown to have comparable performance.

₁₁₁₁ **Chapter 4**

₁₁₁₂ **Datasets and Monte Carlo samples**

₁₁₁₃ The search for the exotic decay of the 125 GeV Higgs boson to two light neutral scalars
₁₁₁₄ decaying to a pair of bottom quarks and a pair of tau leptons ($h \rightarrow aa \rightarrow bb\tau\tau$) is
₁₁₁₅ based on proton-proton collision data at a center-of-mass energy 13 TeV collected
₁₁₁₆ in Run-2 of data-taking, spanning the data-taking years 2016, 2017, and 2018. The
₁₁₁₇ datasets used and the triggers used to collect the data are described in Section 4.1.
₁₁₁₈ Section 4.2 describes the Monte Carlo simulated samples that are used to model the
₁₁₁₉ $h \rightarrow aa \rightarrow bb\tau\tau$ signal and background Standard Model processes. Lastly, in order
₁₁₂₀ to obtain a better description of Standard Model backgrounds that contain two tau
₁₁₂₁ leptons, a data-Monte Carlo hybrid technique is used to generate embedded samples
₁₁₂₂ which model processes with genuine $\tau\tau$ in the final state, as detailed in Section 4.3.

₁₁₂₃ **4.1 Datasets used**

₁₁₂₄ The $h \rightarrow aa \rightarrow bb\tau\tau$ analysis [40] is based on proton-proton collision data at a center-
₁₁₂₅ of-mass energy of 13 TeV collected in full Run-2 (2016-18) with the CMS detector.
₁₁₂₆ The data analyzed corresponds to a total integrated luminosity of 138 fb^{-1} (36.33 fb^{-1}
₁₁₂₇ for 2016, 41.53 fb^{-1} for 2017, and 59.74 fb^{-1} for 2018) [41] [42] [43]. The cumulative
₁₁₂₈ delivered and recorded luminosity versus time for 2015-2018 is shown in Fig. 4.1.

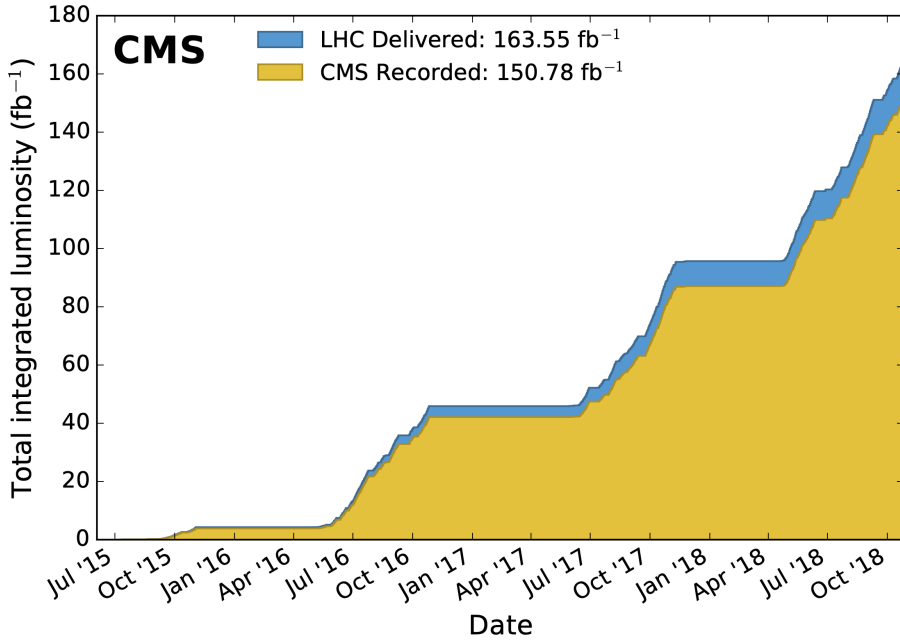


Figure 4.1: Cumulative delivered and recorded luminosity versus time for 2015-2018 at CMS, in proton-proton collision data only, at nominal center-of-mass energy [44].

1129 Data collected with the single muon trigger is used for the $\mu\tau_h$ channel. For the
 1130 $e\tau_h$ channel, data collected with the single electron trigger is used; and for the $e\mu$
 1131 channel, data collected with the electron + muon trigger is used. A more in-depth
 1132 discussion of the triggers used follows in a later section.

1133 A full list of samples used can be found in the full documentation [45] [40].

1134 4.2 Monte Carlo samples

1135 Modeling and computing observables originating from arbitrary physics processes at
 1136 the tree level and at next-to-leading order (NLO) is performed by Monte Carlo (MC)
 1137 event generators, such as Powheg and MadGraph5_amCNLO [46] [47]. The informa-
 1138 tion generated, e.g. the computation of the differential cross sections and kinematics
 1139 of the final state particles, is saved in a compressed file and used to generate MC sam-

1140 ples that are used in physics analyses. The samples are digitized using GEANT4 [48],
1141 a platform used at the LHC and other facilities to comprehensively simulate the pas-
1142 sage of particles through matter. The digitized samples are passed through the same
1143 detector reconstruction as real data events collected in the detector.

1144 The samples for modeling the signal ($h \rightarrow aa \rightarrow 2b2\tau$ and $h \rightarrow a_1a_2$) in the
1145 2HDM+S and TRSM are generated at tree-level, for a range of masses of the light
1146 neutral scalar a . For $h \rightarrow aa$, the mass hypotheses for the a range from $m_a =$
1147 (12 GeV, 62.5 GeV). For $h \rightarrow a_1a_2$, the mass hypotheses for the two light scalars span
1148 combinations of m_{a1} , m_{a2} ranging from (12 GeV, 62.5 GeV) for the two scalars.

1149 4.3 Embedded samples

1150 An important background for Higgs boson studies and searches for additional Higgs
1151 bosons is the decay of Z bosons into pairs of τ leptons ($Z \rightarrow \tau\tau$). An embedded tech-
1152 nique was developed in the context of Standard Model Higgs to $\tau\tau$ measurements, to
1153 model $Z \rightarrow \tau\tau$ decays, and was expanded to also model all Standard Model processes
1154 that contain $\tau\tau$ [49]. The embedded technique has since been used successfully at
1155 CMS for the Standard Model $H \rightarrow \tau\tau$ measurement, as well as searches for minimal
1156 supersymmetric extensions to the Standard Model (MSSM) [50] [51].

1157 Fig. 4.2 shows a schematic of how embedded samples are produced. Data events
1158 containing $Z \rightarrow \mu\mu$ decays are selected. In these events, all energy deposits of the
1159 recorded muons are removed, and are replaced with simulated tau leptons with the
1160 same kinematic properties as the removed muons. This results in a hybrid data format
1161 containing information from both observed and simulated events, as illustrated in Fig.
1162 4.2 [49].

1163 In the selection step of the embedded technique, events are selected with at least
1164 one of a set of $\mu\mu$ trigger paths, which require $p_T > 17(8)$ GeV for the leading

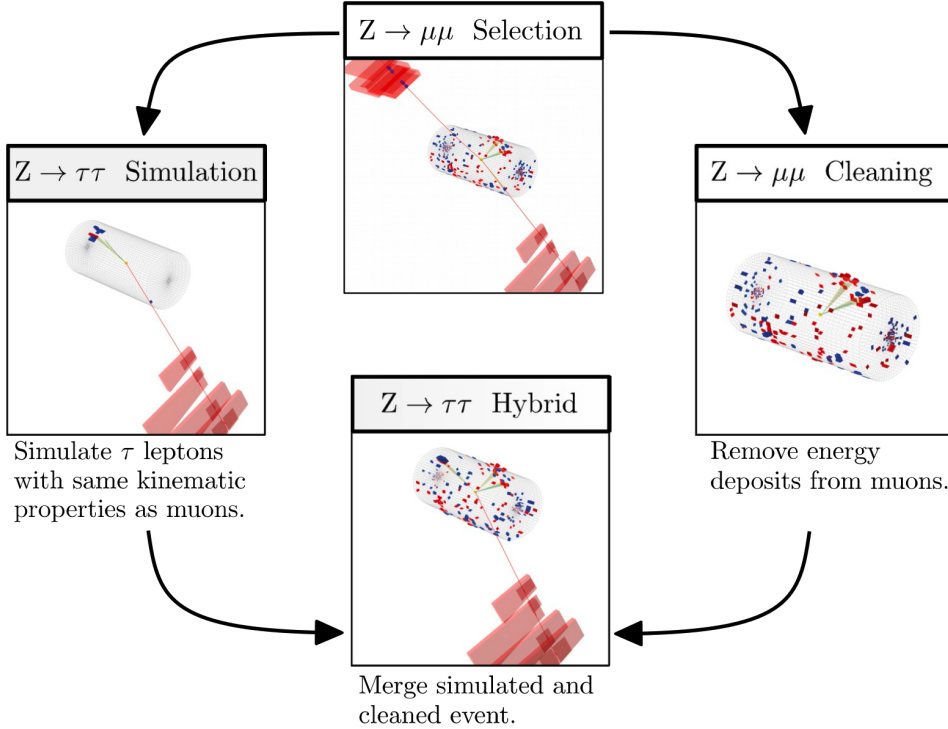


Figure 4.2: Schematic view of the four main steps of the embedding technique for τ leptons, as described in Section 4.3 [49]. A $Z \rightarrow \mu\mu$ event is selected in data ($Z \rightarrow \mu\mu$ selection), all of the energy deposits associated with the muons are removed ($Z \rightarrow \mu\mu$ cleaning), and two τ leptons and their decays are simulated in an empty detector ($Z \rightarrow \tau\tau$ simulation). Lastly, all energy deposits of the simulated τ decays are combined with the data event ($Z \rightarrow \tau\tau$ hybrid).

(sub-leading) muons, and a minimum requirement between 3.8 and 8.0 GeV on the invariant di-muon mass $m_{\mu\mu}$ [49]. The offline reconstructed muons must match the objects at trigger level and also have offline $p_T > 17(8)$ GeV. They must have $|\eta| < 2.4$ and be located at a distance $|d_z| < 0.2$ cm to the primary vertex along the beam axis. To form a Z boson candidate, each muon is required to originate from a global muon track. The muon pairs must have opposite charges with an invariant mass of $m_{\mu\mu} > 20$ GeV. If more than two di-muon pairs are found, the pair with the invariant mass closest to the Z boson mass (91.19 GeV) is chosen.

This selection is designed to be tight enough to ensure a high purity of genuine $\mu\mu$ events, and also loose enough to minimize biases of the embedded event samples. Isolation requirements are avoided, since they would introduce a bias towards less

1176 hadronic activity in the vicinities of the embedded leptons that will appear more
 1177 isolated than expected in data. The selection results in an expected mixture of events
 1178 summarized in Table 4.1 from [49]. $Z \rightarrow \mu\mu$ is the dominant process modeled by the
 1179 embedded technique, with $t\bar{t}$, QCD, and diboson and single top processes becoming
 1180 more significant when considering events with b-tag jets.

Process	Fraction (%)		
	Inclusive	$m_{\mu\mu} > 70$ GeV	$N(\text{b-tag jets}) > 0$
$Z \rightarrow \mu\mu$	97.36	99.11	69.25
QCD	0.84	0.10	2.08
$t\bar{t}$	0.78	0.55	25.61
$Z \rightarrow \tau\tau$	0.71	0.05	0.57
Diboson, single t	0.17	0.17	2.35
W+jets	0.08	0.02	0.14

Table 4.1: Expected event composition after selecting two muons in the embedded technique [49], before additional cuts (i.e. inclusive, *column 2*), and after adding a requirement on the di-muon mass $m_{\mu\mu} > 70$ GeV (*column 3*), or a requirement on the number of b-tag jets in the event (*column 4*).

1181 The advantage of the embedded technique is that aspects of the event that are
 1182 difficult to model and describe are directly taken from data, resulting in a better
 1183 data description than can be achieved with only the $Z \rightarrow \tau\tau$ simulation [49]. The
 1184 simulation must be tuned extensively to accurately model aspects of the data, such
 1185 as time-dependent pile-up profiles, the production of additional jets, e.g. in multijet
 1186 and vector boson fusion topologies, the number of reconstructed primary interaction
 1187 vertices, and the missing transverse momentum p_T^{miss} . Since all events with genuine
 1188 $\tau\tau$ are estimated with samples made with the embedded technique (referred to as
 1189 embedded samples from here on), events in Monte Carlo simulation with genuine $\tau\tau$
 1190 are not used, in order to avoid double-counting.

₁₁₉₁ **Chapter 5**

₁₁₉₂ **Object reconstruction and
1193 corrections applied**

₁₁₉₄ In the data processing workflow, data events and simulated events are analyzed to
₁₁₉₅ reconstruct physics objects of interest, and algorithms for distinguishing genuine par-
₁₁₉₆ ticle candidates from background, are employed. Section 5.1 describes the physical
₁₁₉₇ properties of the most important objects in the $h \rightarrow aa \rightarrow bb\tau\tau$ analysis: taus,
₁₁₉₈ muons, electrons, jets, and jets originating from b-quarks (b-flavor jets), as well as
₁₁₉₉ their reconstruction and identification in CMS. In this analysis, the full energy and
₁₂₀₀ momentum of the two tau leptons ($m_{\tau\tau}$) is estimated from the measured (i.e. visible)
₁₂₀₁ components of the tau leptons using the SVFit/FastMTT algorithm, which is de-
₁₂₀₂ scribed in Section 5.2. Corrections are applied to the simulated samples at the object
₁₂₀₃ level and the event level to account for known discrepancies between simulations and
₁₂₀₄ the data that the simulations are intended to model. These corrections are listed and
₁₂₀₅ detailed in Section 5.3.

₁₂₀₆ **5.1 Object reconstruction**

₁₂₀₇ **5.1.1 Taus**

₁₂₀₈ The tau (τ) is the heaviest known lepton. With a rest mass of 1776.86 MeV, it can
₁₂₀₉ decay to not only electrons and muons, but also hadrons. The mean lifetime of the τ
₁₂₁₀ is $\tau = 290 \times 10^{-15}$ seconds, corresponding to $c\tau = 87.03 \mu\text{m}$, which is short enough
₁₂₁₁ that taus decay in the CMS detector before reaching the detector elements.

₁₂₁₂ In two thirds of the cases, τ leptons decay hadronically, typically into one or three
₁₂₁₃ charged mesons (predominantly π^+ , π^-), often accompanied by neutral pions (that
₁₂₁₄ decay $\pi^0 \rightarrow \gamma\gamma$), and a ν_τ . These hadronic decays are denoted τ_h . In the remainder of
₁₂₁₅ the decays, the tau decays to the lighter leptons (electron or muon), termed leptonic
₁₂₁₆ decays. In all cases, at least one neutrino is produced, resulting in missing transverse
₁₂₁₇ energy in the CMS detector. The tau's largest decay branching ratios (proportional
₁₂₁₈ to probability of decay) are listed below [26]:

- ₁₂₁₉ • 17.8% decay to $e^- \bar{\nu}_e \nu_\tau$
- ₁₂₂₀ • 17.4% decay to $\mu^- \bar{\nu}_\mu \nu_\tau$
- ₁₂₂₁ • 25.5% decay to $\pi^- \pi^0 \nu_\tau$ (ρ^- resonance at 770 MeV)
- ₁₂₂₂ • 10.8% decay to $\pi^- \nu_\tau$
- ₁₂₂₃ • 9.3% decay to $\pi^- \pi^0 \pi^0 \nu_\tau$ (a_1^- resonance at 1200 MeV)
- ₁₂₂₄ • 9.0% decay to $\pi^- \pi^- \pi^+ \nu_\tau$ (a_1^- resonance at 1200 MeV)

₁₂₂₅ The neutrinos escape undetected from the CMS detector and are not considered
₁₂₂₆ in the reconstruction. Charged hadrons leave tracks in the tracking detector before
₁₂₂₇ being absorbed in the hadronic calorimeter; in CMS tau reconstruction terminology,
₁₂₂₈ they are often called “prongs”, i.e. the dominant τ_h decay modes are termed “1 prong”

₁₂₂₉ (π^\pm) , “1 prong + π^0 (s)”, and “3-prong”. Neutral pions decay to two photons which
₁₂₃₀ lose their energy in the electromagnetic calorimeter. Taus that decay to electrons
₁₂₃₁ and muons, are typically triggered on and reconstructed as electrons and muons
₁₂₃₂ respectively.

₁₂₃₃ **Hadron plus strips (HPS) reconstruction of τ_h**

₁₂₃₄ At CMS, hadronically decaying tau leptons are reconstructed with the hadron plus
₁₂₃₅ strips (HPS) algorithm [52] [53]. The HPS algorithm capitalizes on photon conversions
₁₂₃₆ in the CMS tracker material, which originate from the neutral pion (π^0) decaying
₁₂₃₇ to two photons. The bending of electron/positron tracks due to the CMS solenoid
₁₂₃₈ magnetic field leads to a spread of the neutral pions’ calorimeter signatures in the ϕ
₁₂₃₉ direction. This motivates the reconstruction of photons in “strips”: objects that are
₁₂₄₀ built out of PF photons and electrons. The strip reconstruction starts with centering
₁₂₄₁ a strip on the most energetic electromagnetic particle in a PF jet. Among other
₁₂₄₂ electromagnetic particles located in a window of size $\Delta\eta = 0.05$ and $\Delta\phi = 0.20$
₁₂₄₃ around the strip center, the most energetic one is associated with the strip and its
₁₂₄₄ momentum is added to the strip momentum. This is repeated iteratively until no
₁₂₄₅ further particles can be associated. Lastly, strips satisfying a requirement of $p_T^{\text{strip}} > 1$
₁₂₄₆ GeV are combined with charged hadrons to reconstruct individual τ_h decay modes,
₁₂₄₇ where h stands for both π and K :

- ₁₂₄₈ • *Single hadron:* $h^- \nu_\tau$ and $h^- \pi^0 \nu_\tau$ decay modes, in which the neutral pions have
₁₂₄₉ too little energy to be reconstructed as strips.
- ₁₂₅₀ • *One hadron + one strip:* $h^- \pi^0 \nu_\tau$ decay modes, where the photons from the π^0
₁₂₅₁ decay are close together in the calorimeter.
- ₁₂₅₂ • *One hadron + two strips:* $h^- \pi^0 \nu_\tau$ decay modes, where the photons from the π^0
₁₂₅₃ decay are well separated.

- 1254 • *Three hadrons:* $h^- h^+ h^- \nu_\tau$ decay modes. The three charged hadrons are re-
1255 quired to originate from the same secondary vertex.

1256 The $h^- \pi^0 \pi^0 \nu_\tau$ and $h^- h^+ h^- \pi^0 \nu_\tau$ decay modes do not have their own treatment are
1257 reconstructed with the above topologies.

1258 In the HPS algorithm, the direction of the reconstructed tau momentum \vec{p}^{τ_h}
1259 is required to fall within a distance of $\Delta R = 0.1$ from the original PF jet. All
1260 charged hadrons and strips are required to be contained within a cone of size $\Delta R =$
1261 $(2.8 \text{ GeV})/p_T^{\tau_h}$, from the τ_h as reconstructed by the HPS.

1262 All charged hadrons are assumed to be pions, and they are required to be consis-
1263 tent with the masses of the intermediate meson resonances (if applicable), with the
1264 following allowed windows for candidates: 50-200 MeV for π^0 , 0.3-1.3 GeV for ρ , and
1265 0.8-1.5 GeV for a_1 . If the τ_h decay is compatible with more than one hypothesis, the
1266 one giving the highest $p_T^{\tau_h}$ is chosen. Lastly, an isolation requirement is applied: aside
1267 from the τ_h decay products, no charged hadrons or photons can be present within
1268 an isolation cone of size $\Delta R = 0.5$ around the direction of the τ_h . The outputs of
1269 the HPS algorithm are the reconstructed decay mode and the visible four-momentum
1270 (i.e. the four-momenta of all decay products excluding the neutrinos).

1271 **DeepTau for identifying τ_h**

1272 The identification of τ_h candidates in CMS has historically been divided into separate
1273 discriminators against jets, electrons, and muons. Discriminators versus jets and
1274 electrons use information from derived quantities, such as the p_T sum of particles
1275 near the τ_h axis. Building on the previous multivariate analysis (MVA) classifier [54]
1276 based on a boosted decision tree (BDT), DeepTau is a more recent classifier based on a
1277 deep neural network (DNN) that simultaneously discriminates against jets, electrons,
1278 and muons. The DNN uses a combination of high-level inputs, similar to previous
1279 algorithms, and also uses convolutional layers in η - ϕ space to process information

1280 from all reconstructed particles near the τ_h axis. Convolutional layers are based on
1281 the principle that an image can be processed independently of its position.

1282 The final DeepTau discriminators against jets, muons, and electrons are given by

$$D_\alpha(y) = \frac{y_\tau}{y_\tau + y_\alpha} \quad (5.1)$$

1283 where y_τ (y_α) are estimates of the probabilities for the τ_h candidate to come from
1284 a genuine τ_h (jet, μ , e). Working points for each discriminator with different τ_h
1285 identification efficiencies are defined for D_e , D_μ , and D_{jet} , for usage in physics analyses
1286 and derivation of data-to-simulation corrections [55].

1287 5.1.2 Muons

1288 Muons are the next lightest lepton after taus, with a mass of 105.66 MeV and a
1289 mean lifetime of $\tau = 2.20 \times 10^{-6}$ seconds, or $c\tau = 658.64$ m. At CMS, muons are
1290 identified with requirements on the quality of the track reconstruction and on the
1291 number of measurements in the tracker and the muon systems [56]. In the standard
1292 CMS reconstruction, tracks are first reconstructed independently in the inner tracker
1293 (tracker track) and in the muon system (standalone-muon track). Next, these tracks
1294 are processed in two different methods.

1295 The first is Global Muon reconstruction (outside-in) [56], which fits combined hits
1296 from the tracker track and standalone-muon track, using the Kalman-filter technique.
1297 At large transverse momenta, $p_T \gtrsim 200$ GeV, the global-muon fit can improve the
1298 momentum resolution compared to the tracker-only fit.

1299 The second is Tracker Muon reconstruction (inside-out) [56], which starts with
1300 tracker tracks with $p_T > 0.5$ GeV and total momentum $p_T > 2.5$ GeV. These tracks
1301 are extrapolated outwards to the muon system and matched to detector segments
1302 there, taking into account the magnetic field, expected energy losses, and multiple

1303 Coulomb scattering in the detector material. Tracker Muon reconstruction is more
 1304 efficient than the Global Muon reconstruction at low momenta, $p \lesssim 5$ GeV, because
 1305 it only requires a single muon segment in the muon system, whereas Global Muon
 1306 reconstruction typically requires segments in at least two muon stations.

1307 To further suppress fake muons from decay in flight, isolation cuts are used. A
 1308 relative isolation variable is defined to quantify the energy flow of particles near the
 1309 muon trajectory. A relative isolation is defined similarly for muons and electrons:

$$I^\ell \equiv \frac{\sum_{\text{charged}} p_T + \max\left(0, \sum_{\text{neutral}} p_T - \frac{1}{2} \sum_{\text{charged, PU}} p_T\right)}{p_T^\ell} \quad (5.2)$$

1310 where $\sum_{\text{charged}} p_T$ is the scalar sum of the p_T of the charged particles originating from
 1311 the primary vertex and located in a cone of size $\Delta R = \sqrt{(\Delta\eta)^2 + (\Delta\phi)^2} = 0.4(0.3)$
 1312 centered on the direction of the muon (electron). The sum $\sum_{\text{neutral}} p_T$ is the equivalent
 1313 for neutral particles. The sum $\sum_{\text{charged, PU}} p_T$ is the scalar sum of the p_T of the
 1314 charged hadrons in the cone originating from pile-up vertices. The factor 1/2 comes
 1315 from simulation estimations, which find that the ratio of neutral to charged hadron
 1316 production in the hadronization process of inelastic pp collisions is 1/2. Thus the
 1317 subtracted term is intended to subtract contribution from pile-up, from the neutral
 1318 particle contribution to the isolation sum. Finally, this is divided by the lepton
 1319 transverse momentum, p_T^ℓ .

1320 5.1.3 Electrons

1321 Electrons are the lightest lepton with a mass of 0.511 MeV. At CMS, electrons are
 1322 reconstructed by associating a track reconstructed in the silicon tracking detector
 1323 with a cluster of energy in the ECAL. Performance is maximized via a combination
 1324 of a stand-alone approach and the complementary global particle-flow approach [57].

1325 In the stand-alone approach, the electron energy, which is typically spread over

several crystals of the ECAL, is clustered with the “hybrid” algorithm in the barrel and the “multi- 5×5 ” in the endcaps [57]. The hybrid algorithm collects energy in a small window in η and an extended window in ϕ . It identifies a seed crystal, and adds arrays of 5×1 crystals in $\eta \times \phi$ in a range of $N = 17$ crystals in both directions of ϕ , if their energies exceed a minimum threshold, thus forming a supercluster (SC). In the endcap, crystals are not arranged in an $\eta \times \phi$ geometry; instead clusters are build around seed crystals in clusters of 5×5 crystals that can partly overlap. Nearby clusters are grouped into a supercluster, and energy is recovered from associated deposits in the preshower.

In the PF reconstruction [57], PF clusters are reconstructed by aggregating around a seed all contiguous crystals with energies two standard deviations above the electronic noise observed at the beginning of a data-taking run. The energy of a given crystal can be shared among two or more clusters.

The electron track reconstruction is performed in two ways [57]: the ECAL-based seeding, which begins with the SC energy and positioning, and the tracker-based seeding (part of the PF reconstruction algorithm), which uses tracks reconstructed from the general algorithm for charged particles, extrapolated towards the ECAL and matched to an SC. Kalman filter (KF) tracks with a small number of hits or that are not well-fitted, are re-fitted with a dedicated Gaussian sum Filter (GSF).

A global identification variable [57] is defined using a multivariate analysis (MVA) technique that combines information on track observables (kinematics, quality of the KF track and GSF track), the electron PF cluster observables (shape and pattern), and the association between the two (geometric and kinematic observables). For electrons seeded only through the tracker-based approach, a weak selection is applied on this MVA variable. For electrons seeded through both approaches, a logical OR is taken.

Electron isolation, i.e. the presence of energy deposits near the electron trajectory,

is a separate key handle in rejecting significant background. Compared to isolated electrons, electrons from misidentified jets or genuine electrons within a jet resulting from semileptonic decays of b or c quarks tend to have significant energy deposits near the primary trajectory [57]. Offline analyses benefit from the PF technique for defining isolation, which sums the PF candidates reconstructed located within a specified isolation cone around the electron candidate, as in Eqn. 5.2.

5.1.4 Jets

The vast majority of processes of interest at the LHC contains quarks or gluons in the final state, but these particles cannot be observed directly. In a process called hadronization, they fragment into spatially-grouped collections of particles called jets, which can be detected in the tracking and calorimeter systems. Hadronization and the subsequent decays of unstable hadrons can produce hundreds of nearby particles in the CMS detector. Jets are reconstructed by the PF algorithm (PF jets), or from the sum of the ECAL and HCAL energies deposited in the calorimeter towers (Calo jets). In PF jets, typically used in offline analyses, jets are built using the anti- k_T (AK) clustering algorithm [58]. The anti- k_T algorithm iterates over particle pairs and finds the two that are closest in a distance measure d , and determines whether to combine them:

$$d_{ij} = \min(p_{T,i}^{-2}, p_{T,j}^{-2}) \frac{\Delta_{ij}^2}{R^2}, \text{ combine when } d_{ij} < p_{T,i}^{-2}; \text{ stop when } d_{ij} > p_{T,i}^{-2} \quad (5.3)$$

where $\Delta_{ij}^2 = (\eta_i - \eta_j)^2 + (\phi_i - \phi_j)^2$ and $p_{T,i}$, η_i , ϕ_i are the transverse momentum, rapidity, and azimuthal angle of particle i . The power -2 means that higher-momentum particles are clustered first, leading to jets that tend to be centered on the hardest (highest p_T) particle.

There are several methods to remove contributions of pile-up collisions from jet

1376 clustering [59]:

- 1377 • Charged hadron subtraction (CHS), which removes all charged hadron candidates associated with a track that is not associated with the primary vertex.
- 1379 • PileUp Per Particle Identification (PUPPI), which weighs input particles based
1380 on their likelihood of arising from pile-up. QCD particles tend to have a collinear
1381 structure, compared to soft diffuse radiation coming from pile-up. The local
1382 shape for charged pile-up, used as a proxy for all pile-up particles, is used on an
1383 event-by-event basis to calculate a weight for each particle. PUPPI is deployed
1384 in Run-2 and is more performant than CHS in high pile-up scenarios.

1385 **5.1.5 B-flavored jets**

1386 Jets that arise from bottom-quark hadronization (b-flavor jets) have overwhelming
1387 background from processes involving jets from gluons (g) and light-flavor quarks (u, d,
1388 s), and from c-quark fragmentation. The ability to identify b-flavor jets, or b-tagging,
1389 exploits the b hadrons' relatively large masses, long lifetimes, and daughter particles
1390 with hard momentum spectra [58].

1391 The impact parameter (IP) of a track is the 3-dimensional distance between the
1392 track and the primary vertex (PV) at the point of closest approach. The IP is positive
1393 if the track originates from the decay of particles travelling along the jet axis. The
1394 resolution of the IP depends on the p_T and η of the track, motivating the use of the
1395 impact parameter significance S_{IP} (ratio of the IP to its estimated uncertainty) as an
1396 observable [58].

1397 Because of the large but finite lifetimes of the b hadrons, b hadrons tend to
1398 travel a short distance before decaying at a secondary vertex (SV), which can be
1399 measured and reconstructed separately from the primary vertex due to the excellent
1400 position resolution of the pixel detector [58]. Previous b-tagging algorithms (e.g.

1401 CSV, cMVAv2, and DeepCSV) have capitalized on variables such as the presence of
1402 a SV, the flight distance and direction (computed from the vector between the PV
1403 and the SV), and kinematics of the system of associated secondary tracks (e.g. track
1404 multiplicity, mass, and energy).

1405 The DeepJet (formerly known as DeepFlavour) algorithm [60] is a deep-neural-
1406 network multi-classification algorithm, which uses 16 properties of up to 25 charged
1407 and 6 properties of 25 neutral particle-flow jet constituents, as well as 17 properties
1408 from up to 4 secondary vertices associate with the jet. Compared to the previous clas-
1409 sifying algorithm DeepCSV, DeepJet has been demonstrated to have higher efficiency
1410 with lower misidentification probability in Phase-1 data [61].

1411 5.2 Reconstruction of the $\tau\tau$ mass

1412 The final signal extraction is done to the total $\tau\tau$ mass, which is estimated from the
1413 visible $\tau\tau$ mass using the FastMTT algorithm [62]. FastMTT is based on the SVFit
1414 algorithm, originally developed for the Standard Model $H \rightarrow \tau\tau$ analysis [63]. Both
1415 the SVFit algorithms, and the FastMTT algorithm, are described below, to give a
1416 complete picture of how tau decays are parameterized.

1417 To specify a hadronic τ decay, six parameters are needed [63]: the polar and
1418 azimuthal angles of the visible decay product system in the τ rest frame, the three
1419 boost parameters from the τ rest frame to the laboratory frame, and the invariant
1420 mass m_{vis} of the visible decay products. For a leptonic τ decay, two neutrinos are
1421 produced, and a seventh parameter, the invariant mass of the two-neutrino system, is
1422 necessary. The unknown parameters are constrained by four observables that are the
1423 components of the four-momentum of the system formed by the visible decay products
1424 of the τ lepton, measured in the laboratory frame. The remaining unconstrained
1425 parameters for hadronic and leptonic τ decays are thus:

- The fraction of the τ energy in the laboratory frame carried by the visible decay

1426 products,

- ϕ , the azimuthal angle of the τ direction in the laboratory frame,

- $m_{\nu\nu}$, the invariant mass of the two-neutrino system in leptonic τ decays (for hadronic τ decays, $m_{\nu\nu}$ is set to 0).

1431 E_x^{miss} and E_y^{miss} , the x and y components of the missing transverse energy E_T^{miss}
1432 provide two further constraints.

1433 5.2.1 Original SVFit ‘‘standalone’’: maximum likelihood

1434 In one of the original versions of SVFit, called ‘‘standalone’’ SVFit [63], a maximum
1435 likelihood fit method is used to reconstruct the mass $m_{\tau\tau}$ by combining the measured
1436 observables E_x^{miss} and E_y^{miss} with a likelihood model that includes terms for the τ
1437 decay kinematics and the E_T^{miss} resolution [63]. The likelihood function $f(\vec{z}, \vec{y}, \vec{a}_1 \vec{a}_2)$
1438 of the parameters $\vec{z} = (E_x^{\text{miss}}, E_y^{\text{miss}})$ in an event is constructed, where the remaining
1439 parameters are the kinematics of the two τ decays, denoted $\vec{a}_1 = (x_1, \phi_1, m_{\nu\nu,1})$ and
1440 $\vec{a}_2 = (x_2, \phi_2, m_{\nu\nu,2})$, and the four-momenta of the visible decay products with the
1441 measured values $\vec{y} = (p_1^{\text{vis}}, p_2^{\text{vis}})$.

1442 The likelihood f is the product of three likelihood functions. The first two likelihood
1443 functions model the decay parameters \vec{a}_1 and \vec{a}_2 of the two τ leptons. For leptonic
1444 decays, the likelihood function is modeled using matrix elements for τ decays,
1445 and integrated over the allowed phase space $0 \leq x \leq 1$ and $0 \leq m_{\nu\nu} \leq m_\tau \sqrt{1-x}$. For
1446 hadronic τ decays, a model based on the two-body phase space is used and integrated
1447 over $m_{\text{vis}}^2/m_{\tau\tau}^2 \leq x \leq 1$. The third likelihood function quantifies the compatibility of
1448 a τ decay hypothesis with the reconstructed \vec{E}_T^{miss} in an event, assuming the neutrinos
1449 are the only source of missing transverse energy. The expected \vec{E}_T^{miss} resolution

1450 is represented by a covariant matrix, estimated on an event-by-event basis using a
1451 significance algorithm [64].

1452 5.2.2 “Classic SVFit” with matrix element

1453 Classic SVFit is an improved algorithm of the original “standalone” SVFit using the
1454 formalism of the matrix element (ME) method [62]. In the ME method, an estimate
1455 for the unknown model parameter Θ (here, the mass $m_{\tau\tau}$) is obtained by maximizing
1456 the probability density \mathcal{P} . The key ingredients of the probability density are the
1457 squared modulus of the matrix element $|\mathcal{M}(\mathbf{p}, \Theta)|^2$ and the transfer function $W(\mathbf{y}|\mathbf{p})$
1458 (probability density to observe the measured observables \mathbf{y} given the phase space
1459 point \mathbf{p}). The best estimate $m_{\tau\tau}$ is obtained by computing the probability density \mathcal{P}
1460 for a range of mass hypotheses and finding the value of $m_{\tau\tau}$ that maximizes \mathcal{P} .

1461 Distributions illustrating the performance of the classic matrix element SVFit
1462 algorithm are shown in Fig. 5.1 from [62], showing the di-tau mass after and before
1463 application of SVFit to recover energy lost to neutrinos. The SVFit algorithm is
1464 found to improve the sensitivity of the Standard Model $H \rightarrow \tau\tau$ analysis performed
1465 by CMS by about 30%, compared to performing the same analysis using only the
1466 visible mass m_{vis} .

1467 5.2.3 FastMTT: optimized SVFit

1468 FastMTT [65] is a further simplification to the matrix element method of Classic
1469 SVFit which has comparable performance but is about 100 times faster. FastMTT
1470 drops the matrix element component of the computation without significant impact
1471 on the final mass resolution, and simplifies the computation of the transfer functions.
1472 The opening angle of the τ decay products with respect to the initial τ momenta ap-
1473 proaches 0 for τ with high $\gamma = E_\tau/m_\tau$, with typical τ decays from the Z boson decays
1474 already satisfying this condition. In this collinear approximation, the dimensionality

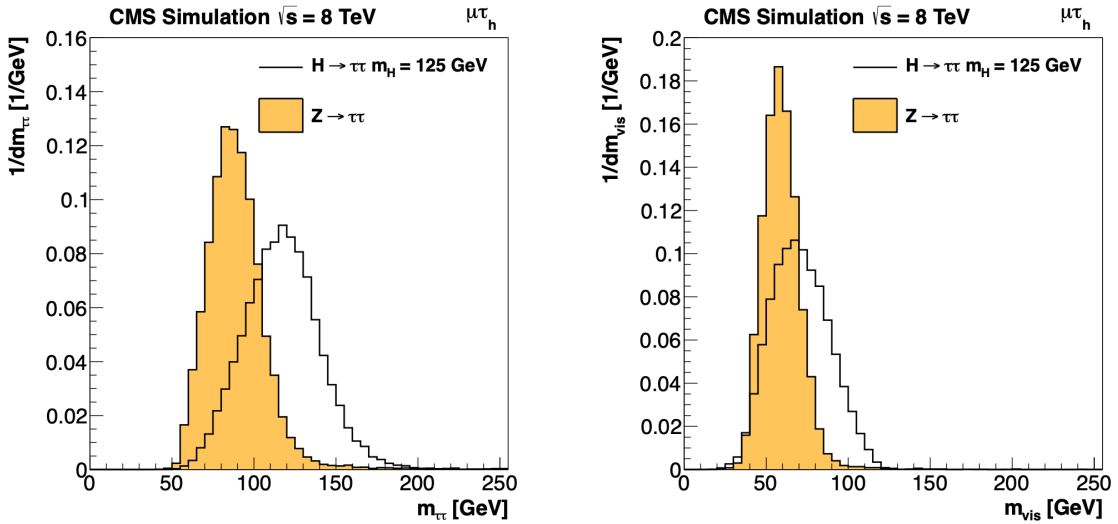


Figure 5.1: Distributions from [62], of $m_{\tau\tau}$ after reconstruction with the original SVFit algorithm (*left*), and before SVFit with only the visible tau decay products (*right*), for $H \rightarrow \tau\tau$ signal events of mass $m_H = 125$ GeV (*black line*) and the $Z/\gamma^* \rightarrow \tau\tau$ background (*orange, solid*), in the decay channel $\tau\tau \rightarrow \mu\tau_h$.

1475 of the transfer function can be reduced in the computation of FastMTT, while still
1476 yielding similar results to Classic SVFit [65].

1477 5.3 Corrections applied to simulation

1478 Corrections are applied to simulated samples to account for known effects in the event
1479 modeling and reconstruction and data-taking, and are intended to bring simulations
1480 in closer agreement with data. Corrections fall into two broad categories: *energy*
1481 *scale corrections* applied to physics objects, and *event-level corrections*. Energy scale
1482 corrections are multiplicative factors applied to the energy and transverse momentum
1483 p_T of simulated objects (e.g. leptons or jets), and bring the average reconstructed en-
1484 ergies of simulated particles into better agreement with those of objects reconstructed
1485 from data. Event-level corrections are applied as a per-event multiplicative weight,
1486 and account for effects such as mis-modeling in simulations of the underlying physics
1487 process, or changing detector operating conditions during data-taking. Event-level

1488 corrections change the shapes of the distributions of all the physical observables.

1489 Uncertainties in scale factors and corrections are also sources of systematic errors
1490 in the analysis, detailed in Chapter 8. Systematic uncertainties in the tau, muon, and
1491 electron energy scales can shift the p_T of the leptons up or down, which can change
1492 whether events pass or fail the offline p_T thresholds for the trigger paths described in
1493 the previous section, i.e. change the number of events in the signal region.

1494 5.3.1 Tau energy scale

1495 An energy scale is applied to the transverse momentum p_T and mass of the hadronic
1496 tau τ_h in the $\mu\tau_h$ and $e\tau_h$ channels, to correct for a deviation of the average recon-
1497 structed τ_h energy from the generator-level energy of the visible τ_h decay products.
1498 These correction factors are derived centrally [54], by fitting to events in $e\tau_h$ and $\mu\tau_h$
1499 final states in Z/γ^* events separately for the h^\pm , $h^\pm\pi^0$, and $h^\pm h^\mp h^\pm$ decays. The
1500 values used are shown in Table 5.1.

1501 When applying the energy scale to the τ_h , the 4-momentum of the missing trans-
1502 verse energy (MET) is adjusted such that the total 4-momenta of the τ_h and the MET
1503 remains unchanged [66].

Tau energy scale factor				
Decay mode	2018	2017	2016 pre-VFP	2016 post-VFP
0	0.991 ± 0.008	0.986 ± 0.009	0.987 ± 0.01	0.993 ± 0.009
1	1.004 ± 0.006	0.999 ± 0.006	0.998 ± 0.006	0.991 ± 0.007
10	0.998 ± 0.007	0.999 ± 0.007	0.984 ± 0.008	1.001 ± 0.007
11	1.004 ± 0.009	0.996 ± 0.01	0.999 ± 0.011	0.997 ± 0.016

Table 5.1: Energy scales applied to genuine hadronic tau decays τ_h by data-taking year/era and decay mode, along with systematic errors.

1504 **5.3.2 Muon energy scale**

1505 An energy scale is applied to the p_T and mass of genuine muons from τ decays in the
1506 $e\mu$ and $\mu\tau_h$ channels [67]. The applied values are the same for MC and embedded
1507 samples and are shown in Table 5.2. Following the SM $H \rightarrow \tau\tau$ analysis, Rochester
1508 corrections are not applied, and instead prescriptions from [68] are followed.

Muon energy scale factor	
Eta range	Value for all years
$ \eta \in [0.0, 1.2)$	1.0 ± 0.004
$ \eta \in [1.2, 2.1)$	1.0 ± 0.009
$ \eta \in [2.1, 2.4)$	1.0 ± 0.027

Table 5.2: Energy scales and systematic errors applied to genuine muons. The values are the same for MC and embedded for all years [69] [68].

1509 **5.3.3 Electron energy scale**

1510 Corrections to the electron energy scale are applied to genuine e from τ decays, and
1511 are binned in two dimensions by electron p_T and η for barrel vs. endcap [70]. The
1512 scale factors are binned in p_T and η for MC samples: e.g. values for 2018 are shown
1513 in Fig. 5.2 from [71]. For embedded samples the electron energy scale is taken as
1514 only binned in η (Table 5.3).

Electron energy scale factor for embedded samples			
Eta range	2018	2017	2016
$ \eta \in [0.0, 1.479)$	0.973 ± 0.005	0.986 ± 0.009	0.9976 ± 0.0050
$ \eta \in [1.479, 2.4)$	0.980 ± 0.0125	0.887 ± 0.0125	0.993 ± 0.0125

Table 5.3: Energy scales and systematic errors applied to electrons in embedded samples, binned in the electron η , by data-taking year [72] [73] [74].

1515 **5.3.4 τ_h identification efficiency**

1516 The τ_h identification efficiency can differ in data and MC [66]. Recommended correc-
1517 tions are provided by the Tau POG, and we use the medium DeepTau vs. jet working

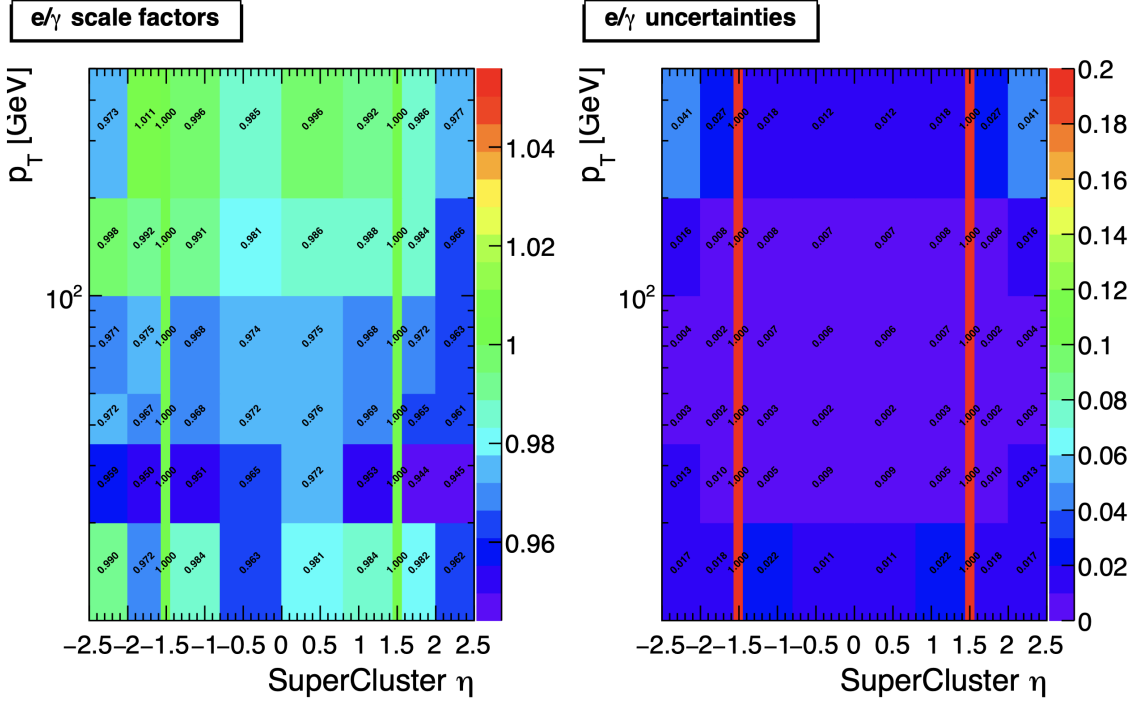


Figure 5.2: Electron/photon energy scale factors (*left*) and corresponding uncertainties (*right*) binned in the electron η and p_T , for the data-taking year 2018 [71].

1518 point values. The identification efficiency is measured in $Z \rightarrow \tau\tau$ events in the $\mu\tau_h$
 1519 final state, and is binned in p_T due to clear p_T dependence of the DeepTau ID.

Tau ID efficiency for DeepTau Medium vs. jet WP in 2018						
p_T (GeV)	< 20	(20, 25]	(25, 30]	(30, 35]	(35, 40]	(40, 500]
Central value	0	0.945	0.946	0.916	0.921	1.005
Up value	0	1.001	0.981	0.946	0.950	1.035
Down value	0	0.888	0.981	0.883	0.893	0.953

Table 5.4: Tau ID efficiency for the DeepTau vs. jet medium working point, with central, up, and down values for 2018, binned in the tau p_T [66].

1520 5.3.5 Trigger efficiencies

1521 Scale factors are applied to correct for differences in trigger efficiencies between MC
 1522 and embedded vs. data, with values taken from tools provided by the Standard Model
 1523 $H \rightarrow \tau\tau$ working group which uses the same trigger paths [69]. In the following

1524 sections we review relevant trigger efficiencies in data, which form the basis of the
1525 trigger efficiency corrections applied to MC and embedded.

1526 **5.3.6 Tau trigger efficiencies**

1527 The efficiencies in data of the single- τ_h leg in $\mu\tau_h$, $e\tau_h$, and di- τ_h triggers is computed
1528 centrally per using a Tag and Probe (TnP) method [75] which is outlined here. In
1529 this method, $Z \rightarrow \tau\tau \rightarrow \mu\tau_h$ are selected in data and a Drell-Yan simulated sample
1530 ($Z \rightarrow \ell\ell, \ell = e, \mu, \tau_h$) with high purity. Cuts are applied to reject events not in this
1531 final state, e.g. suppressing $Z \rightarrow \mu\mu$ by vetoing events with a single loose ID muon.
1532 An isolated muon candidate (the tag) with online $p_T > 27$ GeV and $|\eta| < 2.1$ is
1533 identified and matched to an offline μ . An offline τ_h candidate (the probe) is selected,
1534 which is separated from the tag μ , and has $p_T > 20$ GeV and $|\eta| < 2.1$. The probe
1535 τ_h must pass anti-muon and anti-electron discriminators to avoid fakes from muons
1536 and electrons, and must pass the medium MVA tau isolation to suppress fakes from
1537 QCD jets. The trigger efficiency in the TnP method is calculated as

$$\text{Efficiency} = \frac{\text{Number of events passing the TnP selection with fires the HLT path}}{\text{Number of events passing the TnP selection}} \quad (5.4)$$

1538 The efficiencies for the hadronic tau legs in the relevant channels of this analyses
1539 ($\mu\tau_h$ and $e\tau_h$) as a function of the offline tau p_T and η , are shown for data taken in
1540 2016, 2017, and 2018 in Figures 5.3a and 5.3b [75] [76]. In both figures, the different
1541 HLT thresholds and differences in the L1 seed result in higher efficiencies in 2016 and
1542 differences in shapes of the 2016 efficiencies compared to 2017 and 2018. The low
1543 pile-up in 2016 also leads to higher efficiencies in that year.

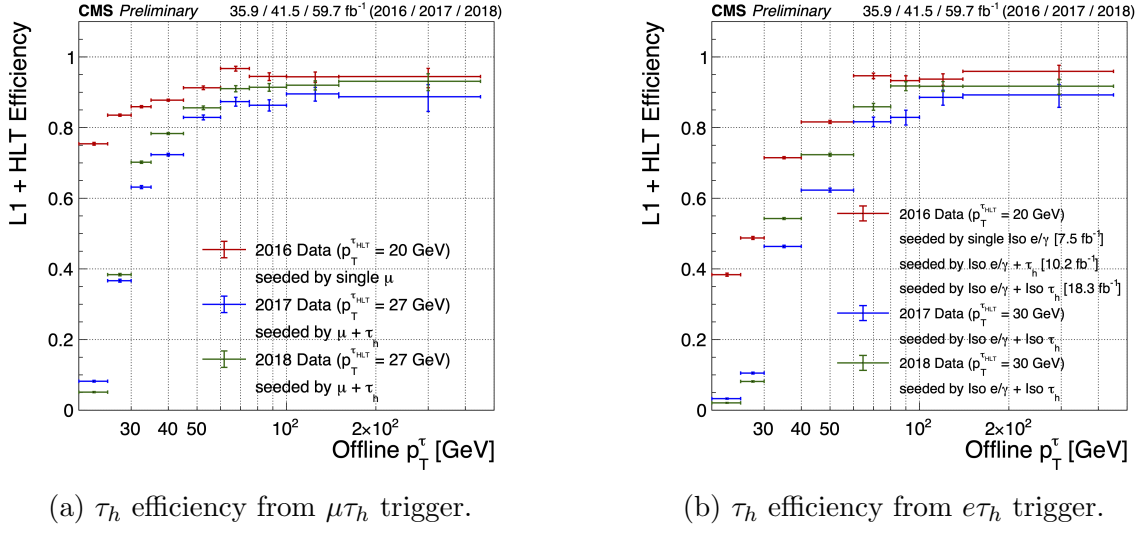
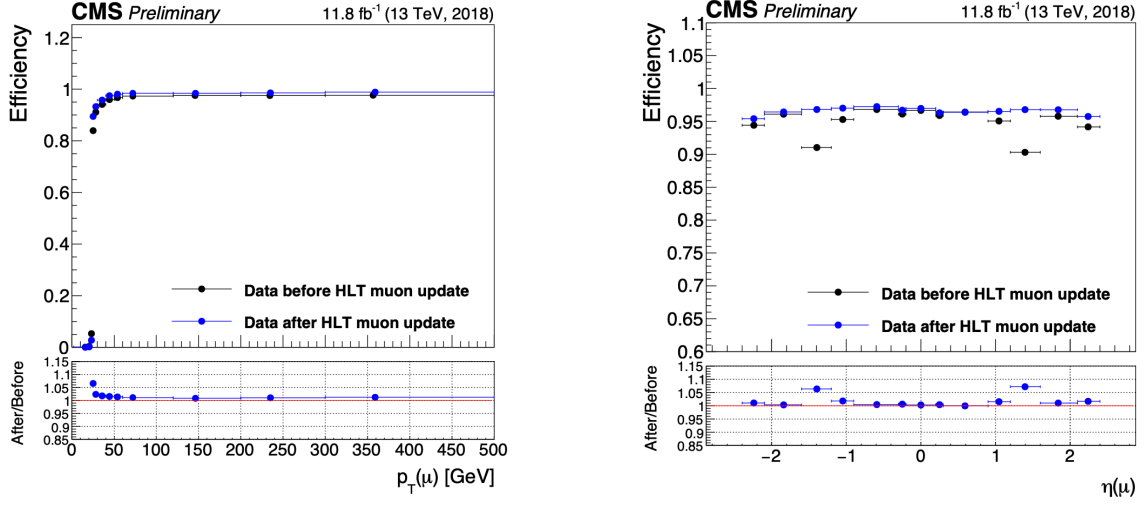


Figure 5.3: Hadronic tau leg efficiency of the cross-triggers for $\mu\tau_h$ (left) and $e\tau_h$ (right) triggers as a function of offline tau p_T for the years 2016 (red), 2017 (blue) and 2018 (green), from [76]. HLT p_T thresholds and L1 seeds are indicated in the legends.

1544 5.3.7 Single muon trigger efficiencies

1545 The efficiencies for the single isolated muon trigger with $p_T > 24 \text{ GeV}$ used in this
 1546 analysis, is shown for the data-taking year 2018 in Fig. 5.4a as a function of the muon
 1547 p_T and as a function of the muon $|\eta|$ in Fig. 5.4b from [77]. The data is split with
 1548 respect to a HLT muon reconstruction update that was deployed on 15/05/2018. A
 1549 small asymmetry in efficiencies between negative and positive η in Fig. 5.4b is due to
 1550 disabled muon chambers (CSCs). The efficiencies shown are estimated using a Tag
 1551 and Probe method using $Z \rightarrow \mu\mu$ events, with the tag being an offline muon with
 1552 $p_T > 29 \text{ GeV}$ and $|\eta| < 2.4$ passing a tight ID criteria, and the probe is an online (L1)
 1553 trigger object with $\Delta R < 0.3$ and passing tight ID and Particle Flow based isolation
 1554 requirements with $p_T > 26 \text{ GeV}$.



(a) Muon efficiency vs p_T for SingleMuon.

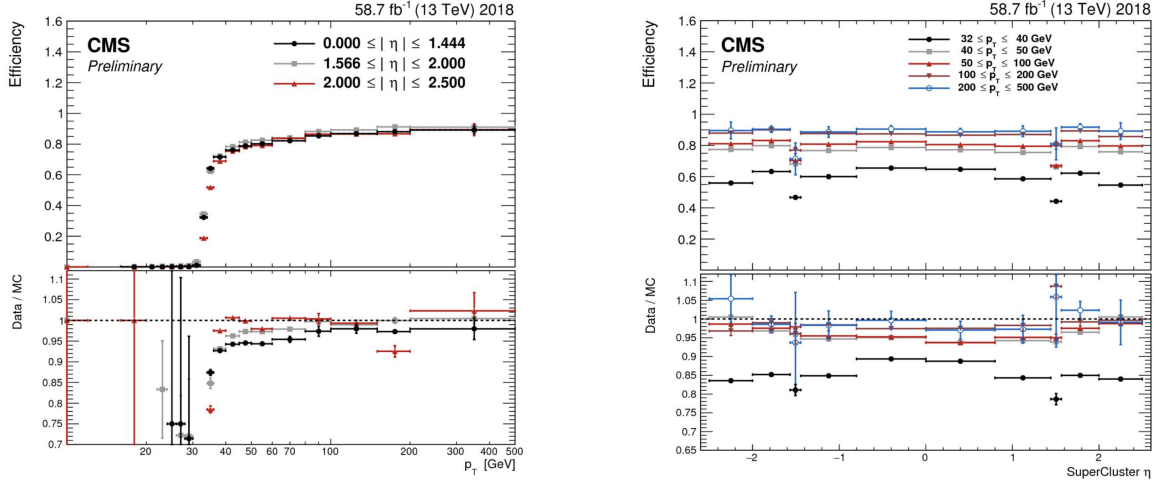
(b) Muon efficiency vs $|\eta|$ for SingleMuon.

Figure 5.4: Trigger efficiencies in data (*top panels*) and ratio of efficiencies after/before a HLT muon reconstruction update (*bottom panels*) for the muon in the isolated single muon trigger with threshold $p_T > 24$ GeV in the data-taking year 2018, as functions of the muon p_T (*left*) and muon $|\eta|$ (*right*). Only statistical errors are shown [77].

5.3.8 Single electron trigger efficiencies

The efficiencies in data, and the ratio between data and MC, of the single electron HLT trigger with p_T threshold 32 GeV used in this analysis are shown for 2018, as a function of the electron p_T in Fig. 5.5a and of the electron $|\eta|$ in Fig. 5.5b, from [78]. In the Tag and Probe method used for the 2018 dataset, the tag is an offline reconstructed electron with $|\eta| \leq 2.1$ and not in the barrel and endcap overlap region, with $p_T > 35$ GeV with tight isolation and shower shape requirements, firing the tag trigger. The probe is an offline reconstructed electron with $|\eta| \leq 2.5$ with $E_T^{\text{ECAL}} > 5$ GeV with no extra identification criteria [78].

The disagreement between data and MC, particularly at low transverse momentum, is in part due to detector effects that are difficult to simulate, such as crystal transparency losses in the ECAL and the evolution of dead regions in the pixel tracker [78].



(a) Electron efficiency vs p_T for single electron.

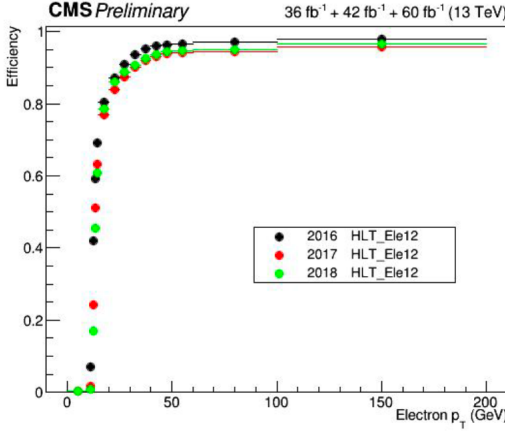
(b) Electron efficiency vs $|\eta|$ for single electron.

Figure 5.5: Trigger efficiencies in data, and the data/MC ratio for the electron in the single electron trigger with threshold $p_T > 32$ GeV in the data-taking year 2018, as functions of the electron p_T (*left*) and electron $|\eta|$ (*right*) [78]. In the plot vs. p_T , the region $1.442 \leq |\eta| \leq 1.566$ is not included as it corresponds to the transition between barrel and endcap parts of the ECAL.

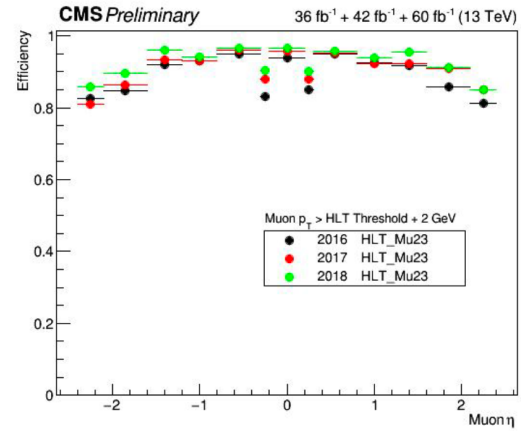
1568 5.3.9 $e\mu$ cross-trigger efficiencies

1569 The efficiencies of the electron and muons for the cross-trigger with leading muon
 1570 used in the $e\mu$ channel are shown for data in 2016, 2017, and 2018 in Figures 5.6a and
 1571 5.6b [79]. These efficiencies were measured centrally using a Tag and Probe in events
 1572 with Z to dileptons with the same flavor and opposite charge, where the tags are an
 1573 isolated muon or electron, and the probe (offline) candidate is required to satisfy the
 1574 same lepton selection as that of the tag candidate, be matched within $\Delta R < 0.1$ with
 1575 a corresponding online trigger object, and also to pass the cross-trigger. The trigger
 1576 efficiency is then:

$$\text{Efficiency} = \frac{\text{Events passing lepton pair selections and probe passing trigger}}{\text{Events passing lepton pair selections}} \quad (5.5)$$



(a) Electron efficiency vs. p_T .



(b) Muon efficiency vs. η .

Figure 5.6: Efficiencies of the electron leg vs. p_T (left) and the muon log vs. η (right), for the HLT path with online thresholds of 12 GeV for the electron and 23 GeV for the muon, for the data-taking years 2016 (black), 2017 (red), and 2018 (green) [79].

1577 5.3.10 Electrons and muons faking τ_h : energy scales

1578 Energy scales for electrons misidentified as hadronic tau decays (e faking τ_h) are
 1579 provided by the Tau POG, and were measured in the $e\tau_h$ channel with the visible
 1580 invariant mass of the electron and hadronic tau system [69]. This energy scale is
 1581 applied for τ_h with $p_T > 20$ GeV regardless of which DeepTau vs. electron working
 1582 point was used. Values for 2018 are shown in Table 5.5.

Electrons faking τ_h energy scale factor in 2018	
Reconstructed decay mode of the fake τ_h	Central value and (up, down) shifts
0	1.01362 (+0.00474, -0.00904)
1	1.01945 (+0.01598, -0.01226)
10	0.96903 (+0.0125, -0.03404)
11	0.985 (+0.04309, -0.05499)

Table 5.5: Energy scales and up/down systematic uncertainties applied to electrons misidentified as hadronic taus for 2018, binned in decay mode of the fake τ_h [69].

1583 No nominal energy scale is applied for muons mis-reconstructed as τ_h , and the
 1584 uncertainty is treated as $\pm 1\%$ and uncorrelated in the reconstructed decay mode [69].

1585 **5.3.11 Electrons and muons faking τ_h : misidentification effi-**
 1586 **ciencies**

1587 Corrections on identification efficiencies are applied to genuine electrons and muons
 1588 misidentified as τ to account for differences in data and MC.

1589 The specific values depend on the vs. electron and vs. muon discriminator working
 1590 points used. For misidentified $\mu \rightarrow \tau_h$, the scale factors are split into different $|\eta|$
 1591 regions, determined by the CMS muon and tracker detector geometries, as shown in
 1592 Table 5.6 for 2018 [66].

Tau ID efficiency for DeepTau vs. muon WPs in 2018		
$ \eta $	Tight working point	VLoose working point
(0.0, 0.2)	0.767 ± 0.127	0.954 ± 0.069
(0.2, 0.6)	1.255 ± 0.258	1.009 ± 0.098
(0.6, 1.0)	0.902 ± 0.203	1.029 ± 0.075
(1.0, 1.45)	0.833 ± 0.415	0.928 ± 0.145
(1.45, 2.0)	4.436 ± 0.814	5.000 ± 0.377
(2.0, 2.53)	1.000 ± 0.000	1.000 ± 0.000

Table 5.6: Tau mis-identification efficiency for the DeepTau Tight and Very Loose (VLoose) working points vs. muons in 2018, binned in the muon $|\eta|$ [66].

1593 For misidentified $e \rightarrow \tau_h$, the scale factors are split into barrel and endcap regions,
 1594 dictated by the ECAL detector geometry, as shown in Table 5.7 for 2018.

Tau ID efficiency for DeepTau vs. electron WPs in 2018		
$ \eta $	Tight working point	VLoose working point
(0.0, 0.73)	1.47 ± 0.27	0.95 ± 0.07
(0.73, 1.509)	1.509 ± 0.0	1.00 ± 0.0
(1.509, 1.929)	1.929 ± 0.2	0.86 ± 0.1
(1.929, 2.683)	2.683 ± 0.9	2.68 ± 0.0

Table 5.7: Tau mis-identification efficiency for the DeepTau Tight and Very Loose (VLoose) working points vs. electrons in 2018, binned in the electron $|\eta|$ [66].

1595 5.3.12 Electron ID and tracking efficiency

1596 Scale factors are applied to MC to correct for differences between MC and data in
 1597 the performance of electron identification (ID) and tracking.

1598 Electron and photon identification, as discussed earlier, use variables with good
 1599 signal vs. background discrimination power such as lateral shower shape and ratio
 1600 of energy deposited in the HCAL to energy deposited in the ECAL at the position
 1601 of the electron. The cut-based electron identification efficiencies in data and ratio of
 1602 efficiencies in data to MC are shown in Fig. 5.7a for the multivariate analysis (MVA)
 1603 identification working point.

1604 The tracking efficiencies in data and the data/MC ratio are shown in Fig. 5.7b
 1605 for the Gaussian-sum filter (GSF) tracking [80].

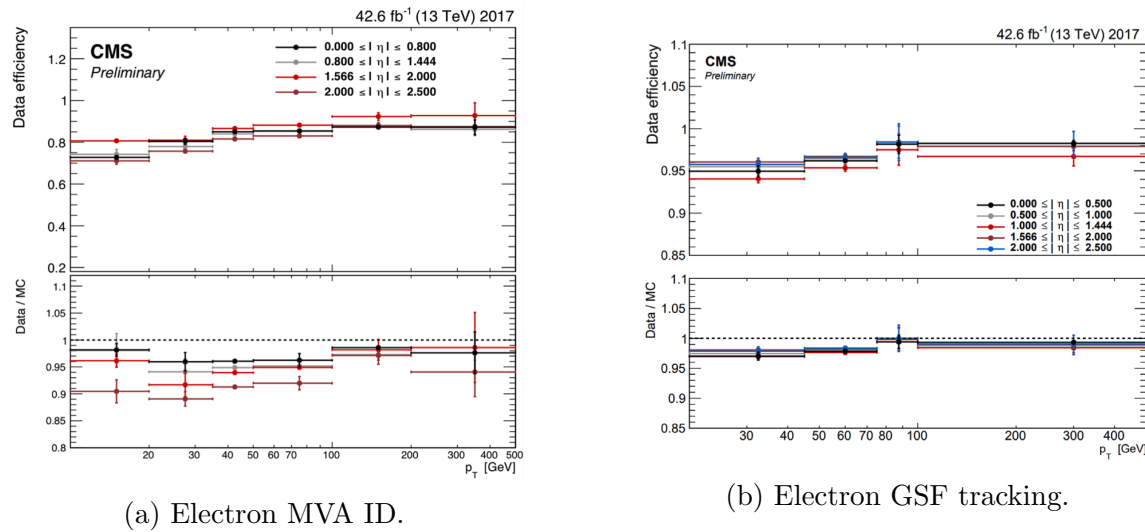


Figure 5.7: Efficiencies in data (*top panels*) and the ratio of efficiencies in data/MC (*bottom panels*), for the electron multivariate analysis (MVA) identification (*left*) and for the Gaussian-sum filter (GSF) tracking (*right*) [80]. Error bars represent statistical and systematic uncertainties.

1606 5.3.13 Muon ID, isolation, and tracking efficiencies

1607 Scale factors are applied to MC to correct for differences between MC and data in
 1608 the performance of muon identification, isolation, and tracking, as detailed below.

1609 The efficiencies for muon identification measured in 2015 data and MC simulation
 1610 are shown in Figures 5.8a and 5.8b for the loose ID and tight ID respectively [81]. The
 1611 loose ID is chosen such that efficiency exceeds 99% over the full η range, and the data
 1612 and simulation agree to within 1%. The tight ID is chosen such that efficiency varies
 1613 between 95% and 99% as a function of η , and the data and simulation agree to within
 1614 1-3%. The muon identification working point used in this analysis is the medium ID,
 1615 which has an efficiency of 98% for all η and an agreement within 1-2% [81].

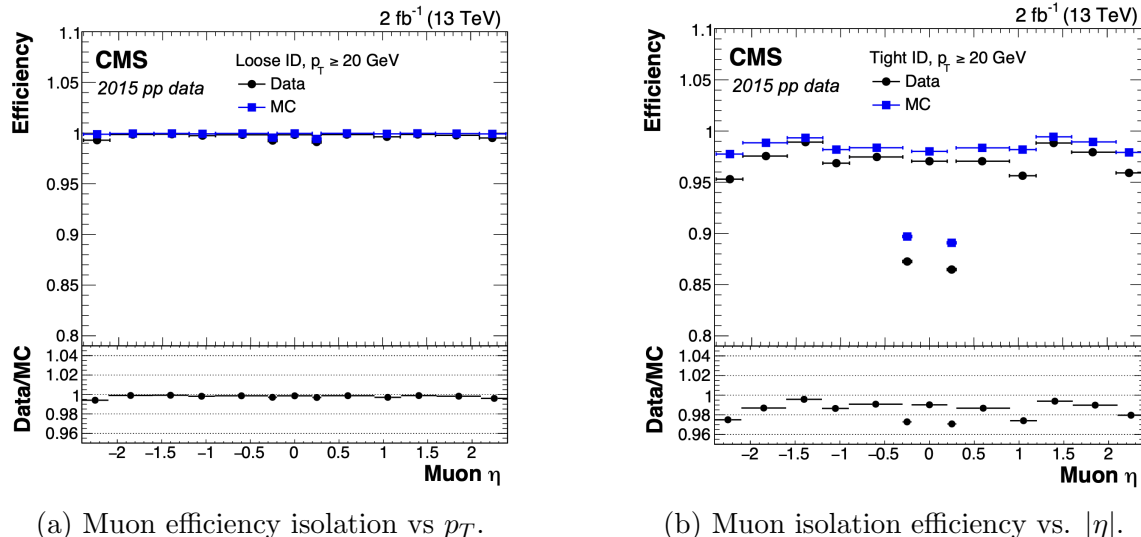
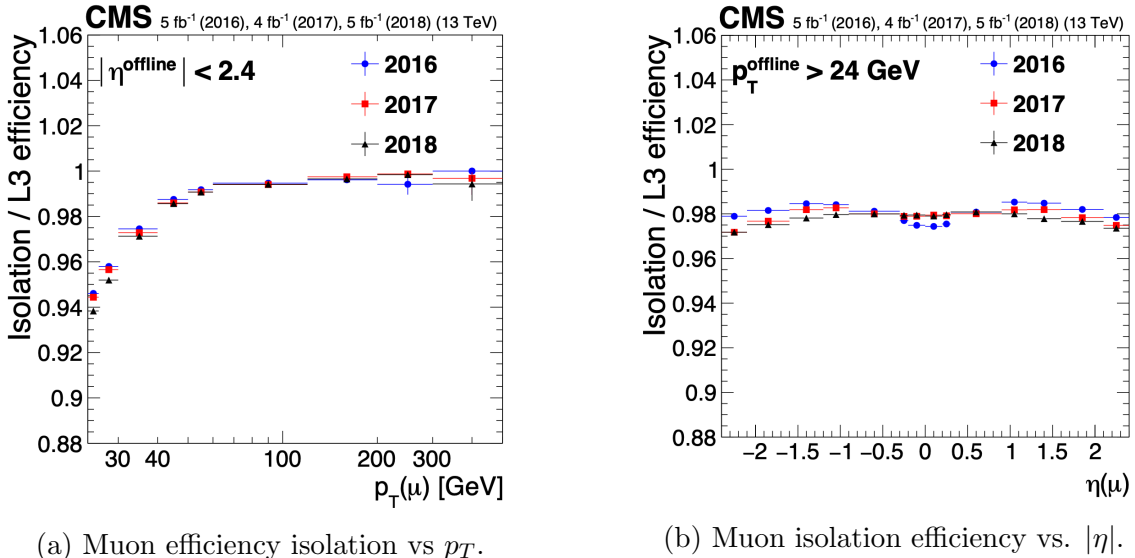


Figure 5.8: Muon identification efficiencies in 2015 data and MC as a function of the muon p_T for the loose ID (*left*) and tight ID (*right*) working points [81].

1616 The efficiencies in data for the muon isolation, as measured in Level-3 muons
 1617 (muons in one of the final stages of reconstruction in the HLT), as a function of the
 1618 muon p_T and $|\eta|$ are shown in Figures 5.9a and 5.9b [81]. The HLT muon reconstruc-
 1619 tion consists of two steps: Level-2 (L2), where the muon is reconstructed in the muon
 1620 subdetectors only, and Level-3 (L3) which is a global fit of tracker and muon hits (i.e.
 1621 the global muon reconstruction as described in Section 5.1.2) [82].

1622 The muon tracking efficiencies as a function of $|\eta|$ for standalone muons (i.e. tracks
 1623 from only the muon system, i.e. DT, CSC, and RPC, as discussed in Section 5.1.2),
 1624 is shown for data and simulated Drell-Yan samples in Fig. 5.10 [83].



(a) Muon efficiency isolation vs p_T .

(b) Muon isolation efficiency vs. $|\eta|$.

Figure 5.9: Muon isolation efficiencies in Run-2 data with respect to Level-3 muons (one of the final stages of HLT muon reconstruction) as a function of the muon p_T (*left*) and $|\eta|$ (*right*) [81].

5.3.14 Recoil corrections

In proton-proton collisions, W and Z bosons are predominantly produced through quark-antiquark annihilation. Higher-order processes can induce radiated quarks or gluons that recoil against the boson, imparting a non-zero transverse momentum to the boson [84]. Recoil corrections accounting for this effect are applied to samples with W+jets, Z+jets, and Higgs bosons [69]. The corrections are performed on the vectorial difference between the measured missing transverse momentum and the total transverse momentum of neutrinos originating from the decay of the W, Z, or Higgs boson. This vector is projected onto the axes parallel and orthogonal to the boson p_T . This vector, and the resulting correction to use, is measured in $Z \rightarrow \mu\mu$ events, since these events have leptonic recoil that do not contain neutrinos, allowing the 4-vector of the Z boson to be measured precisely. The corrections are binned in generator-level p_T of the parent boson and also the number of jets in the event.

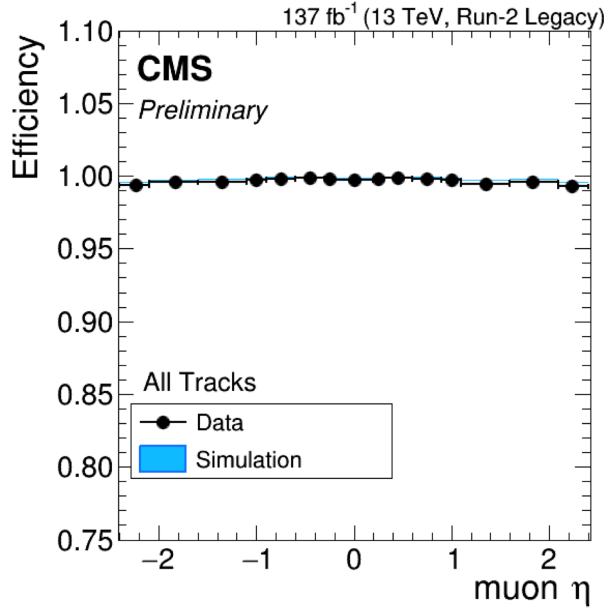


Figure 5.10: Muon tracking efficiencies as a function of $|\eta|$ for standalone muons in Run-2 data (*black*) and Drell-Yan MC simulation (*blue*) [83]. All Tracks refers to tracks which exploit the presence of muon candidates in the muon system to seed the track reconstruction in the inner tracker, in contrast to tracks that use tracker-only hits for seeding. Uncertainties shown are statistical.

5.3.15 Drell-Yan corrections

The Z boson transverse momentum distribution disagrees between leading-order (LO) simulations and data in a $Z \rightarrow \mu\mu$ control region with at least one b-tag jet [85]. Per-event weights derived by the 2016 data-only version of this analysis [85] are applied to $Z \rightarrow \tau\tau/\ell\ell$ events, as a function of the generator-level Z boson p_T to provide better matching of MC to data.

5.3.16 Pile-up reweighting

Reweighting is performed to rescale MC events to account for differences between MC and data, in the distribution of the pile-up (number of additional proton-proton interactions per bunch crossing). A tool for calculating the pile-up reweighting for the MC samples used is provided centrally by the Luminosity POG [86].

1649 **5.3.17 Pre-firing corrections**

1650 In 2016 and 2017 data-taking, a gradual timing shift of ECAL was not properly
1651 propagated to L1 trigger primitives (TPs), resulting in a large fraction of high η
1652 TPs being incorrectly associated with the previous bunch crossing. L1 trigger rules
1653 prevent two consecutive bunch crossings from firing, causing events to be rejected if
1654 significant ECAL energy was deposited in $2.0 < |\eta| < 3.0$. To account for this issue,
1655 MC simulations for 2016 and 2017 are corrected using an event-dependent weight.
1656 Embedded samples are not corrected [51].

1657 **5.3.18 Top p_T spectrum reweighing**

1658 In Run-1 and Run-2 it was observed that the p_T spectra of top quarks in $t\bar{t}$ data
1659 was significantly softer than those predicted by MC simulations [87]. Possible sources
1660 of this discrepancy are higher order QCD and/or electroweak corrections, and non-
1661 resonant production of $t\bar{t}$ -like final states. To account for this, corrections derived
1662 from Run-2 data by the Top Physics Analysis Group (PAG) are applied to the p_T
1663 of the top and anti-top quarks in MC simulations, computed as a function of their
1664 generator-level p_T [87].

1665 **5.3.19 B-tagging efficiency**

1666 In order to predict correct b-tagging discriminant distributions and event yields in
1667 data, the weight of selected MC events is reweighed according to recommendations by
1668 the BTV POG [88]. The reweighing depends on the jet p_T , η , and the b-tagging dis-
1669 criminant. In this method, there is no migration of events from one b-tag multiplicity
1670 bin to another.

1671 **5.3.20 Jet energy resolution and jet energy smearing**

1672 Calibration of jet energies, i.e. ensuring that the energy and momentum of the recon-
1673 structed jet matches that of the quark/gluon-initiated jet, is a challenging task due
1674 to time-dependent changes in the detector response and calibration and high pile-
1675 up [89] [90]. Jet calibration is done via jet energy corrections (JECs) applied to the
1676 p_T of jets in MC samples, accounting successively for the effects of pile-up, uniformity
1677 of the detector response, and residual data-simulation jet energy scale differences [91].
1678 Typical jet energy resolutions reported at $\sqrt{s} = 8$ TeV in the central rapidities are
1679 15-20% at 30 GeV and about 10% at 100 GeV [89]. Jet energy corrections are also
1680 propagated to the missing transverse energy.

1681 Measurements show that the jet energy resolution (JER) in data is worse than
1682 in simulation, and so the jets in MC need to be smeared to describe the data. JER
1683 corrections are applied after JEC on MC simulations, and adjust the width of the p_T
1684 distribution based on pile-up, jet size, and jet flavor [92]. Tools for applying JEC and
1685 JER are provided centrally by the JER Corrections group.

1686 Chapter 6

1687 Event selection

1688 This chapter describes how events in data and simulated samples are selected in the
1689 search for $h \rightarrow aa \rightarrow bb\tau\tau$. As described in the previous chapter, the tau lepton can
1690 decay to electrons (e), muons (μ), or hadronic states (τ_h). As a result, several different
1691 final states of the $\tau\tau$ system are possible, and are here referred to as “channels” since
1692 they are mutually exclusive. The three $\tau\tau$ final states studied in this analysis are
1693 muon and hadronic tau ($\mu\tau_h$), electron and hadronic tau ($e\tau_h$), and electron and
1694 muon ($e\mu$). The procedure for dividing events into these three channels begins with
1695 checking the High-Level Trigger paths passed by the events as detailed in Section 6.1.
1696 Events are further accepted or rejected based on criteria applied to the leptons in the
1697 event. These event selections are described for the $\mu\tau_h$ channel in Section 6.2, the $e\tau_h$
1698 channel in Section 6.3, and the $e\mu$ channel in Section 6.4.

1699 6.1 General procedure for all channels

1700 For the search for $h \rightarrow aa \rightarrow bb\tau\tau$, three final states of the $\tau\tau$ system are considered:
1701 $\mu\tau_h$, $e\tau_h$, and $e\mu$. The $\tau_h\tau_h$ final state is not considered because signal events in the
1702 $\tau_h\tau_h$ channel would typically produce hadronic taus with momenta below data-taking
1703 trigger thresholds.

1704 In all three final states, events are required to have at least one b-tag jet passing the
1705 medium working point of the DeepFlavour tagger, with $p_T > 20$ GeV, and $|\eta| < 2.4$.
1706 A second b-tag jet is not required because such a requirement would reduce signal
1707 acceptance by 80% compared to only requiring one b-tag jet.

1708 Events in MC samples are sorted into one of the three $\tau\tau$ channels if they pass the
1709 following trigger requirements and requirements on the offline reconstructed objects
1710 in the event, first checking the HLT paths for the $\mu\tau_h$ channel, then $e\tau_h$, and finally $e\mu$.
1711 The two leading leptons (e.g. muon and hadronic tau for the $\mu\tau_h$ channel) that were
1712 determined to have originated from the $\tau\tau$ decay, are called the $\tau\tau$ “legs”. For events
1713 in data and embedded samples, the HLT paths requirements for the corresponding
1714 channel are checked.

1715 After sorting events by HLT paths and identifying the leading tau legs in the offline
1716 reconstructed objects, the p_T of the offline objects is checked against the online trigger
1717 thresholds. Trigger matching is also performed, which checks the correspondence
1718 between each offline reconstructed object used in the analysis (e.g. a muon), and a
1719 trigger object in the HLT (e.g. a HLT muon). An offline object is considered to be
1720 matched, if it corresponds to a trigger object of the same object type, with $\Delta R < 0.5$.
1721 This matched trigger object is also required to pass the filter(s) of the HLT trigger.
1722 The trigger thresholds used for the $bb\mu\mu$ final state and the $bb\tau\tau$ final state (the focus
1723 of this work) are summarized in Tables 6.1.

1724 After checking the HLT paths and trigger objects in each channel, events are
1725 subject to further selection to ensure that they contain leptons and b-tag jet(s) of in-
1726 terest. These requirements are summarized in Table 6.2, and detailed in the following
1727 sections.

Year	Single/dilepton trigger p_T	$bb\mu\mu$	$bb\tau\tau$					
			$e\mu$		$e\tau_h$		$\mu\tau_h$	
		μ	e	μ	e	τ_h	μ	τ_h
2016	Single lepton	24	–	–	25	–	22	–
	p_T -leading lepton	17	23	23	–	–	–	20
	p_T -subleading lepton	8	12	8	–	–	19	–
2017	Single lepton	24	–	–	27, 32	–	24, 27	–
	p_T -leading lepton	17	23	23	–	30	–	27
	p_T -subleading lepton	8	12	8	24	–	20	–
2018	Single lepton	24	–	–	32, 35	–	24, 27	–
	p_T -leading lepton	17	23	23	–	30	–	27
	p_T subleading lepton	8	12	8	24	–	20	–

Table 6.1: Trigger thresholds used for the leptons in the $bb\mu\mu$ analysis and the $bb\tau\tau$ analysis (the focus of this work). The thresholds for the three $bb\tau\tau$ channels ($e\mu$, $e\tau_h$, and $\mu\tau_h$) are listed separately, with some channels and years taking the logical OR of two triggers with different thresholds.

6.2 Event selection in the $\mu\tau_h$ channel

In all three years, a single muon trigger is used if the muon has sufficiently high p_T , otherwise a dilepton $\mu\tau_h$ cross-trigger is used (Tables 6.3, 6.4, and 6.5). For data taken in 2017-2018 (2016), the logical OR of the single muon triggers with online p_T thresholds 24 and 27 (23) GeV is used, with the corresponding offline muon required to have with p_T 1 GeV above the online threshold. For data taken in 2017-2018 (2016), a dilepton $\mu + \tau_h$ cross-trigger with p_T thresholds of 20 (19) and 27 (20) GeV for the muon and tau respectively, is used. The τ_h is required to have $|\eta| < 2.3$ if the single trigger is fired, $|\eta| < 2.1$.

The muon and τ_h are required to have opposite charge and be separated by $\Delta R > 0.4$. The muon is required to have $|\eta| < 2.4$, and the τ_h is required to have $|\eta| < 2.3$ unless a cross-trigger is required, in which case we require $|\eta| < 2.1$ as discussed above.

The muon is required to pass the medium identification (ID) working point [93], which is defined by the Muon POG as a loose muon (i.e. a Particle Flow muon that is either a global or a tracker muon - see Section 5.1.2) with additional requirements

All years (2016, 2017, 2018) and eras				
Kinematic variable	$bb\mu\mu$		$bb\tau\tau$	
	μ	$e\mu$	$e\tau_h$	$\mu\tau_h$
ΔR between leptons	>0.4	>0.3	>0.4	>0.4
$ \eta $ of electron	-	<2.4	<2.1	-
$ \eta $ of muon	<2.4	<2.4	-	<2.1
$ \eta $ of hadronic tau	-	-	<2.3/< 2.1	<2.3/< 2.1
Relative isolation of electron	-	<0.10	-	<0.15
Relative isolation of muon	<0.25	<0.15	-	<0.15
Leading b-tag jet p_T	>15 GeV		>20 GeV	
Leading b-tag jet $ \eta $	<2.4		<2.4	
Leading b-tag jet WP	Tight		Medium	
Sub-leading b-tag jet p_T	>15 GeV		-	
Sub-leading b-tag jet $ \eta $	<2.4		-	
Sub-leading b-tag jet WP	Loose		-	
ΔR between jet(s) and leptons	>0.4		>0.5	

Table 6.2: Summary of requirements applied to the leptons in the $bb\mu\mu$ analysis and the $bb\tau\tau$ analysis (the focus of this work). $\Delta R = \sqrt{(\Delta\eta)^2 + (\Delta\phi)^2}$ is a measure of spatial separation. Relative isolation is defined in Eqn. 5.2 and Section 5.1.2. The b-tag jets are required to pass the listed DeepFlavour working points (WP), which are described in Section 5.1.5. In the $bb\tau\tau$ analysis, the required $|\eta|$ of the hadronic taus are listed for the single and cross triggers respectively. The $bb\mu\mu$ analysis requires two b-tag jets in all events, while the $bb\tau\tau$ analysis only requires one.

1744 on track quality and muon quality. This identification criteria is designed to be
1745 highly efficiently for prompt muons and for muons from heavy quark decays. In
1746 addition to the ID, for prompt muons it is recommended to apply cuts on the impact
1747 parameter [93]: we apply $|\Delta(z)| < 0.2$ and $|\Delta(xy)| < 0.045$.

1748 In addition, a cut is applied on the muon relative isolation (defined in Section
1749 5.1.2), to be less than 0.15 in a cone size of $\Delta R = 0.4$, which corresponds to the
1750 Tight Particle Flow isolation requirement [93].

1751 The τ_h is required to pass a cut on its impact parameter of $|\Delta(z)| < 0.2$. The τ_h
1752 is also required to pass the VLoose (Very Loose) DeepTau working point vs. elec-
1753 tron, the Tight DeepTau working point vs. muons, and the VVVLoose and Medium
1754 DeepTau working point vs. jets. Events with taus reconstructed in two of the decay
1755 modes (labeled 5 and 6) are rejected, since these decay modes are meant to recover
1756 3-prong taus, but are only recommended for use in analyses where the benefits in
1757 final significance outweigh the resulting increase in background [66].

1758 For the estimation of the background from jets faking τ_h , which is described in Sec-
1759 tion 7.7, anti-isolated events are selected, by requiring events to pass all the selections
1760 described above, except failing the Medium DeepTau working point vs. jets.

1761 6.3 Event selection in the $e\tau_h$ channel

1762 The HLT trigger paths for the $e\tau_h$ channel are summarized in Tables 6.3, 6.4, and
1763 6.5. Similarly to the $\mu\tau_h$ channel, a single electron trigger is used if the electron has
1764 sufficiently high p_T in 2018 and 2017. For data taken in 2018 (2017), the OR of the
1765 single electron triggers with online p_T thresholds at 32 and 35 (27 and 32) GeV are
1766 used, with the corresponding offline electrons required to have p_T greater than 33
1767 (28) GeV. A $e + \tau_h$ cross-trigger is used for electrons with lower offline p_T between
1768 25 and 33 GeV (25 and 28 GeV). For the 2016 dataset, there is no cross trigger but

1769 only a single electron trigger with online p_T threshold at 25 GeV, which is used if the
1770 offline electron has p_T greater than 26 GeV.

1771 The electron and τ_h are required to have opposite charge and be separated by
1772 $\Delta R > 0.4$. The electron is required to be within $|\eta| < 2.3$ when no cross trigger is
1773 used, and $|\eta| < 2.1$ when the cross trigger is fired. The τ_h is required to have $|\eta| < 2.3$
1774 if no cross trigger is fired, and have $|\eta| < 2.1$ if the cross trigger is fired.

1775 The electron is required to have a relative isolation (same definition as in Section
1776 5.1.2) of less than 0.1 in a cone size of $\Delta R = 0.3$, which is the standard recommended
1777 cone size giving minimal pile-up dependence and reduced probability of other objects
1778 overlapping with the cone. The isolation quantity used includes an “effective area”
1779 (EA) correction to remove the effect of pile-up in the barrel and endcap parts of the
1780 detector [94].

1781 The electron is also required to pass cuts on its impact parameter of $|\Delta(z)| < 0.2$
1782 and $|\Delta(xy)| < 0.045$. It is also required to pass the non-isolated MVA working point
1783 corresponding to 90% efficiency. The electron’s number of missing hits, which are
1784 gaps in its trajectory through the inner tracker [94], must be less than or equal to
1785 1. The electron must pass a conversion veto, which rejects electrons coming from
1786 photon conversions in the tracker, which should instead be reconstructed as part of
1787 the photon [94].

1788 The impact parameter cut for the τ_h is $|\Delta(z)| < 0.2$. In contrast to the $\mu\tau_h$ event
1789 selection, the vs. electron and vs. muon DeepTau working points are flipped, to
1790 reject muons faking the τ_h leg. The τ_h is required to pass the Tight DeepTau working
1791 point vs. electrons, the VLoose DeepTau working point vs. muons, and the Medium
1792 DeepTau working point vs. jets.

1793 As in the $\mu\tau_h$ channel, for the estimation of the background from jets faking τ_h ,
1794 which is described in Section 7.7, anti-isolated events are selected, by requiring events
1795 to pass all the selections described above, except failing the Medium DeepTau working

1796 point vs. jets.

1797 6.4 Event selection in the $e\mu$ channel

1798 The HLT trigger paths for the $e\mu$ channel are summarized in Tables 6.3, 6.4, and
1799 6.5. Events are selected with the logical OR of two $e + \mu$ cross triggers, where either
1800 the electron or muon can have larger p_T : (1) leading electron, where the electron has
1801 online $p_T > 23$ GeV and muon has online $p_T > 8$ GeV, or (2) leading muon, where
1802 electron has online $p_T > 12$ GeV and muon has online $p_T > 23$ GeV.

1803 The leading and sub-leading leptons are required to have an offline p_T greater
1804 than 1 GeV above the online threshold (i.e. $p_T > 24$ GeV). If the sub-leading lepton
1805 is the electron, the offline p_T threshold is 1 GeV above the online threshold ($p_T > 13$
1806 GeV), but if it is a muon, the offline p_T threshold is required to be at least 5 GeV
1807 greater than the online threshold (i.e. $p_T > 13$ GeV). This is because of poor data
1808 and simulation agreement for low- p_T muons with p_T between 9 GeV and 13 GeV, and
1809 the higher probability of mis-identifying jets as muons at lower p_T . With no effect on
1810 the expected limits, the offline p_T threshold for muons is raised to 13 GeV instead of
1811 9 GeV, even though it may lead to loss in signal acceptance. Both the electron and
1812 muon are required to have $|\eta| < 2.4$.

1813 The electron and muon are required to have opposite charge and be separated
1814 by $\Delta R > 0.3$ (note the decreased separation requirement compared to the other
1815 two channels). The electron is required to pass the non-isolated MVA identification
1816 working point corresponding to 90% efficiency, and to have a relative isolation less
1817 than 0.1 for a cone size of $\Delta R = 0.3$ with the EA pile-up subtraction correction.
1818 The electron must have one or fewer missing hits and pass the conversion veto (both
1819 described previously in Section 6.3).

1820 The muon is required to pass the medium identification working point (described

earlier in 6.2), and to have a relative isolation less than 0.15 for a cone size of $\Delta R = 0.4$. The muon impact parameter is required to have $|\Delta(z)| > 0.2$ and $|\Delta(xy)| < 0.045$.

For the QCD multijet background estimation described in Section 7.8, the same-sign region is selected by requiring all the above selections, except the legs are required to have the same electric charge rather than opposite.

2016 $\mu\tau_h$ trigger paths	
Notes	HLT Path
	HLT_IsoMu22_v
	HLT_IsoMu22_eta2p1_v
	HLT_IsoTkMu22_v
	HLT_IsoTkMu22_eta2p1_v
	HLT_IsoMu19_eta2p1_LooseIsoPFTau20_v
	HLT_IsoMu19_eta2p1_LooseIsoPFTau20_SingleL1_v
2016 $e\tau_h$ trigger paths	
Notes	HLT Path
	HLT_Ele25_eta2p1_WPTight_Gsf_v
2016 $e\mu$ trigger paths	
Notes	HLT Path
runs B-F and MC	HLT_Mu23_TrkIsoVVL_Ele12_CaloIdL_TrackIdL_IsoVL_v
runs B-F and MC	HLT_Mu8_TrkIsoVVL_Ele23_CaloIdL_TrackIdL_IsoVL_v
runs G-H	HLT_Mu23_TrkIsoVVL_Ele12_CaloIdL_TrackIdL_IsoVL_DZ_v
runs G-H	HLT_Mu8_TrkIsoVVL_Ele23_CaloIdL_TrackIdL_IsoVL_DZ_v

Table 6.3: High-Level Trigger (HLT) paths used to select data and simulation events in 2016 for the three $\tau\tau$ channels.

6.5 Extra lepton vetoes in all channels

Events containing a third lepton (electron or muon) that is neither of the leading $\tau\tau$ legs are rejected, and events with di-muons and di-electrons are vetoed, with criteria taken from the Standard Model $H \rightarrow \tau\tau$ working group [69].

The event is vetoed if a third electron is found with the following properties: $p_T > 10$ GeV, $|\eta| < 2.5$, impact parameter $|\Delta(z)| < 0.2$ and $|\Delta(xy)| < 0.045$, passing non-isolation MVA identification with 90% efficiency, conversion veto, ≤ 1 missing

2017 $\mu\tau_h$ trigger paths	
Notes	HLT Path
	HLT_IsoMu24_v
	HLT_IsoMu27_v
	HLT_IsoMu20_eta2p1_LooseChargedIso_PFTau27_eta2p1_CrossL1_v
2017 $e\tau_h$ trigger paths	
Notes	HLT Path
	HLT_Ele32_WPTight_Gsf_v
	HLT_Ele35_WPTight_Gsf_v
	HLT_Ele24_eta2p1_WPTight_Gsf_Loose_ChargedIsoPFTau30_eta2p1_CrossL1_v
2017 $e\mu$ trigger paths	
Notes	HLT Path
	HLT_Mu23_TrkIsoVVL_Ele12_CaloIdL_TrackIdL_IsoVL_DZ_v
	HLT_Mu8_TrkIsoVVL_Ele23_CaloIdL_TrackIdL_IsoVL_DZ_v

Table 6.4: High-Level Trigger (HLT) paths used to select data and simulation events in 2017 for the three $\tau\tau$ channels.

1833 hits, and relative isolation < 0.3 with cone size $\Delta R = 0.3$. The event is also vetoed if
 1834 a third muon is found with the following properties: $p_T > 10$ GeV, $|\eta| < 2.4$, impact
 1835 parameter $|\Delta(z)| < 0.2$ and $|\Delta(xy)| < 0.045$, medium ID, and isolation < 0.3 with
 1836 cone size $\Delta R = 0.4$.

1837 A di-muon veto is applied, which rejects events containing a pair of muons with
 1838 opposite charge and separation of $\Delta R > 0.15$, that both pass the following selections:
 1839 $p_T > 15$ GeV, $|\eta| < 2.4$, flag for global muons, flag for tracker muon, flag for Particle
 1840 Flow muon, $|\Delta(z)| < 0.2$, $|\Delta(xy)| < 0.045$, and isolation < 0.3 with cone size $\Delta R =$
 1841 0.4. A similar di-electron veto is applied to reject events containing a pair of electrons
 1842 with opposite charge and separation of $\Delta R > 0.15$, that both pass the following
 1843 selections: $p_T > 15$ GeV, $|\eta| < 2.5$, a dedicated electron ID (cut-based) for vetoing
 1844 third leptons, $|\Delta(z)| < 0.2$, $|\Delta(xy)| < 0.045$, with pile-up corrected relative isolation
 1845 < 0.3 with cone size $\Delta R = 0.3$.

1846 These vetoes on extra leptons also ensure orthogonality of events to analyses such
 1847 as the $bb\mu\mu$ final state, whose results are combined with this $bb\tau\tau$ final state as
 1848 described in Section 10.2.

2018 $\mu\tau_h$ trigger paths	
Notes	HLT Path
	HLT_IsoMu24_v
	HLT_IsoMu27_v
only data run < 317509	HLT_IsoMu20_eta2p1_ (contd.)
	LooseChargedIsoPFTauHPS27_eta2p1_CrossL1_v
MC and data run \geq 317509	HLT_IsoMu20_eta2p1_ (contd.)
	LooseChargedIsoPFTauHPS27_eta2p1_TightID_CrossL1_v
2018 $e\tau_h$ trigger paths	
Notes	HLT Path
	HLT_Ele32_WPTight_Gsf_v
	HLT_Ele35_WPTight_Gsf_v
only data run < 317509	HLT_Ele24_eta2p1_WPTight_Gsf_ (contd.)
	LooseChargedIsoPFTauHPS30_eta2p1_CrossL1_v
MC and data run \geq 317509	HLT_Ele24_eta2p1_WPTight_Gsf_ (contd.)
	LooseChargedIsoPFTauHPS30_eta2p1_TightID_CrossL1_v
2018 $e\mu$ trigger paths	
Notes	HLT Path
	HLT_Mu23_TrkIsoVVL_Ele12_CaloIdL_TrackIdL_IsoVL_DZ_v
	HLT_Mu8_TrkIsoVVL_Ele23_CaloIdL_TrackIdL_IsoVL_DZ_v

Table 6.5: High-Level Trigger (HLT) paths used to select data and simulation events in 2018 for the three $\tau\tau$ channels. In 2018 a HLT trigger path using the hadron plus strips (HPS) tau reconstruction algorithm became available.

1849 **Chapter 7**

1850 **Background estimation**

1851 This section describes methods used to estimate sources of background from Standard
1852 Model processes in the search for $h \rightarrow aa \rightarrow bb\tau\tau$. Similar background estimation
1853 methods are being used for the $h \rightarrow a_1a_2$ analysis. The background contributions
1854 directly taken from MC are described in Sections 7.1 to 7.6. Section 7.7 describes
1855 the data-driven method for estimating backgrounds from jets faking hadronic tau
1856 decays ($\text{jet} \rightarrow \tau_h$), which is used in the $\mu\tau_h$ and $e\tau_h$ channels. Section 7.8 describes
1857 the data-driven method for estimating background from quantum chromodynamic
1858 (QCD) processes in the $e\mu$ channel.

1859 **7.1 Z+jets**

1860 A major source of background for $\tau\tau$ analyses is the Drell-Yan (DY) process (Z+jets).
1861 The Z boson decays to $\tau\tau/\mu\mu/ee$ with equal probability of 3.4% each, with the domi-
1862 nant decay modes being to hadrons (around 70%) and neutrinos (invisible) (20%) [26].
1863 The Drell-Yan contribution with genuine taus, $Z \rightarrow \tau\tau$, is estimated using embed-
1864 ded samples, described in Section 4.3. To avoid double-counting between embedded
1865 and MC samples, in all MC samples, events with legs that originated from genuine τ
1866 are discarded.

1867 The other decays of the Z , $Z \rightarrow ee$ and $Z \rightarrow \mu\mu$, are estimated from MC simulation,
1868 and are hereafter referred to as simply the Drell-Yan background. These MC samples
1869 are generated to leading order (LO) with different numbers of jets (jet multiplicity) in
1870 the matrix element: $Z+1$ jet, $Z+2$ jets, $Z+3$ jets, $Z+4$ jets, and inclusive $Z+jets$. The
1871 cross-sections of the samples with ≥ 1 jets are normalized to next-to-NLO (NNLO)
1872 in QCD.

1873 For the inclusive Drell-Yan sample, two samples are used with different thresholds
1874 for the di-lepton invariant mass ($m_{\ell\ell}$) at the generator level: one with $m_{\ell\ell} > 50$ GeV
1875 and the other with $10 < m_{\ell\ell} < 50$.

1876 **7.2 W+jets**

1877 The dominant W boson decay modes are to hadrons (67.4%), $e + \nu_e$ (10.7%), $\mu + \nu_\mu$
1878 (10.6%), and $\tau + \nu_\tau$ (11.4%) [26]. The $W+jets$ background is estimated from MC
1879 simulation. Similarly to the $Z+jets$, the $W+jets$ samples are generated with different
1880 jet multiplicities in the matrix element. LO samples are used for greater statistics
1881 and are normalized to NNLO cross sections.

1882 **7.3 $t\bar{t} + jets$**

1883 In hadron collisions, top quarks are produced singly with the weak interaction, or in
1884 pairs via the strong interaction, with interference between these leading-order pro-
1885 cesses possible in higher orders of the perturbation theory. The top quark is the
1886 heaviest fermion in the Standard Model and has a short lifetime ($\sim 10^{-25}$ s), decay-
1887 ing without hadronization into a bottom quark and a W boson [26], with the decay
1888 modes of the W boson as listed in the previous section. With two top quarks, the
1889 final states of the two resulting W bosons can be described as fully leptonic, semilep-
1890 tonic, and fully hadronic. These three final states are modeled separately with MC

1891 simulation in 2018 and 2017, while for 2016 the sample used is inclusive.

1892 7.4 Single top

1893 There are three main production modes of the single top in pp collisions [95]: the
1894 exchange of a virtual W boson (t channel), the production and decay of a virtual W
1895 boson (s channel), and the associated production of a top quark and W boson (tW ,
1896 or W-associated) channel. As the s channel process is rare and only 3% of the total
1897 production, the dominant production mode of the t -channel and the tW production
1898 are considered and modeled with MC.

1899 7.5 Diboson

1900 In pp collisions, the production of dibosons (pairs of electroweak gauge bosons, i.e.
1901 WW, WZ, and ZZ) is dominated by quark-antiquark annihilation, with a small con-
1902 tribution from gluon-gluon interaction [96]. MC is used to model the pair production
1903 and decays of VV to $2\ell 2\nu$, WZ to $2q 2\ell$ and $3\ell\nu$, and ZZ to 4ℓ and $2q 2\ell$ (q being
1904 quarks and ℓ being leptons).

1905 7.6 Standard Model Higgs

1906 MC is used to simulate backgrounds from major production modes of the Standard
1907 Model 125 GeV Higgs boson: gluon-gluon fusion (ggH), vector boson fusion (VBF),
1908 associated production with a W or Z (WH, ZH), and associated production with a
1909 top pair (ttH) (see Fig. 7.1 for leading-order diagrams). For these production modes,
1910 samples with the Higgs decaying to $\tau\tau$ or to WW are used. Samples made with
1911 higher-order diagrams for WH and ZH that include the production of a jet, with the
1912 Higgs decaying to WW, are also used.

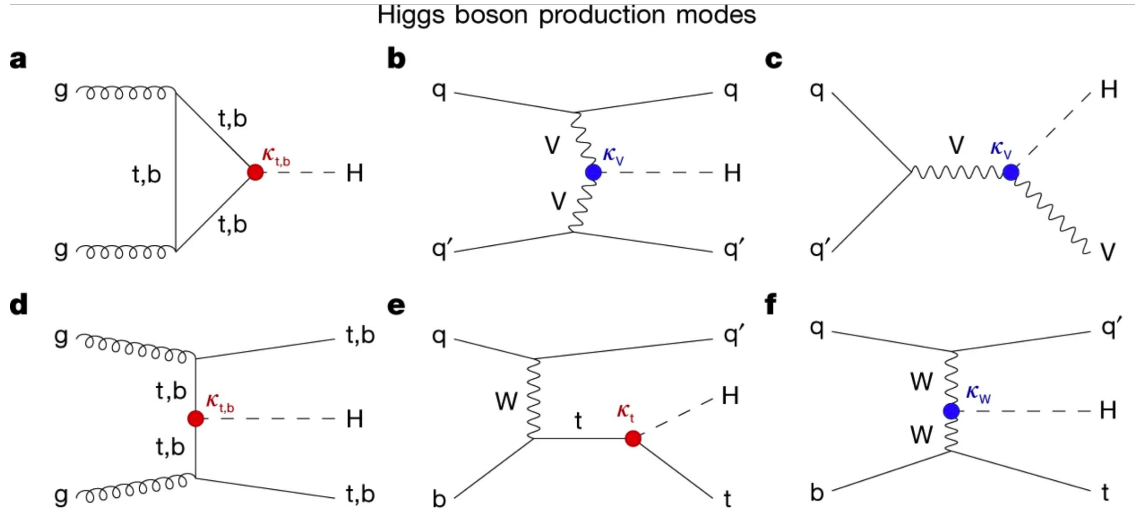


Figure 7.1: Leading-order Feynman diagrams of Higgs production from [97], in ggH (a) and vector boson fusion (VBF; b), associated production with a W or Z (V) boson (VH; c), associated production with a top or bottom quark pair (ttH or bbH); d, and associated production with a single top quark (tH; e, f).

1913 7.7 Jet faking τ_h

1914 Events with a jet mis-reconstructed as the hadronic tau leg τ_h are a major source of
1915 background in the $\mu\tau_h$ and $e\tau_h$ channels. The main processes contributing to jet $\rightarrow \tau_h$
1916 events are QCD multijet, W+jets, and $t\bar{t}$ production. These events are estimated
1917 using a data-driven method adapted from past analyses [51] [85]. This background
1918 includes contributions from W+jets, QCD multijets, and $t\bar{t}$ +jets. To estimate this
1919 background, a sideband region is constructed, where events are required to pass all
1920 baseline $\mu\tau_h/e\tau_h$ selection criteria, but fail the τ_h isolation criteria. The events in
1921 this sideband region are reweighed with a factor $f/(1-f)$, where f is the probability
1922 for a jet to be misidentified as a τ_h . The jet $\rightarrow \tau_h$ background is the anti-isolated,
1923 reweighed MC and embedded events subtracted from the anti-isolated, reweighted
1924 data events.

1925 The fake factor is measured in $Z \rightarrow \mu\mu + \text{jets}$ events in data in the $\mu\mu\tau_h$ final
1926 state, as any reconstructed τ_h in these events must originate from a jet. The two
1927 muons are required to be isolated (< 0.15), have opposite electric charge, and have

1928 an invariant mass between 76 and 106 GeV (close to the Z mass). These events are
1929 selected with a double muon trigger, with the leading muon having offline $p_T > 20$
1930 GeV and the subleading muon $p_T > 10$ GeV. Simulated diboson (ZZ and WZ) events
1931 are subtracted to avoid contamination from events with real τ_h . The denominator of
1932 the fake rate corresponds to fake taus passing the VVVLoose working point of the
1933 discriminator vs. jets, while the numerator corresponds to those passing the Medium
1934 working point, i.e. $f = N_{\text{jet passing tight}} / N_{\text{jet passing loose}}$.

1935 f is measured as a function of the τ_h transverse momentum and is 8% - 10% in
1936 each of the data-taking years. f is derived separately for the $\mu\tau_h$ and $e\tau_h$ channels
1937 because the channels use different anti-lepton identification working points.

1938 7.8 QCD multijet background

1939 In the $e\mu$ channel, events with jets faking electrons or muons originating from QCD
1940 multijet, is estimated from data events with the same baseline selection as in the
1941 signal region, except with same-signed (SS) charged $e + \mu$, ensuring orthogonality
1942 with the signal region which requires opposite-sign (OS) $e\mu$ pairs. All same-sign MC
1943 events (both events with real and fake $e + \mu$) are subtracted from same-sign data
1944 events to remove contamination from other backgrounds. i.e. $\text{QCD}_{\text{SS}} = \text{Data}_{\text{SS}} -$
1945 MC_{SS} .

1946 Three scale factors are applied to the QCD_{SS} events to compute the QCD multijet
1947 background [85] [40]:

- 1948 • *OS-to-SS scale factor*: This scales the SS QCD to the OS region, and is mea-
1949 sured from an orthogonal region with an isolated electron and an anti-isolated
1950 muon. Only the muon is chosen to be anti-isolated because this scale factor was
1951 observed to depend more strongly on electron isolation than that of the muon.
1952 This scale factor is treated as a function of the ΔR separation of the trajectories

1953 of the electron and muon, and is measured separately for events with 0 jets, 1,
1954 jet, and greater than 1 jet.

- 1955 • *2D closure correction for the lepton p_T :* This factor accounts for subleading
1956 dependencies of the first scale factor on the p_T of the two leptons. A 2D weight
1957 is derived in a similar fashion, as a ratio of QCD_{OS} events to QCD_{SS} events,
1958 but parameterized by both electron and muon p_T , where the SS events have the
1959 previous scale factor applied.
- 1960 • *Isolation correction for the muon:* The third and final factor is an isolation
1961 correction, which is a bias correction to account for the fact that the fake
1962 factor was determined for less-isolated muons. This factor is obtained as the
1963 ratio of the OS-to-SS scale factors measured in two other control regions: (1)
1964 events where the electron is anti-isolated ($0.15 < \text{iso} < 0.5$) and the muon is
1965 isolated, and (2) events where both leptons are anti-isolated.

¹⁹⁶⁶ Chapter 8

¹⁹⁶⁷ Systematic uncertainties

¹⁹⁶⁸ The handling of systematic uncertainties is separated into normalization uncertainties
¹⁹⁶⁹ (those that affect the total yield of a variables' distribution) and shape uncertainties
¹⁹⁷⁰ (those that shift the distribution of events). Normalization uncertainties are expressed
¹⁹⁷¹ as multiplicative factors, while shape uncertainties are represented as up and down
¹⁹⁷² shifts of a variable's distribution.

¹⁹⁷³ Up/down shifts of shape uncertainties can change the number of background
¹⁹⁷⁴ events in a distribution. For instance, hadronic taus receive corrections from the
¹⁹⁷⁵ nominal tau energy scale, with the nominal, up, and down energy scales provided
¹⁹⁷⁶ centrally by CMS. For the $\mu\tau_h$ channel, an event could have a τ_h with p_T just below
¹⁹⁷⁷ the offline threshold of 20 GeV (for instance, 19.5 GeV), so in the nominal distribution
¹⁹⁷⁸ of $m_{\tau\tau}$ (or any other variable for this channel), the event is excluded. However, when
¹⁹⁷⁹ we build our distributions with the tau energy scale “up” shift, the energy of this τ_h
¹⁹⁸⁰ may be scaled up to, say, 20.5 GeV, and now the event passes the offline p_T threshold
¹⁹⁸¹ for the single muon trigger, leading to the event's inclusion in the distributions made
¹⁹⁸² with the tau energy scale “up” shift.

¹⁹⁸³ In evaluating the up and down shifts of a specific source of uncertainty, all other
¹⁹⁸⁴ corrections and scale factors are held at their nominal values, and the full chain of

1985 object and event selection and event categorization is performed to obtain the observ-
1986 able distributions. Any “downstream” variables that depend on the shifted variable,
1987 e.g. the invariant di-tau mass $m_{\tau\tau}$, must be computed for the nominal case, and then
1988 re-computed separately for each up and down shift of the tau legs’ energy scale. The
1989 objective of this process is to quantify the effect of a single source of uncertainty on
1990 the resulting observable distributions. Each scale factor and correction described in
1991 Section 5.3 has an associated uncertainty. The binning of the uncertainties follows
1992 that of the nominal scale factor value.

1993 Sections 8.1 to 8.5 describe uncertainties associated with physics objects, and
1994 Sections 8.6 and 8.7 describe uncertainties associated with sample-level effects. The
1995 pulls and impacts for the top sixty most important systematics are shown in Section
1996 8.8.

1997 **8.1 Uncertainties in the lepton energy scales**

1998 The uncertainties in the tau energy scales [66] are binned by the tau decay mode and
1999 are taken as shape uncertainties treated as uncorrelated across the tau decay modes
2000 and years. Same as with the application of the nominal scale factor, when applying
2001 the up or down shifts, the missing transverse energy (p_T^{miss}) of the event is adjusted
2002 so that the 4-vector sum of the tau p_T^{miss} is unchanged.

2003 The uncertainties in the muon energy scale [67] are 0.4% for $|\eta| < 1.2$, 0.9% for
2004 $1.2 < |\eta| < 2.1$, and 2.7% for $2.1 < |\eta| < 2.4$, and are treated as shape uncertainties,
2005 fully uncorrelated between embedded and MC samples.

2006 The uncertainties in the electron energy scale [70] in MC are binned in the electron
2007 $|\eta|$ and p_T , and are shown in Fig. 5.2. The uncertainties range from 0.5% to 2.2% in
2008 the barrel, and 0.3% to 4.1% in the endcap, across the p_T range. The uncertainties
2009 for the embedded sample are binned only in $|\eta|$ and are on the order of 0.5% and

2010 1.25% for the barrel and endcap [74].

2011 There are also uncertainties in the energy scales for electrons and muons misiden-
2012 tified as τ_h . The uncertainty for muons misidentified as τ_h is 1% [66]. For electrons
2013 misidentified as τ_h , the uncertainty is binned in barrel/endcap η and by 1-prong and
2014 1-prong + π_0 decays. The probability for e/μ faking a 3-prong decay mode is much
2015 lower.

2016 8.2 Uncertainties from other lepton corrections

2017 Uncertainties associated with the τ_h identification efficiencies are treated as shapes,
2018 uncorrelated across the seven p_T bins and years. The shape uncertainties in the
2019 embedded samples are taken as 50% correlated with those of the MC samples.

2020 The uncertainties on electron and muon identification efficiencies are taken as
2021 normalization uncertainties of 2% each, with a 50% correlation between embedded
2022 and MC samples.

2023 In the $e\tau_h$ channel, there is an additional uncertainty for the vs. jet discrimination
2024 efficiency [66], because the analysis uses a looser anti-lepton working point (VLoose
2025 WP) than the working points used in the measurement of the efficiency (namely,
2026 VLoose WP vs e, and Tight WP vs mu). For nominal $\tau_h p_T < 100$ GeV, an additional
2027 uncertainty of 3% (5%) is used in MC (embedded), and for high p_T an uncertainty of
2028 15% is used for both.

2029 The uncertainties in trigger efficiencies are taken as shapes [66]. In the $e\tau_h$ and $\mu\tau_h$
2030 channels, there are uncertainties for the single and cross lepton triggers, and in the
2031 $e\mu$ channel there is one uncertainty each for the two $e + \mu$ triggers, and one combined
2032 uncertainty since their trigger phase spaces are not mutually exclusive.

2033 **8.3 Uncertainties from jet energy scale and reso-**
2034 **lution**

2035 The jet energy scale uncertainties are taken as shape uncertainties: there are eleven
2036 in total, with seven correlated across years (labeled “Year” below) and the remainder
2037 uncorrelated across years. They affect the b-tag jet p_T and mass, and hence the
2038 missing transverse energy p_T^{miss} . The shifts are propagated through the b-tagging
2039 scale factor calculation and b-tag jet counting.

2040 The uncertainties in the jet energy correction and resolution [89] [98] are as follows:

- 2041 • *Absolute, AbsoluteYear*: flat absolute scale uncertainties.
- 2042 • *BBEC1, BBEC1Year*: for sub-detector regions, with barrel “BB” in $|\eta| < 1.3$
2043 and endcap region 1 “EC1”: $1.3 < |\eta| < 2.5$.
- 2044 • *EC2, EC2 year*: for sub-detector regions, with endcap region 2 “EC2” in $2.5 <$
2045 $|\eta| < 3.0$.
- 2046 • *HF, HF year*: for sub-detector regions, with hadron forward “HF” in $|\eta| > 3$.
- 2047 • *FlavorQCD*: for uncertainty in jet flavor (uds/c/b-quark and gluon) estimates
2048 based on comparing Pythia and Herwig (different MC generator) predictions.
- 2049 • *RelativeBal*: account for difference between log-linear fits of the two methods
2050 used to study the jet energy response: MPF (missing transverse momentum
2051 projection fraction) and p_T balance.
- 2052 • *RelativeSample*: account for η -dependent uncertainty due to a difference be-
2053 tween relative residuals, observed with dijet and Z+jets in Run D of 2018 data.
- 2054 • *JetResolution*: uncertainty in the jet energy resolution.

2055 8.4 Uncertainties from b-tagging scale factors

2056 The b-tagging scale factor has its own set of associated uncertainties (not to be
2057 confused with shifts in the b-tagging scale factor due to the propagation of the jet
2058 energy scale uncertainties described in the previous section 8.3). They are:

- 2059 • hf : contamination from heavy flavor ($b+c$) jets in the light flavor region.
 - 2060 • $hfstats1, hfstats2$: linear and quadratic statistical fluctuations from b -flavor jets.
 - 2061 • lf : contamination from light flavor ($udsg+c$ jets) in the heavy flavor region.
 - 2062 • $lfstats1, lfstats2$: linear and quadratic statistical fluctuations from $udsg$ jets.
 - 2063 • $cferr, cferr2$: uncertainty for charm jets.
- 2064 The variations for “ $lf, hf, hfstats1/2, lfstats1/2$ ” are applied to both b and $udsg$ jets.
2065 For c -flavor jets, only “ $cferr1/2$ ” is applied.

2066 8.5 Uncertainties from MET

2067 Samples where recoil corrections were applied ($Z+jets$, $W+jets$, and Standard Model
2068 Higgs, as described in Section 5.3) have uncertainties from the response and resolution
2069 of the hadronic recoil against the leptonic system. These are each binned in jet
2070 multiplicity.

2071 8.6 Uncertainties associated with samples used

2072 Normalization uncertainties related to the samples used are:

- 2073 • *Cross-section uncertainties*: $\sigma(t\bar{t})$: 4.2%, $\sigma(\text{diboson})$: 5%, $\sigma(\text{single top})$: 5%,
2074 $\sigma(\text{ggH})$: 3.2%, $\sigma(\text{qqH})$: 2.1%, $\sigma(\text{WH})$: 1.9%, $\sigma(\text{ZH})$: 1.3%, $\sigma(\text{ttH})$: 3.6%

2075 • *Uncertainties in QCD renormalization scale*: QCD scale(qqH): +0.43%-0.33%,

2076 QCD scale(WH): +0.5%-0.7%, QCD scale(ttH): +5.8%-9.2%

2077 • *Branching ratio uncertainties*: BR($H \rightarrow \tau\tau$): 1.8%, and BR($H \rightarrow WW$): 1.5%.

2078 • *Normalization uncertainties*: 2% for Drell-Yan, 4% for embedded, 20% pre-fit
2079 for the QCD multijet background in the $e\mu$ channel, 20% pre-fit for the jet
2080 faking background.

2081 The $t\bar{t}$ process has additional acceptance uncertainties from QCD scale variation
2082 and parton shower uncertainties [99]. Parton shower uncertainties originate from
2083 the modeling of perturbative and non-perturbative QCD effects handled in parton
2084 shower MC generators. The scale variations are determined from the envelope of the
2085 6 provided shapes due to variations in the factorization scale, renormalization scale,
2086 and their combined variation [99].

2087 The Z p_T reweighing uncertainty in Drell-Yan samples is taken to be 10% of the
2088 nominal value, taken as a shape uncertainty.

2089 The fake rate uncertainties are taken as shape uncertainties. For the weight ap-
2090 plied to scale up anti-isolated events in cross-trigger regions, 20% of the nominal
2091 weight is taken as a shape uncertainty.

2092 8.7 Other uncertainties

2093 A 3.6% yield uncertainty in the signal is used to cover uncertainties in the parton
2094 distribution functions, α_s (fine structure constant), and QCD scale.

2095 Normalization uncertainties from luminosity are applied to all MC samples, di-
2096 vided into those uncorrelated across years, those correlated between 2017 and 2018,
2097 and one for 2018 [86].

2098 8.8 Pulls and impacts

2099 The top impacts and pulls computed for the combination of all channels and years is
2100 shown in Fig. 8.1. The top impacts are related to uncertainty in the signal sample and
2101 cross-section of the $t\bar{t}$ cross-section, and also the yields of the jet faking τ_h background,
2102 which is a major background in all channels and expected to be constrained due to
2103 the yield uncertainty which is taken to be 20% pre-fit.

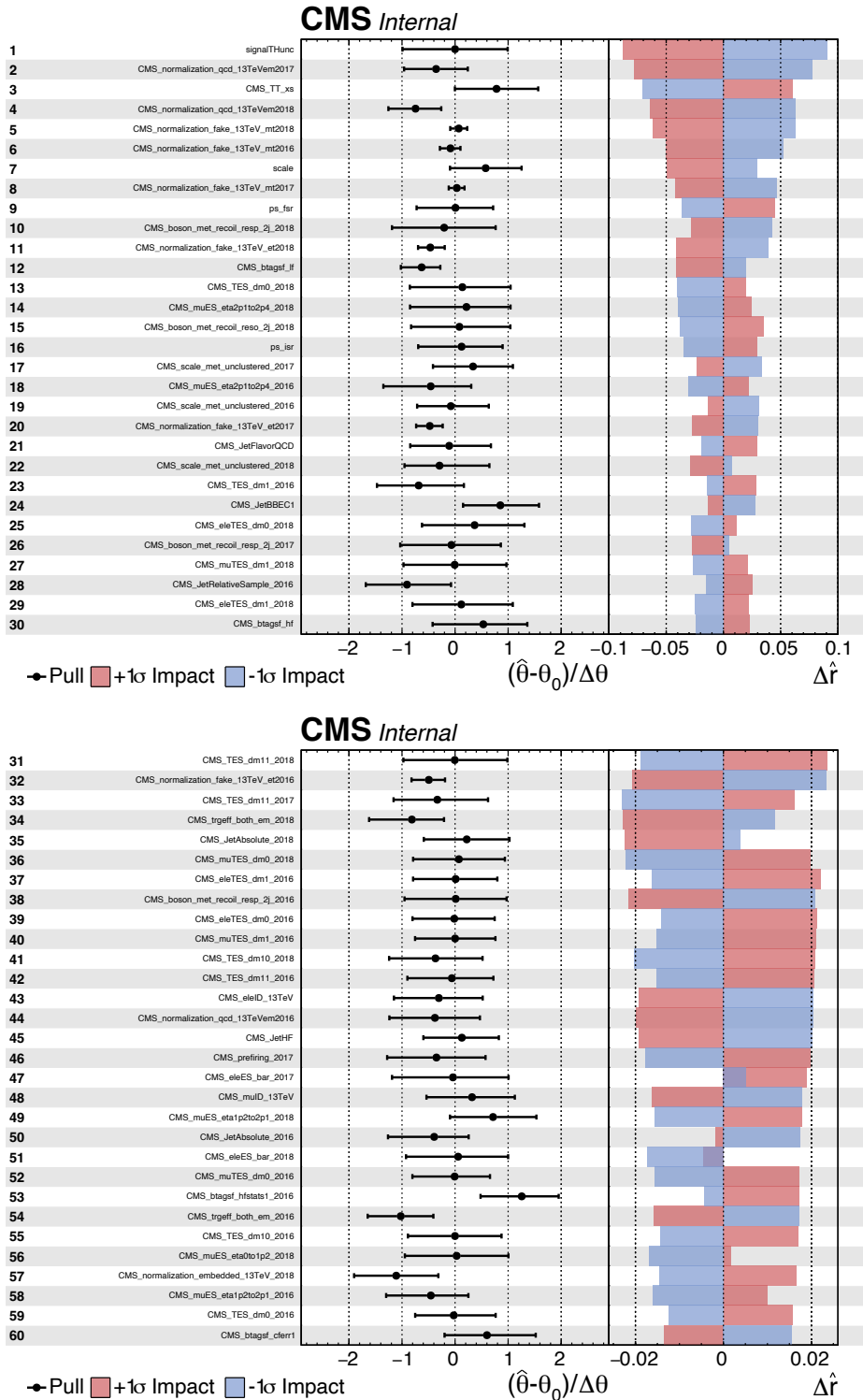


Figure 8.1: Top sixty pulls and impacts for the combination of all channels and years [45].

2104 **Chapter 9**

2105 **Event categorization and signal
2106 extraction**

2107 Measured events are divided into categories, based on cuts on values of observables
2108 in the event, or some derived quantity based on the observables in the event. The
2109 objective of event categorization is to divide events into signal regions, where the
2110 signal is enhanced and the background is suppressed, and control regions, which are
2111 signal-poor and used to check that the background estimation methods employed in
2112 the analysis in fact accurately models the data. In this analysis, events in each tau-tau
2113 channel are selected to contain one or more b-tag jets reconstructed in the event as
2114 described in Section 9.1. Events are further divided into signal and control regions
2115 using a deep learning-based approach described in Section 9.2. The signal is extracted
2116 from the di-tau mass distribution in the signal region using the statistical procedure
2117 described in Section 9.3.

2118 **9.1 B-tag jet multiplicity**

2119 The increased statistics of the full Run-2 dataset enables the separation of events into
2120 events with exactly 1 b-tag jet and events with greater than 1 b-tag jet. Further event

2121 categorization is performed with deep neural networks (DNNs) described below. The
2122 DNNs are used only for separating events into signal and control regions in the 1
2123 b-tag and 2 b-tag jets scenarios. The final results are extracted from the statistical
2124 fitting to the mass of the $\tau\tau$, $m_{\tau\tau}$.

2125 9.2 DNN-based event categorization

2126 Neural networks for event categorization are trained for each of the $\mu\tau_h$, $e\tau_h$, and $e\mu$
2127 channels, for 1 and 2 b-tag jets, giving $3 \times 2 = 6$ networks in total. In the training,
2128 the signal is taken to be all of the possible pseudoscalar mass m_a hypotheses together.
2129 The backgrounds for each DNN are taken to be a representative combination of the
2130 three major backgrounds: $Z \rightarrow \tau\tau$, $t\bar{t} + \text{jets}$, and fake backgrounds. The proportions of
2131 each background for each channel and b-tag jet multiplicity are taken from the yields
2132 in the $m_{\tau\tau}$ distribution. For instance, in the $\mu\tau_h$ 1 b-tag jet category, the composition
2133 of the background for training is 17.4% from $Z \rightarrow \tau\tau$, 42.4% from $t\bar{t} + \text{jets}$, and 40.2%
2134 fakes.

2135 The input variables capture the key differences between the signal and the back-
2136 ground:

- 2137 • Transverse momentum p_T of the electron and muon in the $e\tau_h$ and $\mu\tau_h$ channels,
2138 where the signal tends to have a softer p_T spectrum (lower energy) than the
2139 background.
- 2140 • p_T of the b-tag jet(s). The signal sample b-tag jet(s) tend to have softer p_T .
- 2141 • Invariant masses of the various objects ($\tau\tau$ legs and the b-tag jet(s)), which
2142 tend to be smaller for the signal samples.
- 2143 • The angular separation ΔR between pairs of the objects, where signal samples
2144 peak at smaller ΔR values.

- 2145 • The transverse mass between the missing transverse energy p_T^{miss} and each of
 2146 the four objects [85], defined as

$$m_T(\ell, p_T^{\text{miss}}) \equiv \sqrt{2p_T^\ell \cdot p_T^{\text{miss}}[1 - \cos(\Delta\phi)]} \quad (9.1)$$

2147 where p_T^ℓ is the transverse momentum of the object ℓ , and $\Delta\phi$ is the difference
 2148 in azimuthal angle between the object and the p_T^{miss} . Events from $t\bar{t}$ +jets and
 2149 jets faking τ_h backgrounds have larger p_T^{miss} resulting in larger transverse mass
 2150 values compared to the signal, which tends to have smaller p_T^{miss} that is also
 2151 more aligned with the lepton legs.

- 2152 • The variable D_ζ [85], defined as

$$D_\zeta \equiv p_\zeta - 0.85p_\zeta^{\text{vis}} \quad (9.2)$$

2153 where the ζ axis is the bisector of the transverse directions of the visible τ decay
 2154 products. p_ζ is the component of the p_T^{miss} along the ζ axis, and p_ζ^{vis} is the sum
 2155 of the components of the lepton p_T along the same axis. This variable captures
 2156 the fact that in signal the p_T^{miss} is small and approximately aligned with the $\tau\tau$.
 2157 In contrast, the $Z \rightarrow \tau\tau$ background tends towards large D_ζ values because the
 2158 p_T^{miss} is collinear to the $\tau\tau$, and the $t\bar{t}$ +jets events tend to have small D_ζ due to
 2159 a large p_T^{miss} not aligned with the $\tau\tau$.

- 2160 • For events with 2 b-tag jets, one additional variable is defined to capture the
 2161 difference in the invariant mass of the bb and the $\tau\tau$:

$$\Delta m_{a_1} \equiv (m_{bb} - m_{\tau\tau})/m_{\tau\tau} \quad (9.3)$$

2162 This variable peaks at zero for the $h \rightarrow aa \rightarrow 2b2\tau$ signal.

After training, events in data, MC, and embedded are evaluated with the six DNNs and assigned a raw score between 0 and 1 (background-like or signal-like). In order to flatten the distribution of the score and define score thresholds for categorizing events, the raw output scores are transformed with the function $\tilde{p}(n) = \text{arctanh}(p \times \tanh(n))/n$ where n is a positive integer. The thresholds of the DNN score used for signal/control region definition are determined using scans that optimize the signal sensitivity and are shown in Tables 9.1 and 9.2.

1bNN $\tilde{p}(n = 1.5)$				
	SR1	SR2	SR3	CR
$\mu\tau_h$ 2018	> 0.98	$\in [0.95, 0.98]$	$\in [0.90, 0.95]$	< 0.90
$\mu\tau_h$ 2017	> 0.97	$\in [0.94, 0.97]$	$\in [0.90, 0.94]$	< 0.90
$\mu\tau_h$ 2016	> 0.97	$\in [0.94, 0.97]$	$\in [0.89, 0.94]$	< 0.89
1bNN $\tilde{p}(n = 1.5)$				
	SR1	SR2	SR3	CR
$e\tau_h$ 2018	> 0.97	$\in [0.945, 0.97]$	$\in [0.90, 0.945]$	< 0.90
$e\tau_h$ 2017	> 0.985	$\in [0.965, 0.985]$	$\in [0.93, 0.965]$	< 0.93
$e\tau_h$ 2016	> 0.985	$\in [0.965, 0.985]$	$\in [0.93, 0.965]$	< 0.93
1bNN $\tilde{p}(n = 2.5)$				
	SR1	SR2	SR3	CR
$e\mu$ 2018	> 0.99	$\in [0.95, 0.99]$	$\in [0.85, 0.95]$	< 0.85
$e\mu$ 2017	> 0.985	$\in [0.95, 0.985]$	$\in [0.85, 0.95]$	< 0.85
$e\mu$ 2016	> 0.99	$\in [0.95, 0.99]$	$\in [0.85, 0.95]$	< 0.85

Table 9.1: Event categorization based on DNN scores for events with exactly 1 b-tag jet (1bNN), for the three $\tau\tau$ channels and three eras.

9.3 Methodology for signal extraction

After events are divided into categories, the data is compared to the expected backgrounds in the signal region categories. Here, we describe the fundamental concepts behind hypothesis testing in high-energy physics, as well as how exclusion limits can be set on parameters whose true values we cannot measure, culminating in the modified frequentist method CL_S which is used to perform signal extraction in this

	2bNN $\tilde{p}(n = 1.5)$		
	SR1	SR2	CR
$\mu\tau_h$ 2018	> 0.99	$\in [0.96, 0.99]$	< 0.96
$\mu\tau_h$ 2017	> 0.98	$\in [0.94, 0.98]$	< 0.94
$\mu\tau_h$ 2016	> 0.97	$\in [0.93, 0.97]$	< 0.93
	2bNN $\tilde{p}(n = 1.5)$		
	SR1	SR2	CR
$e\tau_h$ 2018	> 0.96	NA	< 0.96
$e\tau_h$ 2017	> 0.985	NA	< 0.985
$e\tau_h$ 2016	> 0.96	NA	< 0.96
	2bNN $\tilde{p}(n = 2.5)$		
	SR1	SR2	CR
$e\mu$ 2018	> 0.98	$\in [0.94, 0.98]$	< 0.94
$e\mu$ 2017	> 0.97	$\in [0.93, 0.97]$	< 0.93
$e\mu$ 2016	> 0.98	$\in [0.94, 0.98]$	< 0.94

Table 9.2: Event categorization based on DNN scores for events with 2 b-tag jets (2bNN), for the three $\tau\tau$ channels and three eras.

²¹⁷⁶ analysis.

²¹⁷⁷ 9.3.1 Model building and parameter estimation

In the frequentist interpretation of probability, an experiment measuring an observable can be repeated, resulting in different values of the observable, e.g. the invariant mass of a candidate Higgs boson in a search for the Higgs [100]. The ensemble of values of the observable x gives rise to the probability density function (PDF) $f(x)$, which has the important property that it is normalized to unity:

$$\int f(x) dx = 1.$$

A parametric family of PDFs

$$f(x|\alpha),$$

2178 read “ f of x given α ”, is referred to as a probability model or model. The parameters α
 2179 typically represent parameters of the theory or an unknown property of the detector’s
 2180 response. The parameters are not frequentist in nature, unlike x . Out of all the
 2181 parameters, typically only a few are of interest, and are called the parameters of
 2182 interest (POI), labeled μ here. The remaining are referred to as nuisance parameters
 2183 (NP) [100] and are labeled θ .

2184 $f(x)$ is the probability density for the observable in one event and we wish to
 2185 describe the probability density for a dataset with many events, $\mathcal{D} = \{x_1, \dots, x_n\}$,
 2186 called the total probability model \mathbf{f} . For instance, if we also have a prediction for
 2187 the total number of events expected, called ν , we also account for the overall Poisson
 2188 probability for observing n events given ν expected:

$$\mathbf{f}(\mathcal{D}|\nu, \alpha) = \text{Poisson}(n|\nu) \prod_{e=1}^n f(x_e|\alpha) \quad (9.4)$$

The likelihood function $L(\alpha)$ is numerically equivalent to $f(x|\alpha)$ for fixed x , or
 $\mathbf{f}(\mathcal{D}|\alpha)$ with \mathcal{D} fixed [100]. The likelihood function is not a probability density for α
 and is not normalized to unity:

$$\int L(\alpha) d(\alpha) \neq 1.$$

2189 i.e. the likelihood function is the value of f as a function of α given a fixed value of
 2190 x .

2191 To estimate the parameter α we use an estimator, which is a function of the
 2192 data. Take for example the measurement of data distributed according to a Gaussian
 2193 probability density $f(x|\mu, \sigma) = \text{Gauss}(x|\mu, \sigma)$. One possible estimator of the mean μ ,
 2194 is the mean of the measured data points $\bar{x} = \sum_{i=1}^n x_i/n$ [100].

2195 A commonly used estimator in physics is the maximum likelihood estimator
 2196 (MLE), defined as the value α which maximizes the likelihood function $L(\alpha)$. This

2197 value, labeled $\hat{\alpha}$, also maximizes $\ln L(\alpha)$ and minimizes $-\ln L(\alpha)$. By convention the
2198 $-\ln L(\alpha)$ is minimized, in a process called “fitting”, and the maximum likelihood
2199 estimate is called the “best fit value”.

2200 **9.3.2 Hypothesis testing**

2201 In this section we next introduce concepts related to hypothesis testing such as the
2202 test statistic constructed from the ratio of likelihood functions.

2203 The objective of a likelihood analysis is to distinguish different models repre-
2204 senting the various hypotheses, and determine the one that best explains the ex-
2205 perimental outcome. In a search for new physics, a signal is additive on top of the
2206 background. The background-only hypothesis is the null hypothesis, and the signal-
2207 plus-background hypothesis is the alternative.

2208 As a simple example, take the p -value test, for an experiment where we count
2209 events in the signal region, n_{SR} , and expect ν_B background events and ν_S events from
2210 the signal [100]. Then

2211 1. The null hypothesis (H_0), i.e. the background-only hypothesis in this experi-
2212 ment, with the probability modeled by $\text{Poisson}(n_{SR}|\nu_B)$.

2213 2. The alternate hypothesis (H_1), i.e. signal-plus-background hypothesis, with the
2214 probability modeled by $\text{Poisson}(n_{SR}|(\nu_B + \nu_S))$.

2215 The compatibility of the observed data n_{SR}^0 and the null hypothesis, is quantified as
2216 the probability that the background-only hypothesis would produce at least as many
2217 events as was observed. This probability is the p -value:

$$p = \sum_{n=n_{SR}^0}^{\infty} \text{Poisson}(n|\nu_B). \quad (9.5)$$

2218 If the p -value is very small, we might reject the null hypothesis. The p -value is not the

2219 probability of the null hypothesis given the data; rather, it expresses the probability
2220 that data with a certain property was obtained, assuming the null hypothesis [100].

2221 The p -value is an example of a test statistic T , which maps the data to a single
2222 real number. The Neyman-Pearson lemma states that out of the infinite possibilities
2223 of choices of test statistic, the uniformly most powerful test statistic is the likelihood
2224 ratio T_{NP} [100]:

$$T_{NP}(\mathcal{D}) = \frac{L(\mathcal{D}|H_1)}{L(\mathcal{D}|H_0)} \quad (9.6)$$

To reiterate, the test statistic T is a real-valued function of the data, implying that a particular probability model $\mathbf{f}(\mathcal{D}|\boldsymbol{\alpha})$ implies a distribution of the test statistic, $f(T|\boldsymbol{\alpha})$, which depends on the value of $\boldsymbol{\alpha}$. With this distribution in hand, the p -value can be evaluated in the following equivalent formulations:

$$p(\boldsymbol{\alpha}) = \int_{T_0}^{\infty} f(T|\boldsymbol{\alpha}) dT \quad (9.7)$$

$$= \int \mathbf{f}(\mathcal{D}|\boldsymbol{\alpha}) \theta(T(\mathcal{D}) - T_0) d\mathcal{D} \quad (9.8)$$

$$= P(T \geq T_0|\boldsymbol{\alpha}) \quad (9.9)$$

2225 where T_0 is the value of T based on the observed data, and $\theta()$ is the Heaviside
2226 function. The size of the test is conventionally chosen to be 10%, 5%, or 1%. As
2227 the p -value depends on $\boldsymbol{\alpha}$ (both the POI and NP), the null hypothesis should not be
2228 rejected if the p -value is larger than the size of the test for any value of the nuisance
2229 parameters.

2230 9.3.3 Confidence intervals

2231 In an example of the measurement of the Standard Model Higgs boson, $\boldsymbol{\alpha}_{POI} =$
2232 $(\sigma/\sigma_{SM}, M_H)$, with σ/σ_{SM} is the ratio of the production cross-section for Higgs with

respect to its value in the SM, and M_H is the unknown mass of the Higgs, values of these parameters outside specific bounds are said to be “excluded at the 95% confidence level”. These allowed regions are called confidence levels or confidence regions, and the parameter values outside of them are considered excluded [100]. A 95% confidence interval does not mean that there is a 95% chance that the true value of the parameter is inside the interval. Rather, a 95% confidence interval covers the true value 95% of the time (even though we do not know the true value).

To construct a confidence interval for a parameter α , the Neyman Construction is used to invert a series of hypothesis tests; i.e. for each possible value of α , the null hypothesis is treated as α , and we perform a hypothesis test based on a test statistic. To construct a 95% confidence interval, we construct a series of hypothesis tests with size of 5%. The confidence interval $I(\mathcal{D})$ is constructed by taking the set of parameter values $\boldsymbol{\alpha}$ where the null hypothesis is accepted:

$$I(\mathcal{D}) = \{\boldsymbol{\alpha} | P(T(\mathcal{D}) > k_\alpha | \boldsymbol{\alpha}) < \alpha\}, \quad (9.10)$$

where $T(\mathcal{D})$ is the test statistic, and the last α (not bolded) and the subscript k_α refer to the size of the test. A schematic of the Neyman construction is shown in Fig. 9.1. In a more generalized case, the x -axis is the test statistic T .

9.3.4 Profile likelihood ratio

In this section we describe a frequentist statistical procedure based on the profile likelihood ratio test statistic, which is implemented using asymptotic distributions.

With a multi-parameter likelihood function $L(\boldsymbol{\alpha})$, the maximum likelihood of one specific parameter α_p with other parameters $\boldsymbol{\alpha}_o$ fixed, is called the conditional maximum likelihood estimate and is denoted $\hat{\alpha}_p(\boldsymbol{\alpha}_0)$. The process of choosing specific values of the nuisance parameters for a given value of μ , $\mathcal{D}_{\text{simulated}}$, and value of global

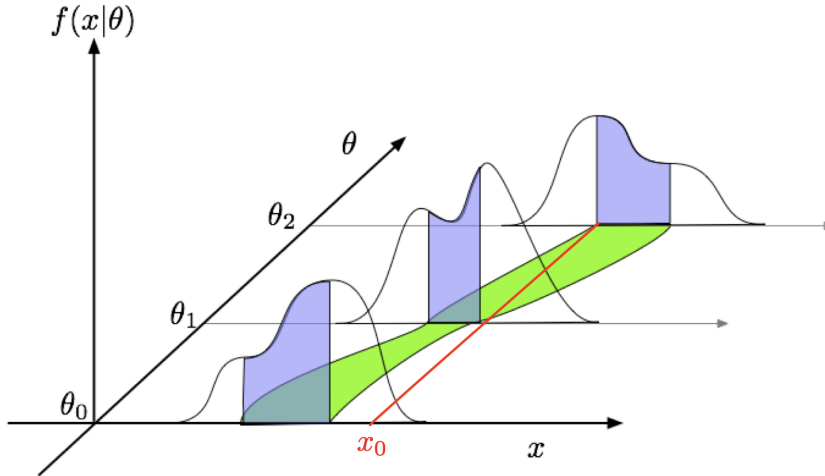


Figure 9.1: Schematic of the Neyman construction for confidence intervals [100]. For each value of θ , we find a region in x where $\int f(x|\theta)dx$ satisfies the size of the test (blue). These regions form a confidence belt (green). The intersection of the observation x_0 (red) with the confidence belt defines the confidence interval $[\theta_1, \theta_2]$ [100].

2256 observables \mathcal{G} is called profiling. From the full list of parameters $\boldsymbol{\alpha}$, we denote the
2257 parameter of interest μ , and the nuisance parameters $\boldsymbol{\theta}$.

2258 We construct the profile likelihood ratio,

$$\lambda(\mu) = \frac{L(\mu, \hat{\boldsymbol{\theta}}(\mu))}{L(\mu, \hat{\boldsymbol{\theta}})} \quad (9.11)$$

2259 which depends explicitly on the parameter of interest μ , implicitly on the data \mathcal{D}_{sim}
2260 and global observables \mathcal{G} , and is independent of the nuisance parameters $\boldsymbol{\theta}$, which
2261 have been eliminated in profiling [100].

2262 The main conceptual reason for constructing the test statistic from the profile
2263 likelihood ratio is that asymptotically (i.e. for measurements with many events) the
2264 distribution of the profile likelihood ratio $\lambda(\mu = \mu_{\text{true}})$ is independent of the values of
2265 the nuisance parameters [100].

2266 The following p -value is used to quantify the consistency with the hypothesis of a
2267 signal strength of μ :

$$p_\mu = \int_{\tilde{q}_{\mu,\text{obs}}}^{\infty} f(\tilde{q}_\mu | \mu, \hat{\boldsymbol{\theta}}(\mu, \text{obs})) d\tilde{q}_\mu \quad (9.12)$$

2268 9.3.5 Modified frequentist method: CL_S

2269 In the modified frequentist method called CL_S , to test a hypothesis with signal, we
 2270 define p'_μ as a ratio of p -values [100]:

$$p'_\mu = \frac{p_\mu}{1 - p_b} \quad (9.13)$$

2271 where p_b is the p -value derived under the background-only hypothesis:

$$p_b = 1 - p_0 \equiv 1 - \int_{\tilde{q}_{\mu,\text{obs}}}^{\infty} f(\tilde{q}_\mu | 0, \hat{\theta}(\mu = 0, \text{obs})) d\tilde{q}_\mu. \quad (9.14)$$

2272 The CL_S upper limit on μ , denoted μ_{up} , is obtained by solving for $p'_{\mu_{up}} = 5\%$.
 2273 If testing the compatibility of the data with the background-only hypothesis, we
 2274 consider the p_b value defined above and conventionally convert it into the quantile
 2275 or “sigma” of a unit Gaussian. z standard deviations (e.g. $z = 5$ in “ 5σ ”) means
 2276 that the probability of falling above these standard deviations, equals p_b (e.g. 3σ
 2277 corresponds to $p_b = 2.7 \times 10^{-3}$ or 95.43%, and 5σ corresponds to $p_b = 5.7 \times 10^{-7}$ or
 2278 99.999943%).

2279 **Chapter 10**

2280 **Results**

2281 In this chapter, Section 10.1 presents the results from the $h \rightarrow aa \rightarrow bb\tau\tau$ analysis
2282 performed on 137 fb^{-1} of data from the full CMS Run-2 dataset in the years 2016 to
2283 2018, with interpretations provided for different 2HDM+S scenarios. This analysis
2284 was combined with a different search in the $h \rightarrow aa \rightarrow bb\mu\mu$ final state, which was
2285 also performed on the full Run-2 dataset. The combination procedure and results
2286 from the combined analyses ($h \rightarrow aa \rightarrow bb\ell\ell$, with $\ell = \mu, \tau$) are detailed in 10.2.
2287 The combined analysis places some of the most stringent limits to date at CMS for
2288 2HDM+S scenarios in the light scalar mass range $m_a = 12 \text{ GeV}$ to 60 GeV .

2289 **10.1 Results from $bb\tau\tau$**

2290 In each of the three $\tau\tau$ channels studied ($\mu\tau_h$, $e\tau_h$, and $e\mu$), events are divided based
2291 on whether they contain exactly 1 or 2 b-tag jets, and further divided into signal
2292 and control regions (SRs and CRs) using the DNN categorization score as described
2293 in Section 9.2. The control regions demonstrate good agreement between observed
2294 events in data, and the sum of the contributions from expected backgrounds that
2295 are modeled in simulated and embedded samples. The signal regions are defined to
2296 be sensitive to the $h \rightarrow aa \rightarrow bb\tau\tau$ signal. The postfit final observed and expected

2297 distributions of the di-tau invariant mass $m_{\tau\tau}$ reconstructed with SVFit (described
2298 in Section 5.2) are shown in Fig. 10.1 for the $\mu\tau_h$ channel, Fig. 10.2 for the $e\tau_h$
2299 channel, and Fig. 10.3 for the $e\mu$ channel. In all figures, the hypothesized yield for
2300 the $h \rightarrow aa \rightarrow bb\tau\tau$ signal is shown for the pseudoscalar mass $m_a = 35$ GeV and
2301 assuming a branching fraction $B(H \rightarrow aa \rightarrow bb\tau\tau) = 10\%$.

2302 The 95% CL expected and observed exclusion limits on the signal strength of the
2303 branching fraction $B(h \rightarrow aa \rightarrow bb\tau\tau)$ as a function of the pseudoscalar mass m_a
2304 ranging from 12 GeV to 60 GeV, are shown for the three $\tau\tau$ channels and all three
2305 channels combined in Fig. 10.4. The limits are shown as percentages and normalized
2306 to the production cross-section of the Standard Model Higgs boson. No excess of
2307 events above the Standard Model expectations is observed. In the limits for the three
2308 $\tau\tau$ channels combined, expected (observed) limits range from 1.4 to 5.6% (1.7 to
2309 7.6%) for pseudoscalar masses between 12 and 60 GeV.

2310 The $e\mu$ channel is the only channel that has signal sensitivity to the $m_a = 12$
2311 GeV pseudoscalar mass hypothesis, because the minimum required spatial separation
2312 $\Delta R = \sqrt{(\Delta\eta)^2 + (\Delta\phi)^2}$ between the two τ legs is smaller than the other two channels
2313 ($\Delta R < 0.3$ for $e\mu$, compared to $\Delta R < 0.4$ for the other two channels). This decreased
2314 ΔR requirement results in better signal acceptance for low mass signals for the $e\mu$
2315 channel. The $\mu\tau_h$ and $e\tau_h$ channels are most sensitive to the intermediate mass points
2316 studied, since the analysis targets a resolved signature: at low mass points, the tau
2317 legs are boosted, and at high mass points, the $m_{\tau\tau}$ distributions in signal have larger
2318 overlap with background distributions. In the combination of the three $\tau\tau$ channels,
2319 the limit for $m_a = 12$ GeV comes only from the $e\mu$ channel, and the best sensitivity
2320 is attained at intermediate mass points around $m_a = 20$ GeV to 45 GeV.

2321 To set limits on the branching fraction of the 125 GeV Higgs to the two pseu-
2322 doscalars, $B(h \rightarrow aa)$, we interpret the results in four types of 2HDM+S, which were
2323 introduced in Section 1.4. In 2HDM+S, the theorized branching fraction of the pseu-

2324 doscalars depends on the 2HDM+S model type, the pseudoscalar mass m_a , and the
2325 ratio of the two Higgs doublets' vacuum expectation values $\tan \beta$. In Type I models,
2326 the branching fraction is independent of $\tan \beta$, while in Types II, III, and IV, it is
2327 a function of m_a and $\tan \beta$. Limits for the $bb\tau\tau$ final state as a function of m_a for
2328 2HDM+S Type I (valid for all $\tan \beta$ values), Type II with $\tan \beta = 2.0$, Type III with
2329 $\tan \beta = 2.0$, and Type IV with $\tan \beta = 0.6$ are overlaid and shown in Fig. 10.5a.

2330 10.2 Combination with $bb\mu\mu$ final state

2331 Results from this analysis for the $h \rightarrow aa \rightarrow bb\tau\tau$ final state are combined with the
2332 analysis for the $h \rightarrow aa \rightarrow bb\mu\mu$ final state [101]. While the predicted branching ratio
2333 for $aa \rightarrow bb\mu\mu$ is comparatively small, the $bb\mu\mu$ final state has competitive results
2334 due to the excellent di-muon resolution measured by CMS. The $bb\mu\mu$ analysis uses
2335 an unbinned fit to the data using the di-muon mass $m_{\mu\mu}$ distribution. Details can be
2336 found in [101].

2337 Combining the results is possible since the $bb\tau\tau$ analysis explicitly rejects events
2338 with extra leptons, so there is no overlap between the events studied in the $bb\tau\tau$
2339 analysis and the $bb\mu\mu$ analysis. In the statistical combination, several systematic
2340 uncertainties are treated as correlated: the integrated luminosity normalization, the
2341 b-tagging scale factor, the scale factors related to muon reconstruction, identifica-
2342 tion, and trigger efficiencies, the inefficiency in the ECAL trigger readout, and the
2343 theoretical uncertainties related to signal modeling.

2344 Since the results in both final states are statistically limited, the combination ben-
2345 efits from the additional data. For $m_a = 35$ GeV, all systematic uncertainties amount
2346 to around 6% of the total uncertainty, with the dominant systematic uncertainties
2347 coming from jet energy systematics in the $bb\mu\mu$ final state, theoretical uncertainties
2348 in the signal, and uncertainties in the QCD multijet backgrounds in the $e\mu$ channel

2349 of the $bb\tau\tau$ final state.

2350 The mass distributions of the di-muon and di-tau objects ($m_{\mu\mu}$ and $m_{\tau\tau}$) are
2351 compared to the data in a combined maximum likelihood fit to derive upper limits
2352 on $B(h \rightarrow aa)$. The observed limits at 95% CL on $B(h \rightarrow aa)$ for different 2HDM+S
2353 scenarios, are shown for the search for $h \rightarrow aa \rightarrow bb\mu\mu$ in Fig. 10.5b, and the
2354 combined analyses $h \rightarrow aa \rightarrow bb\ell\ell$ in Fig. 10.6.

2355 Exclusion limits in a two-dimensional plane as a function of $\tan\beta$ and m_a are
2356 set for 2HDM+S Types II, III, and IV in Fig. 10.7. The most stringent constraints
2357 are observed for 2HDM+S type III because of large branching fractions predicted in
2358 theory, with predicted branching fractions between 0.47 and 0.42 for $\tan\beta = 2.0$ and
2359 values of m_a between 15 and 60 GeV, compared to the observed 95% CL upper limits
2360 which are between 0.08 and 0.03. For 2HDM+S type IV, the predicted branching
2361 fractions from theory are between 0.26 and 0.20 for $\tan\beta = 0.6$ for values of m_a
2362 between 15 and 60 GeV, and the 95% CL observed upper limits are between 0.12 and
2363 0.05.

2364 The combined results from $h \rightarrow aa \rightarrow bb\ell\ell$ are compared with CMS results in
2365 other final states as a function of the pseudoscalar mass m_a : for 2HDM+S type I in
2366 Fig. 10.8, type II with $\tan\beta = 2.0$ in Fig. 10.9, and type III with $\tan\beta = 2.0$ in Fig.
2367 10.10. In other scenarios, e.g. type III with $\tan\beta = 5.0$, more stringent limits are set
2368 by analyses in other final states, $\mu\mu\tau\tau$ in this case. Other summary plots for other
2369 model types and $\tan\beta$ values can be found at [102].

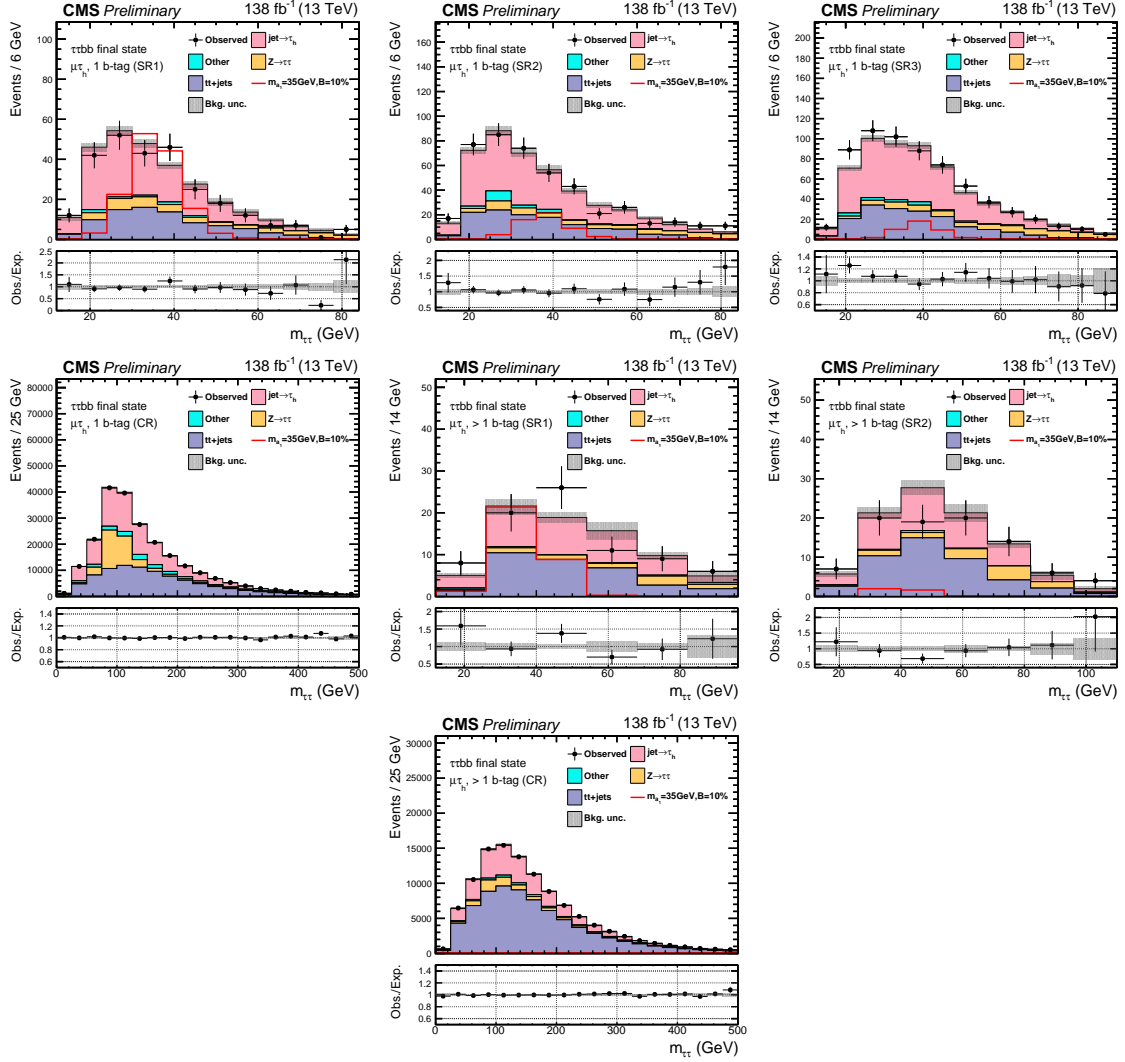


Figure 10.1: Postfit final $m_{\tau\tau}$ observed and expected distributions, and the observed/expected ratios, in the $\mu\tau_h$ channel [45]. Events are divided into the 1 b-tag jet signal regions (SR1, SR2, SR3) (*top row*), 1 b-tag jet control region (*middle row*), 2 b-tag jet signal regions (SR1, SR2) (*middle row*), and lastly the 2 b-tag jet control region (CR) (*bottom*). Statistical and systematic sources of uncertainties in the expected events are added in quadrature and labeled “Bkg. unc” (*shaded gray*). The dominant backgrounds in all categories are jets faking the τ_h leg (*pink*), $Z \rightarrow \tau\tau$ (*orange*), and $t\bar{t}+j$ ets (*purple*). For illustrative purposes, the beyond-Standard Model signal yield from $h \rightarrow aabb\tau\tau$ is shown for the pseudoscalar mass hypothesis $m_a = 35$ GeV, assuming a branching fraction $B(h \rightarrow aa \rightarrow bb\tau\tau) = 10\%$ (*red line*).

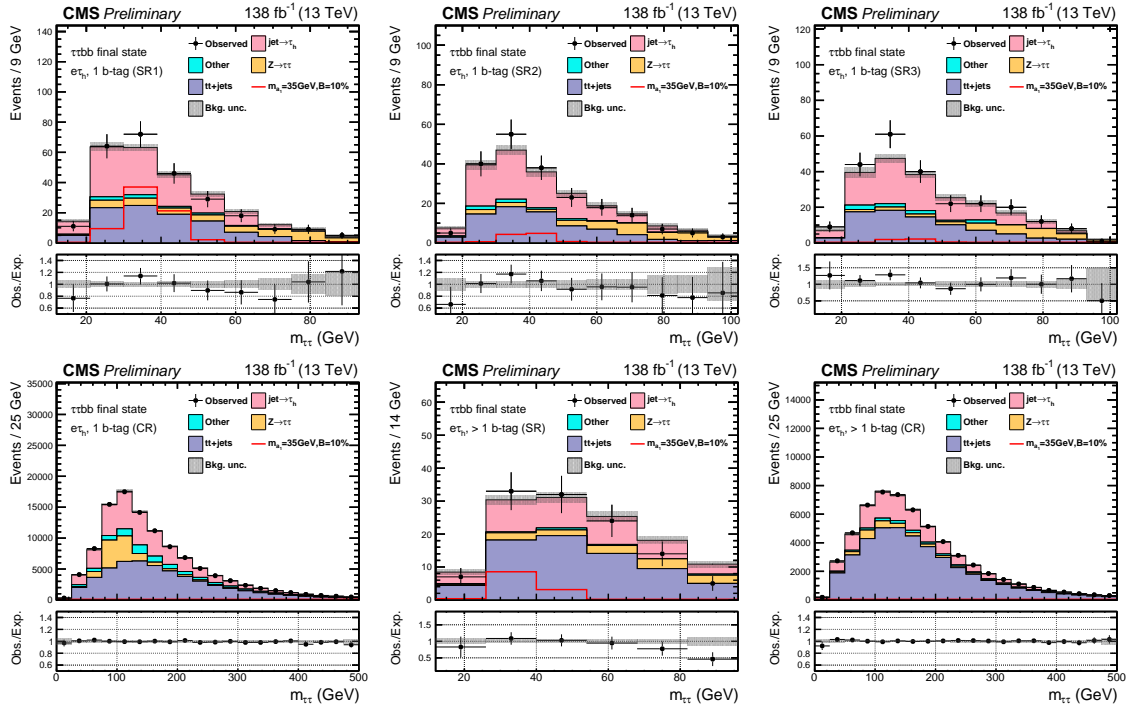


Figure 10.2: Postfit final observed and expected $m_{\tau\tau}$ distributions, and the observed/expected ratios, in the $e\tau_h$ channel [45]. Events are divided into the 1 b-tag jet signal regions (SR1, SR2, SR3) (*top row*), the 1 b-tag jet control region (CR) (*bottom row*), and 2 b-tag jet signal region (SR) and control region (CR) (*bottom row*). Statistical and systematic sources of uncertainties in the expected events are added in quadrature and labeled “Bkg. unc” (*shaded gray*). In this channel, the dominant backgrounds are jets faking the τ_h leg (*pink*), $Z \rightarrow \tau\tau$ (*orange*), and $t\bar{t}+j$ (*purple*). For illustrative purposes, the beyond-Standard Model signal yield from $h \rightarrow aabb\tau\tau$ is shown for the pseudoscalar mass hypothesis $m_a = 35$ GeV, assuming a branching fraction $B(h \rightarrow aa \rightarrow bb\tau\tau) = 10\%$ (*red line*).

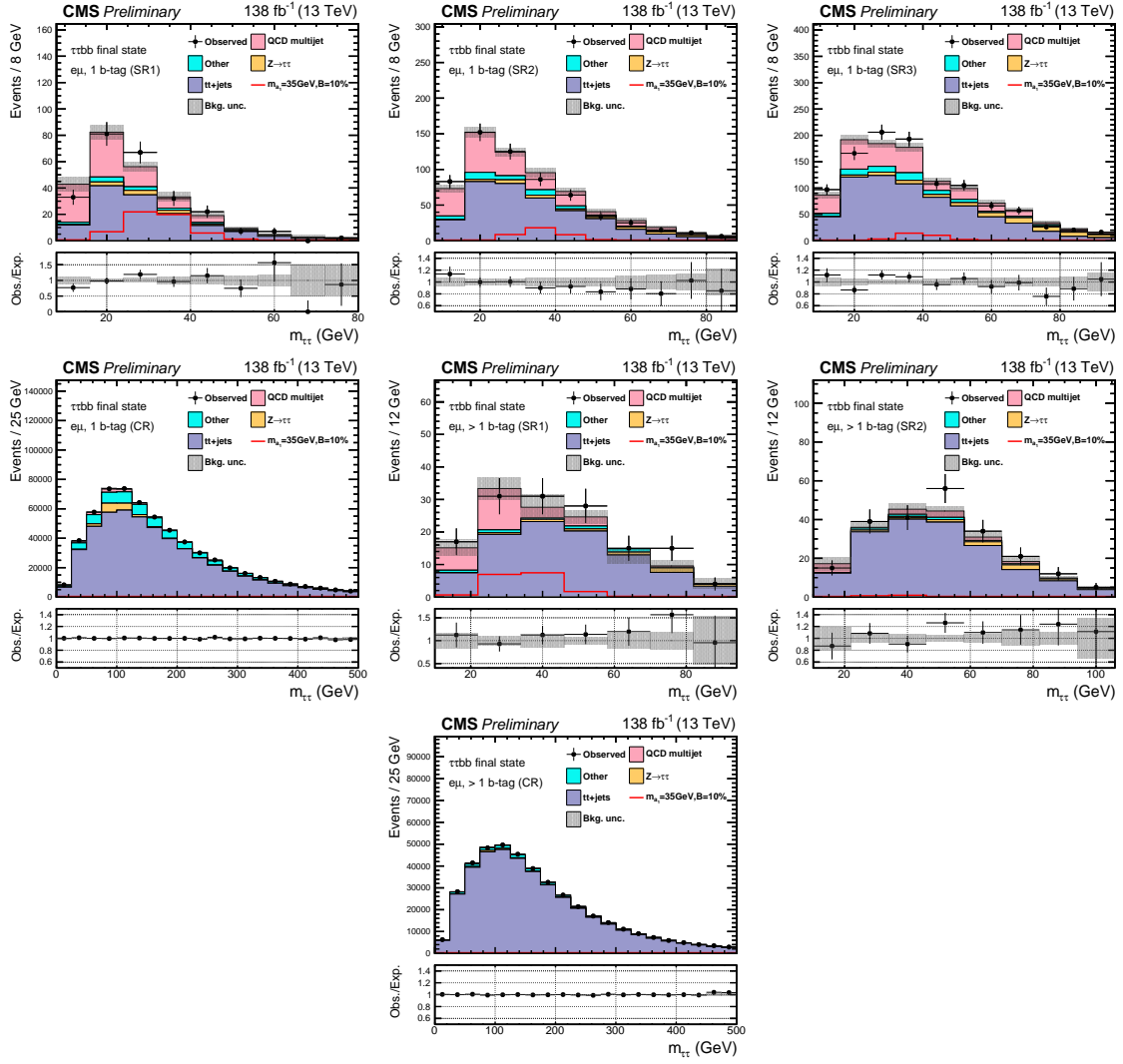


Figure 10.3: Postfit final observed and expected $m_{\tau\tau}$ distributions, and the observed/expected ratios, in the $e\mu$ channel [45]. Events are divided into the 1 b-tag jet signal regions (SR1, SR2, and SR3) (*top row*), 1 b-tag jet control region (CR) (*middle row*), 2 b-tag jet signal regions (SR1 and SR2) (*middle row*), and 2 b-tag jet control region (CR) (*bottom row*). Statistical and systematic sources of uncertainties in the expected events are added in quadrature and labeled “Bkg. unc” (*shaded gray*). The $t\bar{t}+j$ process (*purple*) is a major background, and in the signal regions the QCD multijet (*pink*) is also a major background. TFor illustrative purposes, the beyond-Standard Model signal yield from $h \rightarrow aabb\tau\tau$ is shown for the pseudoscalar mass hypothesis $m_a = 35$ GeV, assuming a branching fraction $B(h \rightarrow aa \rightarrow bb\tau\tau) = 10\%$ (*red line*).

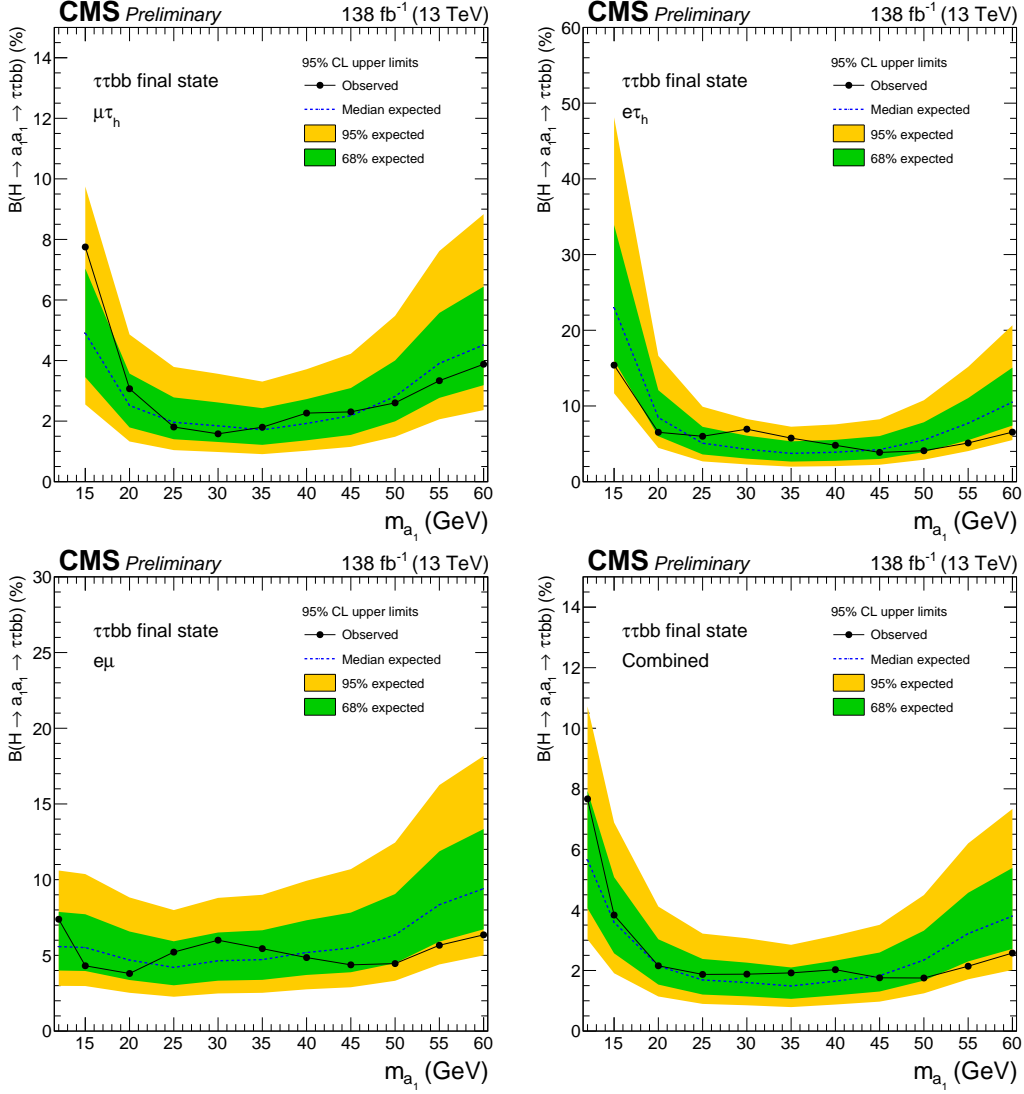
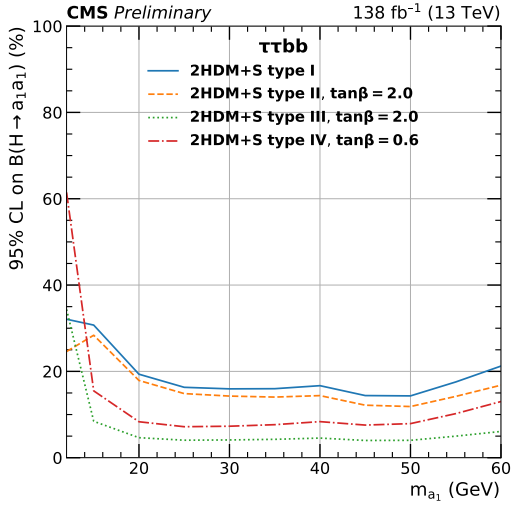
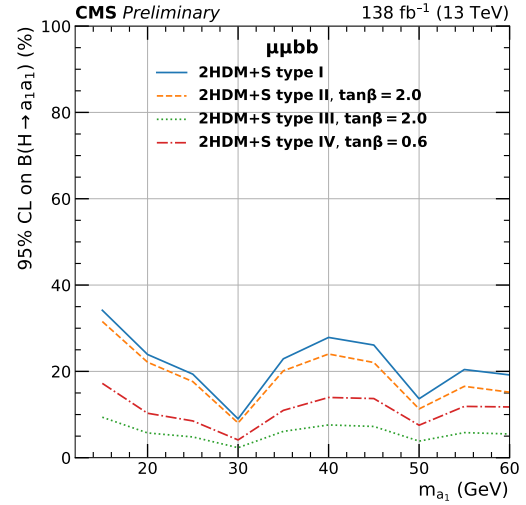


Figure 10.4: Observed 95% CL exclusion limits (*black, solid lines*) and expected 95% CL and 68% CL limits (*shaded yellow and green*) on the branching fraction $B(h \rightarrow aa \rightarrow bb\tau\tau)$ in percentages, assuming the Standard Model production for the 125 GeV Higgs (h). Limits are shown for the $\mu\tau_h$ channel (*top left*), the $e\tau_h$ channel (*top right*), and the $e\mu$ channel (*bottom left*), and lastly the combination of all three channels (*bottom right*) [45]. The dataset corresponds to 138 fb^{-1} of data collected in the years 2016-2018 at a center-of-mass energy 13 TeV. Only the $e\mu$ channel has sensitivity to the mass hypothesis $m_a = 12 \text{ GeV}$. The best sensitivity is attained at intermediate mass points.



(a) $bb\tau\tau$ final state.



(b) $bb\mu\mu$ final state.

Figure 10.5: Observed 95% CL upper limits on $B(h \rightarrow aa)$ in %, for the $bb\tau\tau$ final state (*left*) and $bb\mu\mu$ final state (*right*) using the full Run 2 integrated luminosity of 138 fb^{-1} in 2HDM+S type I (blue), type II with $\tan\beta = 2.0$ (orange dashed), type III with $\tan\beta = 2.0$ (dotted green), and type IV with $\tan\beta = 0.6$ (red dashed) [45]. Linear interpolation is used between points in the graphs. The $\tan\beta$ values chosen here correspond to the most stringent limits in each model.

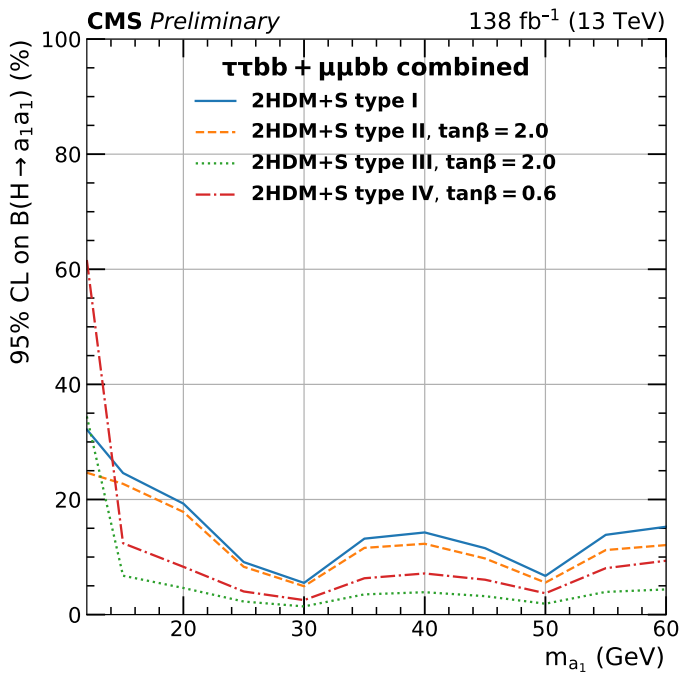


Figure 10.6: Observed 95% CL upper limits on the branching fraction of the 125 GeV Higgs boson to two pseudoscalars, $B(h \rightarrow aa)$, in percentages, as a function of the pseudoscalar mass m_a , in 2HDM+S type I (blue), type II with $\tan\beta = 2.0$ (orange dashed), type III with $\tan\beta = 2.0$ (dotted green), and type IV with $\tan\beta = 0.6$ (red dashed), for the combination of $bb\mu\mu$ and $bb\tau\tau$ channels using the full Run 2 integrated luminosity of 138 fb^{-1} [45].

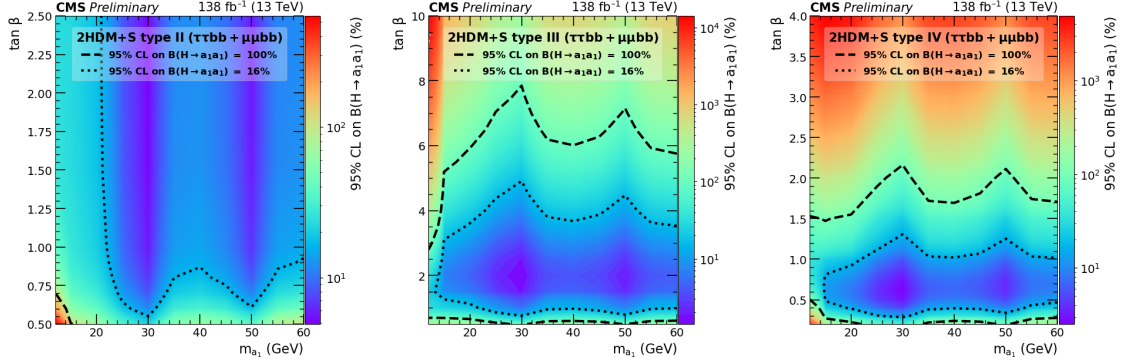


Figure 10.7: Observed 95% CL upper limits on $\mathcal{B}(h \rightarrow aa)$ in %, for the combination of $bb\mu\mu$ and $bb\tau\tau$ channels using the full Run 2 integrated luminosity of 138 fb^{-1} for Type II (*left*), Type III (*middle*), and Type IV (*right*) 2HDM+S in the $\tan \beta$ vs. m_a phase space. The contours (*dashed black*) correspond to branching fractions of 100% and 16%, where 16% is the combined upper limit on Higgs boson to undetected particle decays from previous Run-2 results. All points inside the contour are allowed within that upper limit. Linear extrapolation has been used between different points on the figures [45].

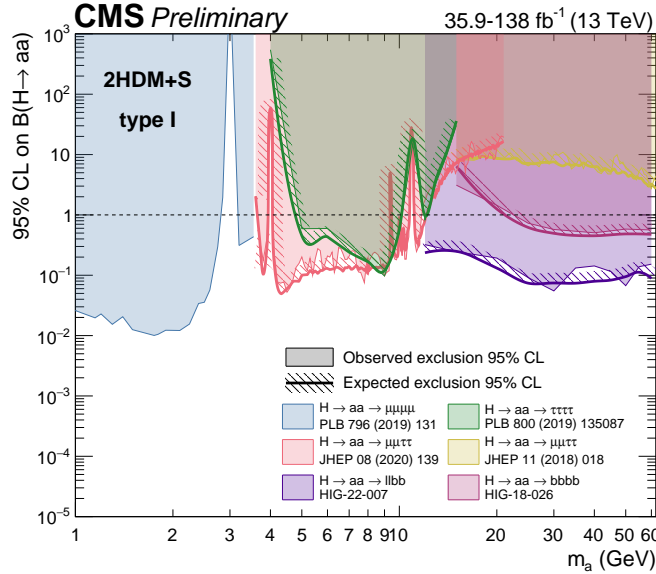


Figure 10.8: Summary plot of current 95% limits on the branching ratio of the 125 GeV Higgs boson to two pseudoscalars, normalized to the Standard Model Higgs production cross-section, $\frac{\sigma(h)}{\sigma_{\text{SM}}} \times B(h \rightarrow aa)$ in the 2HDM+S type I scenario performed with data collected at 13 TeV [102]. Results from different final states studied at CMS are overlaid on this figure: $\mu\mu\mu\mu$ (blue), $\tau\tau\tau\tau$ (green), boosted $2\mu 2\tau$ (red), resolved $2\mu 2\tau$ (yellow), $bbbb$ (magenta), and the combined result for $\ell\ell bb$ ($\ell = \mu, \tau$) (purple).

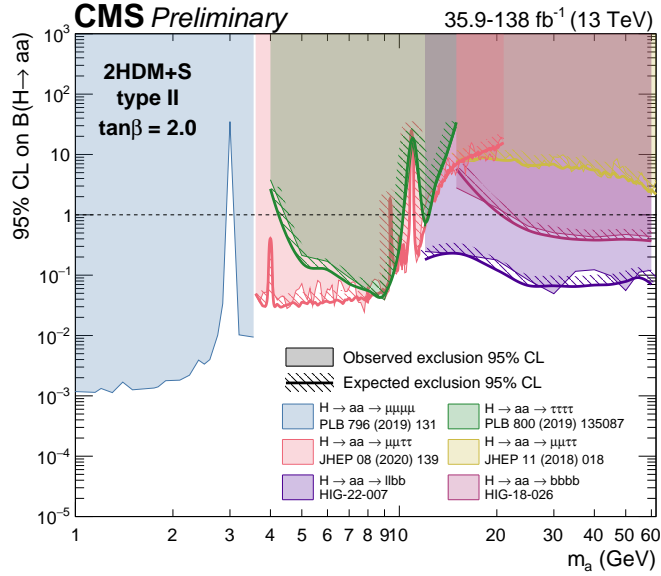


Figure 10.9: Summary plot of current observed and expected 95% CL limits on the branching ratio of the 125 GeV Higgs boson to two pseudoscalars, normalized to the Standard Model Higgs production cross-section, $\frac{\sigma(h)}{\sigma_{SM}} \times B(h \rightarrow aa)$, in the 2HDM+S type II scenario with $\tan\beta = 2.0$, obtained at CMS with data collected at 13 TeV [102]. Results from different final states studied at CMS are overlaid on this figure: $\mu\mu\mu\mu$ (blue), $\tau\tau\tau\tau$ (green), boosted $2\mu 2\tau$ (red), resolved $2\mu 2\tau$ (yellow), $bbbb$ (magenta), and the combined result for $\ell\ell bb$ ($\ell = \mu, \tau$) (purple).

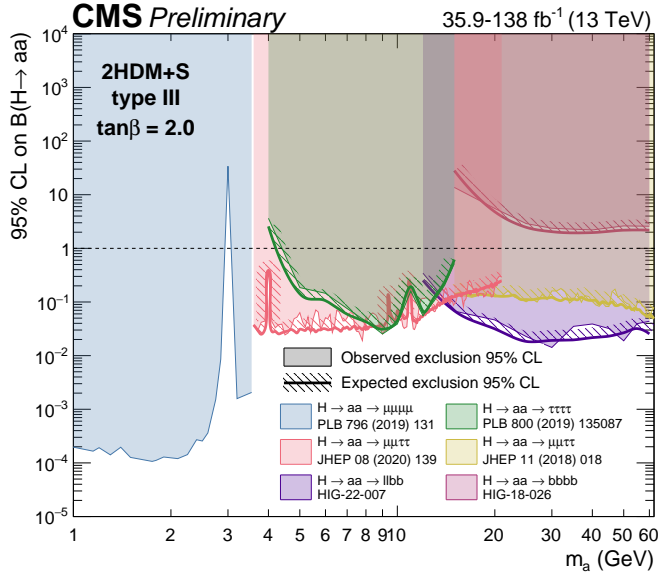


Figure 10.10: Summary plot of current observed and expected 95% CL limits on the branching ratio of the 125 GeV Higgs boson to two pseudoscalars, normalized to the Standard Model Higgs production cross section, $\frac{\sigma(h)}{\sigma_{SM}} \times B(h \rightarrow aa)$ in the 2HDM+S type-III scenario with $\tan \beta = 2.0$, obtained at CMS with data collected at 13 TeV [102]. Results from different final states studied at CMS are overlaid on this figure: $\mu\mu\mu\mu$ (blue), $\tau\tau\tau\tau$ (green), boosted $2\mu 2\tau$ (red), resolved $2\mu 2\tau$ (yellow), $bbbb$ (magenta), and the combined result for $\ell\ell bb$ ($\ell = \mu, \tau$) (purple).

2370 **Chapter 11**

2371 **Asymmetric exotic Higgs decays**

2372 This chapter presents progress towards a search for exotic Higgs decays to two light
2373 scalars with unequal mass ($h \rightarrow a_1 a_2$) final states with bottom quarks and τ leptons,
2374 with plans to interpret the results in the context of Two Real Singlet Models (TRSMs),
2375 described in Section 1.5. Compared to the symmetric decay scenario $h \rightarrow aa$ which
2376 has been studied in multiple final states at CMS with stringent limits set on the
2377 various 2HDM+S scenarios, this asymmetric decay scenario has not been directly
2378 searched for at the CMS experiment. Section 11.1 lists the mass hypotheses of the
2379 new particles a_1 and a_2 that will be studied. Section 11.2 describes the studies on
2380 which channels the analysis will be carried out in. Section 11.3 shows the control
2381 plots produced using the analysis framework that will be used for this analysis.

2382 **11.1 Signal masses**

2383 As discussed in Section 1.5, $h \rightarrow a_1 a_2$ can result in a “cascade” decay if one of the
2384 scalars, a_2 is sufficiently heavy ($m_{a_2} > 2m_{a_1}$). The “non-cascade” case is where the
2385 light scalars decay directly to Standard Model particles.

2386 The mass hypotheses (mass points) (m_{a_1}, m_{a_2}) studied here are:

- *Cascade mass points:* (15, 30), (15, 40), (15, 50), (15, 60), (15, 70), (15, 80), (15, 90), (15, 100), (15, 110), (20, 40), (20, 50), (20, 60), (20, 70), (20, 80), (20, 90), (20, 100), (30, 60), (30, 70), (30, 80), and (30, 90) GeV
- *Non-cascade mass points:* (15, 20), (15, 30), (20, 30), (20, 40), (30, 40), (30, 50), (30, 60), (40, 50), (40, 60), (40, 70), (40, 80), (50, 60), and (50, 70) GeV

Samples were produced using the MadGraph5_aMCatNLO event generator, for each signal mass point in the gluon-gluon fusion (ggF) and vector boson fusion (VBF) production modes of the 125 GeV Higgs boson. In the sample generation, the decays of a to Standard Model particles were specified to be decays to bottom quarks or τ leptons.

11.2 Cascade scenario signal studies

Studies of the signal phenomenology in the cascade scenario were performed to determine the viability of the $4b2\tau$ and/or $2b4\tau$ channels.

Cross sections and branching fractions of the $4b2\tau$ and $2b4\tau$ final states were compared using cross-section predictions provided by the authors of [7]. For an example mass point $m_{a_2} = 80$ GeV, $m_{a_1} = 30$ GeV, the branching fractions to $4b2\tau$ is ten times larger than $2b4\tau$: $B(h \rightarrow a_1 a_2 \rightarrow 3a_1 \rightarrow 4b2\tau) = 0.00857$, vs. $B(h \rightarrow a_1 a_2 \rightarrow 3a_1 \rightarrow 2b4\tau) = 0.00068$. The $4b2\tau$ final state is chosen for this analysis.

In general the four b-flavor jets have low p_T at generator level, as illustrated for example mass points (100, 15) GeV and (40, 20) GeV in Fig. 11.1. The p_T distribution of the sub-leading jet peaks at an energy below 20 GeV, with the third and fourth jets tending to have even softer energies.

An event category with three or more b-tag jets was determined to be infeasible due to low statistics in this category, due to the difficulties in reconstructing the third

2412 and fourth b-flavor jets which have very low transverse momenta p_T . Event categories
 2413 with exactly 1 b-tag jet and ≥ 2 b-tag jets will be used.

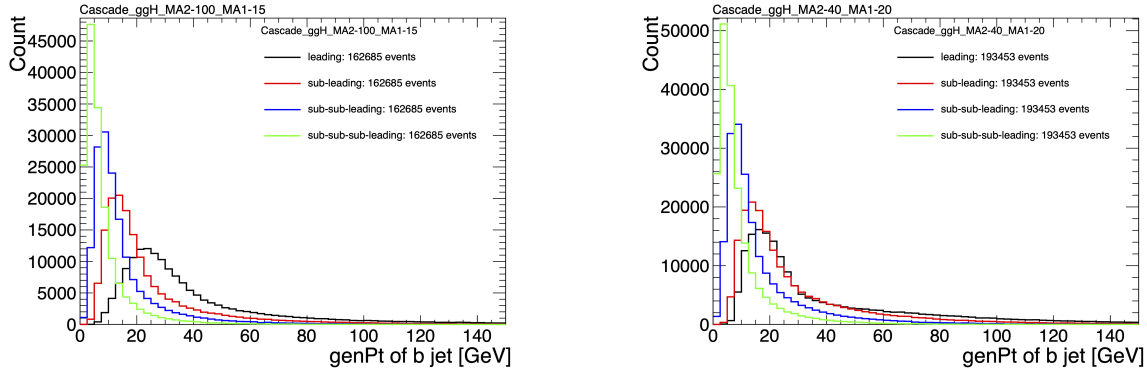


Figure 11.1: Generator-level b-flavor jet transverse momenta p_T , for $h \rightarrow a_1 a_2$ cascade scenario in the $4b2\tau$ final state, for mass hypotheses $(m_{a_1}, m_{a_2}) = (100, 15)$ GeV (*left*) and $(40, 20)$ GeV (*right*). In each plot the generator-level p_T of the leading (*black*), sub-leading (*red*), third (*blue*), and fourth (*light green*) are overlaid.

2414 In the $4b2\tau$ final state, the possibility of the leading and sub-leading b-tag jets
 2415 being sufficiently close in ΔR to require boosted jet reconstruction techniques was
 2416 explored. In the $4b2\tau$ case, the two b-flavor-jets in the generated event that were
 2417 spatially closest in ΔR were considered as one object. This two b-flavor jet object was
 2418 spatially matched in ΔR to the jets reconstructed with the standard AK4 algorithm
 2419 which uses a cone size of $\Delta R = 0.4$. The quality of the p_T resolution (computed as
 2420 $(p_{T,\text{reconstructed}} - p_{T,\text{gen}})/p_{T,\text{gen}}$) and closeness in distance ΔR of the reconstructed jet
 2421 to the nearest generator-level jets, was seen to depend on the absolute and relative
 2422 masses of the light scalars. The best (worst) performance occurred in samples with
 2423 large (small) mass differences between the heavier scalar a_2 and the lighter scalar a_1 ,
 2424 as illustrated for the mass hypotheses (m_{a_1}, m_{a_2}) (100, 15) GeV and (40, 20) GeV in
 2425 Fig. 11.2.

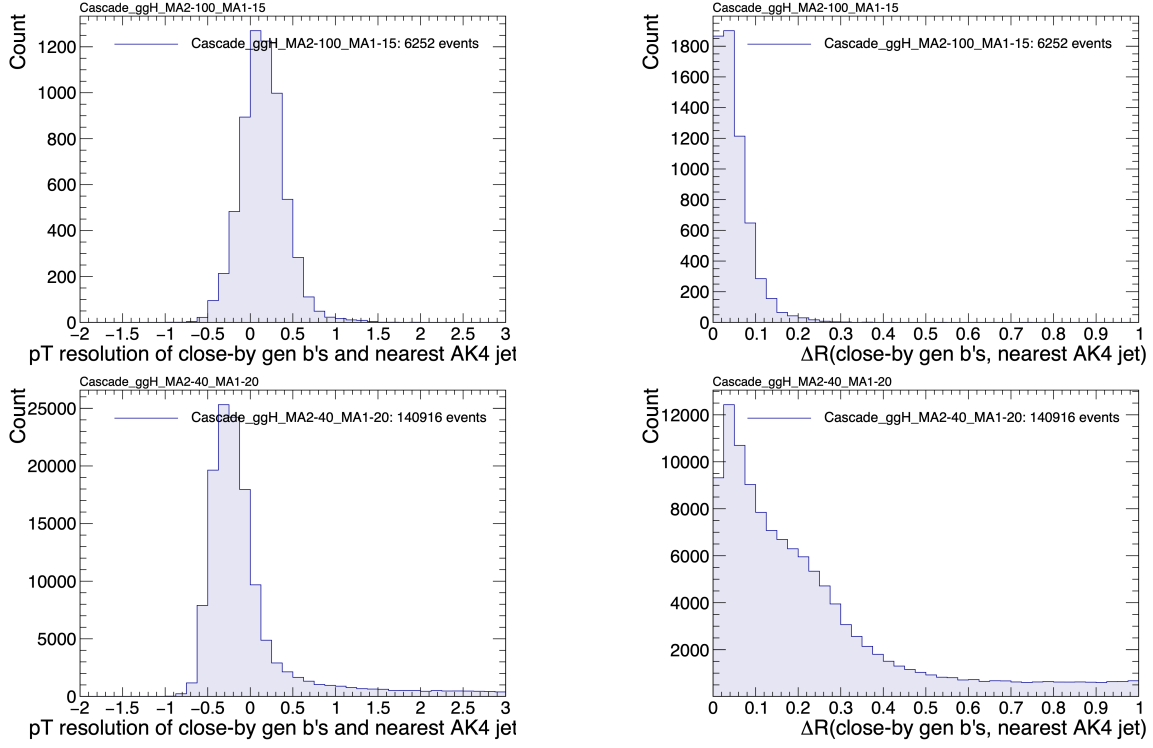


Figure 11.2: Distributions (arbitrary units) of transverse momentum p_T resolution and ΔR between the two closest generator-level b jets, treated as one object, and the nearest reconstructed AK4 jet, for two different $h \rightarrow a_1 a_2$ mass hypotheses (m_{a_1}, m_{a_2}) = (100, 15) GeV (top left, top right) and (40, 20) GeV (bottom left, bottom right) in the ggH production of the 125 GeV h . In the (40, 20) GeV mass point, the longer p_T resolution tail (bottom left) indicates that the reconstructed jet underestimates the generator b -flavor jets' energy, and the significant fraction of events with larger ΔR values (bottom right) indicate worse matching.

11.3 Current control plots for $\mu\tau_h$ channel

The $\tau\tau$ states for the $h \rightarrow a_1 a_2$ to $4b2\tau$ analysis will be similar to those studied in $h \rightarrow aa \rightarrow bb\tau\tau$. For the $\mu\tau_h$ channel, histograms of the key kinematic variables are made for data and the sum of the expected backgrounds, which are estimated from Monte Carlo samples, embedded samples, and the data-driven method for estimating jets faking τ_h as described in Chapter 7. Nominal values of the scale factors and event reweighting are applied, as described in Chapter ???. The errors shown in the figures only include statistical errors and only several of the full set of systematic errors (only those associated with the lepton energy scales and τ_h identification efficiency,

2435 described in Sections 5.3.1, 5.3.2, and 5.3.4).

2436 The p_T , η , and ϕ of the leading muon and hadronic tau τ_h , and the di-tau visible
2437 mass m_{vis} and momentum $p_{T,\text{vis}}$, are shown in Fig. 11.3. The p_T , η , and ϕ of the the
2438 leading and sub-leading b-tag jets, and the missing transverse energy magnitude and
2439 azimuthal direction, are shown in Fig. 11.4.

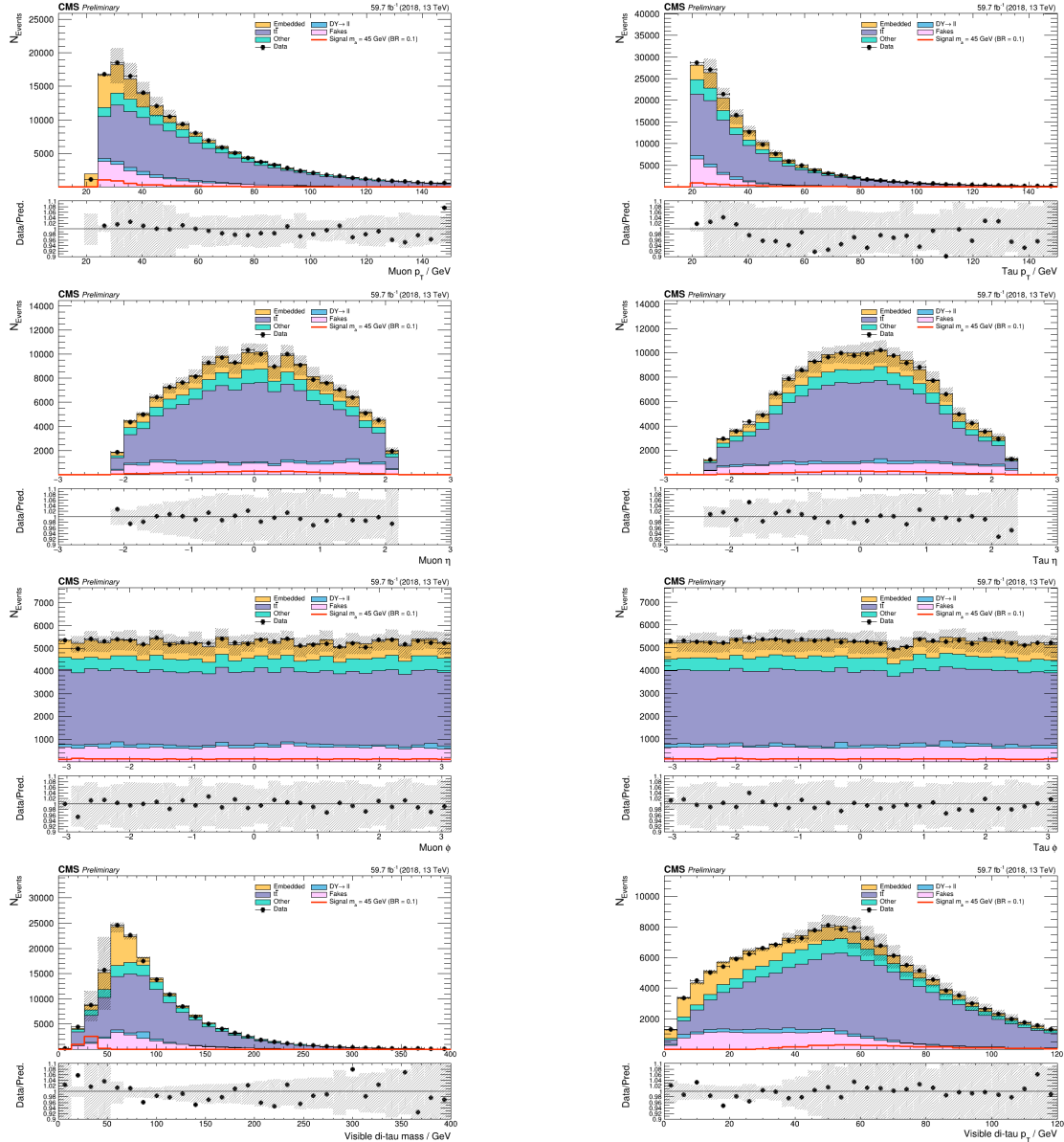


Figure 11.3: Kinematic properties of the leading muon and τ_h in the $\mu\tau_h$ channel: p_T (top row), η (second row), and ϕ (third row). The visible 4-momenta of the muon and τ_h are summed, giving the visible di-tau mass m_{vis} and transverse momentum $p_{T,\text{vis}}$. The errors shown in the figures only include statistical errors and only several of the full set of systematic errors (only those associated with the lepton energy scales and τ_h identification efficiency).

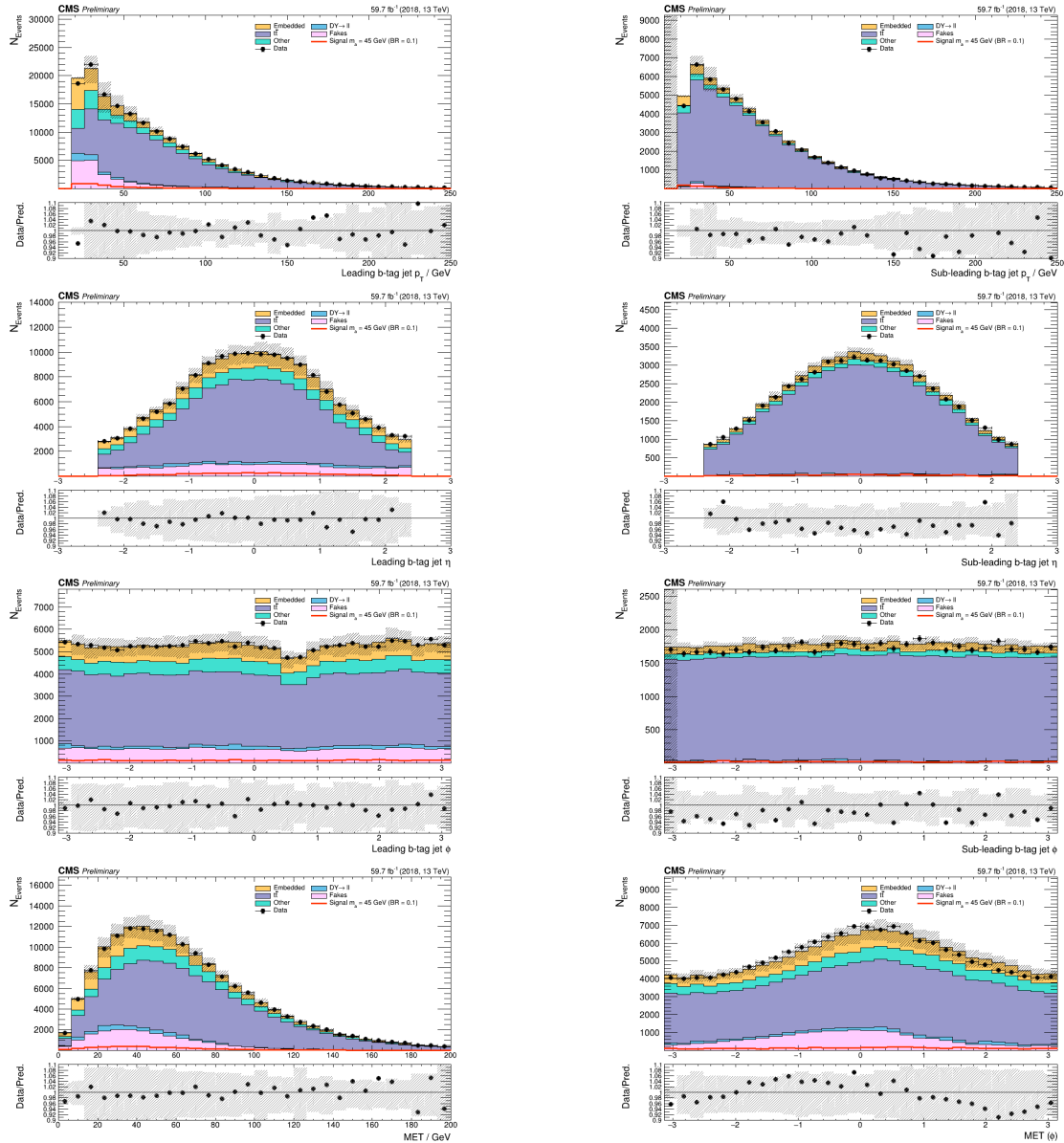


Figure 11.4: Kinematic properties of the leading and sub-leading b-tag jets in the $\mu\tau_h$ final state: jet p_T (*top row*), η (*second row*), ϕ (*third row*), as well as the missing transverse energy magnitude and azimuthal direction (*bottom row*). The errors shown in the figures only include statistical errors and only several of the full set of systematic errors (only those associated with the lepton energy scales and τ_h identification efficiency).

²⁴⁴⁰ **Chapter 12**

²⁴⁴¹ **Conclusion and outlook**

²⁴⁴² With the discovery of a Higgs boson with mass 125 GeV at the LHC in 2012, the LHC
²⁴⁴³ and CMS physics program has evolved to include the precise characterization of the
²⁴⁴⁴ 125 GeV Higgs boson and searching for evidence of additional Higgs particles in an
²⁴⁴⁵ extended Higgs sector. This thesis presents a direct search at CMS for exotic decays
²⁴⁴⁶ of the Higgs boson with mass 125 GeV in data collected in the years 2016-2018 in
²⁴⁴⁷ proton-proton collisions at center-of-mass energy 13 TeV, to two light neutral scalar
²⁴⁴⁸ particles that decay to two bottom quarks and two tau leptons ($h \rightarrow aa \rightarrow bb\tau\tau$). The
²⁴⁴⁹ results are combined with another search that was performed in the $h \rightarrow aa \rightarrow bb\mu\mu$
²⁴⁵⁰ final state, giving the most stringent limits to date for theories with Two Higgs
²⁴⁵¹ Doublet Models extended with a singlet scalar (2HDM+S), for pseudoscalar masses
²⁴⁵² m_a ranging from 15 GeV to 60 GeV, in a number of 2HDM+S scenarios such as type
²⁴⁵³ II and III with $\tan\beta = 2.0$.

²⁴⁵⁴ As the rich physics program of CMS has set stringent limits on the exotic decay
²⁴⁵⁵ $h \rightarrow aa$, we turn our attention to direct searches for decays to light neutral scalars
²⁴⁵⁶ with potentially unequal mass, $h \rightarrow a_1a_2$, which has not been performed at CMS
²⁴⁵⁷ to date. Preliminary studies on $h \rightarrow a_1a_2$ signals in the Two Real Singlet Model
²⁴⁵⁸ (TRSM) are shown, and work is ongoing to develop the analysis for $h \rightarrow a_1a_2$ in final

2459 states with bottom quarks and tau leptons.

2460 To ensure the continued performance of the CMS detector and to enhance its
2461 data-taking capabilities in the intense pile-up conditions of the Phase-2 upgrade of
2462 the High-Luminosity LHC, upgrades of the Level-1 Trigger are paramount for filtering
2463 the increased data rate of the HL-LHC. This thesis presents work on the standalone
2464 barrel calorimeter algorithm for reconstructing and identifying electron and photon
2465 candidates, using high granularity crystal-level information from the ECAL subdetec-
2466 tor. For Phase-2, the increase in the granularity of information sent from the electro-
2467 magnetic calorimeter to the Level-1 trigger, from energy sums over towers (which are
2468 5×5 in crystals) to crystal-level information, allows for the implementation of a more
2469 sophisticated clustering algorithm that can exploit the fact that genuine electrons
2470 and photons tend to leave energies concentrated a 3×5 window in crystals, and use
2471 shape and isolation information to distinguish genuine electrons and photons from
2472 noise. Electrons and photons are key to characterizing Standard Model processes and
2473 performing searches for new physics, and this represents one of the many upgrades of
2474 the CMS detector in preparation for Phase-2. With the ongoing Run-3 data collecting
2475 period, and wealth of ongoing and scheduled upgrades, there remains an abundance
2476 of directions for detector development and physics at CMS heading into Phase-2 of
2477 the LHC.

²⁴⁷⁸ Bibliography

- ²⁴⁷⁹ [1] Paul H. Frampton. Journeys Beyond the Standard Model. 54(1):52–
²⁴⁸⁰ 52. ISSN 0031-9228. doi: 10.1063/1.1349615. URL <https://doi.org/10.1063/1.1349615>. eprint: https://pubs.aip.org/physicstoday/article-pdf/54/1/52/11109432/52_1_online.pdf.
- ²⁴⁸³ [2] Meinard Kuhlmann. Quantum Field Theory. In Edward N. Zalta and Uri Nodelman, editors, *The Stanford Encyclopedia of Philosophy*. Metaphysics Research
²⁴⁸⁴ Lab, Stanford University, Summer 2023 edition, 2023.
- ²⁴⁸⁶ [3] Steven Weinberg. The Making of the Standard Model. *Eur. Phys. J. C*, 34:
²⁴⁸⁷ 5–13, 2004. URL <https://cds.cern.ch/record/799984>.
- ²⁴⁸⁸ [4] Christopher G. Tully. *Elementary Particle Physics in a Nutshell*. Princeton
²⁴⁸⁹ University Press, Princeton, 2012. ISBN 9781400839353. doi: doi:10.1515/
²⁴⁹⁰ 9781400839353. URL <https://doi.org/10.1515/9781400839353>.
- ²⁴⁹¹ [5] John Ellis. Higgs Physics. In *2013 European School of High-Energy Physics*,
²⁴⁹² pages 117–168, 2015. doi: 10.5170/CERN-2015-004.117.
- ²⁴⁹³ [6] David Curtin, Rouven Essig, Stefania Gori, and Others. Exotic decays of the 125
GeV Higgs boson. *Phys. Rev. D*, 90:075004, Oct 2014. doi: 10.1103/PhysRevD.
²⁴⁹⁴ 90.075004. URL <https://link.aps.org/doi/10.1103/PhysRevD.90.075004>.
- ²⁴⁹⁶ [7] Tania Robens, Tim Stefański, and Jonas Wittbrodt. Two-real-scalar-singlet

- 2497 extension of the SM: LHC phenomenology and benchmark scenarios. *Eur.*
2498 *Phys. J. C*, 80(2):151, 2020. doi: 10.1140/epjc/s10052-020-7655-x.
- 2499 [8] CERN. The history of CERN, 2024. URL <https://timeline.web.cern.ch/timeline-header/89>.
- 2500
2501 [9] R. Schmidt. Accelerator physics and technology of the LHC. In *ROXIE: Routine*
2502 *for the Optimiazation of Magnet X-Sections, Inverse Field Calculation and Coil*
2503 *End Design*, pages 7–17, 1998.
- 2504 [10] J. Vollaire et al. *Linac4 design report*, volume 6/2020 of *CERN Yellow Reports: Monographs*. CERN, Geneva, 9 2020. ISBN 978-92-9083-579-0, 978-92-9083-580-6. doi: 10.23731/CYRM-2020-006.
- 2505
2506
2507 [11] Antonella Del Rosso. Aerial view of the LHC and the four major experiments.
2508 2017. URL <https://cds.cern.ch/record/2253966>. General Photo.
- 2509 [12] ATLAS Collaboration. ATLAS: Detector and physics performance technical
2510 design report. Volume 1. 5 1999.
- 2511 [13] CMS Collaboration. CMS Physics: Technical Design Report Volume 1: Detec-
2512 tor Performance and Software. 2006.
- 2513 [14] L Musa. Conceptual Design Report for the Upgrade of the ALICE ITS.
2514 Technical report, CERN, Geneva, 2012. URL <https://cds.cern.ch/record/1431539>.
- 2515
2516 [15] S. Amato et al. LHCb technical proposal: A Large Hadron Collider Beauty
2517 Experiment for Precision Measurements of CP Violation and Rare Decays. 2
2518 1998.
- 2519 [16] Werner Herr and B Muratori. Concept of luminosity. 2006. doi: 10.5170/
2520 CERN-2006-002.361. URL <https://cds.cern.ch/record/941318>.

- 2521 [17] Olivier S. Brning and Frank Zimmerman. Parameter space for the LHC lu-
2522 minosity upgrade. ISBN 978-3-95450-115-1. URL <https://accelconf.web.cern.ch/IPAC2012/papers/moppc005.pdf>.
- 2523
- 2524 [18] CMS Collaboration. Pileup mitigation at CMS in 13 TeV data. *JINST*, 15(09):
2525 P09018, 2020. doi: 10.1088/1748-0221/15/09/P09018.
- 2526 [19] CMS Collaboration. Measurement of the inelastic proton-proton cross section
2527 at $\sqrt{s} = 13$ TeV. *JHEP*, 07:161, 2018. doi: 10.1007/JHEP07(2018)161.
- 2528 [20] CMS Collaboration. High-Luminosity Large Hadron Collider (HL-LHC): Tech-
2529 nical design report. 10/2020, 12 2020. doi: 10.23731/CYRM-2020-0010.
- 2530 [21] CMS Collaboration. The CMS Experiment at the CERN LHC. *JINST*, 3:
2531 S08004, 2008. doi: 10.1088/1748-0221/3/08/S08004.
- 2532 [22] CMS Collaboration. Particle-flow reconstruction and global event description
2533 with the CMS detector. *JINST*, 12(10):P10003, 2017. doi: 10.1088/1748-0221/
2534 12/10/P10003.
- 2535 [23] V Karimki, M Mannelli, P Siegrist, H Breuker, A Caner, R Castaldi, K Freudens-
2536 reich, G Hall, R Horisberger, M Huhtinen, and A Cattai. *The CMS tracker sys-
2537 tem project: Technical Design Report*. Technical design report. CMS. CERN,
2538 Geneva, 1997. URL <https://cds.cern.ch/record/368412>.
- 2539 [24] The Phase-2 Upgrade of the CMS Tracker. Technical report, CERN, Geneva,
2540 2017. URL <https://cds.cern.ch/record/2272264>.
- 2541 [25] CMS Collaboration. CMS Technical Design Report for the Pixel Detector Up-
2542 grade. 9 2012. doi: 10.2172/1151650.
- 2543 [26] R. L. Workman and Others. Review of particle physics. 2022:083C01. doi:
2544 10.1093/ptep/ptac097.

- 2545 [27] CMS Technical Design Report for the Phase 1 Upgrade of the Hadron Calorime-
2546 ter. 9 2012. doi: 10.2172/1151651.
- 2547 [28] CMS Technical Design Report for the Level-1 Trigger Upgrade. 6 2013.
- 2548 [29] S. Dasu et al. CMS. The TriDAS project. Technical design report, vol. 1: The
2549 trigger systems. 12 2000.
- 2550 [30] Alex Tapper. The CMS Level-1 Trigger for LHC Run II. *PoS*, ICHEP2016:242,
2551 2016. doi: 10.22323/1.282.0242.
- 2552 [31] A. Zabi, F. Beaudette, L. Cadamuro, O. Davignon, T. Romantreau, T. Strebler,
2553 M. Cepeda, J.B. Sauvan, N. Wardle, R. Aggleton, F. Ball, J. Brooke, D. New-
2554 bold, S. Paramesvaran, D. Smith, J. Taylor, C. Foudas, M. Baber, A. Bun-
2555 dock, S. Breeze, M. Citron, A. Elwood, G. Hall, G. Iles, C. Laner, B. Pen-
2556 ning, A. Rose, A. Shtipliyski, A. Tapper, I. Ojalvo, T. Durkin, K. Harder,
2557 S. Harper, C. Shepherd-Themistocleous, A. Thea, T. Williams, S. Dasu,
2558 L. Dodd, R. Forbes, T. Gorski, P. Klabbers, A. Levine, T. Ruggles, N. Smith,
2559 W. Smith, A. Svetek, J. Tikalsky, and M. Vicente. The cms level-1 calorimeter
2560 trigger for the lhc run ii. *Journal of Instrumentation*, 12(01):C01065, jan 2017.
2561 doi: 10.1088/1748-0221/12/01/C01065. URL <https://dx.doi.org/10.1088/1748-0221/12/01/C01065>.
- 2562
- 2563 [32] P. Klabbers et al. CMS level-1 upgrade calorimeter trigger prototype develop-
2564 ment. *JINST*, 8:C02013, 2013. doi: 10.1088/1748-0221/8/02/C02013.
- 2565 [33] CMS Collaboration. The Phase-2 Upgrade of the CMS Data Acquisition and
2566 High Level Trigger. Technical report, CERN, Geneva, 2021. URL <https://cds.cern.ch/record/2759072>. This is the final version of the document,
2567 approved by the LHCC.
- 2568

- 2569 [34] C. Foudas. The CMS Level-1 Trigger at LHC and Super-LHC. In *34th Inter-*
2570 *national Conference on High Energy Physics*, 10 2008.
- 2571 [35] CMS Software Guide. High Level Trigger (TWiki), 2024. URL <https://twiki.cern.ch/twiki/bin/view/CMSPublic/SWGuideHighLevelTrigger>.
- 2573 [36] The Worldwide LHC Computing Grid. 2012. URL <https://cds.cern.ch/record/1997398>.
- 2575 [37] Douglas Thain, Todd Tannenbaum, and Miron Livny. Distributed computing
2576 in practice: the Condor experience. *Concurrency and Computation: Practice*
2577 and Experience, 17(2-4):323–356, 2005. doi: <https://doi.org/10.1002/cpe.938>.
2578 URL <https://onlinelibrary.wiley.com/doi/abs/10.1002/cpe.938>.
- 2579 [38] Alexandre Zabi, Jeffrey Wayne Berryhill, Emmanuelle Perez, and Alexander D.
2580 Tapper. The Phase-2 Upgrade of the CMS Level-1 Trigger. 2020.
- 2581 [39] Technical proposal for a MIP timing detector in the CMS experiment Phase 2
2582 upgrade. Technical report, CERN, Geneva, 2017. URL <https://cds.cern.ch/record/2296612>.
- 2584 [40] CMS Collaboration. Search for exotic decays of the Higgs boson to a pair of
2585 pseudoscalars in the $\mu\mu bb$ and $\tau\tau bb$ final states. *European Physical Journal C*,
2586 2 2024.
- 2587 [41] CMS Collaboration. CMS luminosity measurement for the 2016 data-taking
2588 period. CMS Physics Analysis Summary CMS-PAS-LUM-17-001, 2017. URL
2589 <https://cds.cern.ch/record/2257069>.
- 2590 [42] CMS Collaboration. CMS luminosity measurement for the 2017 data-taking
2591 period at $\sqrt{s} = 13$ TeV. CMS Physics Analysis Summary CMS-PAS-LUM-17-
2592 004, 2018. URL <https://cds.cern.ch/record/2621960>.

- 2593 [43] CMS Collaboration. CMS luminosity measurement for the 2018 data-taking
2594 period at $\sqrt{s} = 13$ TeV. CMS Physics Analysis Summary CMS-PAS-LUM-18-
2595 002, 2019. URL <https://cds.cern.ch/record/2676164>.
- 2596 [44] CMS LUMI Group. CMS Luminosity Public Results (TWiki), 2024. URL
2597 <https://twiki.cern.ch/twiki/bin/view/CMSPublic/LumiPublicResults>.
- 2598 [45] Cécile Caillol, Pallabi Das, Sridhara Dasu, Pieter Everaerts, Stephanie Kwan,
2599 Isobel Ojalvo, and Ho-Fung Tsoi. CMS AN-20-213 (internal): Search for an
2600 exotic decay of the 125 GeV Higgs boson to light pseudoscalars, with a pair of
2601 b jets and a pair of tau leptons in the final state, 2020.
- 2602 [46] J. Alwall, R. Frederix, S. Frixione, et al. The automated computation of tree-
2603 level and next-to-leading order differential cross sections, and their matching
2604 to parton shower simulations. *Journal of High Energy Physics*, 2014(7), July
2605 2014. ISSN 1029-8479. doi: 10.1007/jhep07(2014)079. URL [http://dx.doi.org/10.1007/JHEP07\(2014\)079](http://dx.doi.org/10.1007/JHEP07(2014)079).
- 2606 [47] R. Frederix, S. Frixione, V. Hirschi, et al. The automation of next-to-leading
2607 order electroweak calculations. *Journal of High Energy Physics*, 2018(7), July
2608 2018. ISSN 1029-8479. doi: 10.1007/jhep07(2018)185. URL [http://dx.doi.org/10.1007/JHEP07\(2018\)185](http://dx.doi.org/10.1007/JHEP07(2018)185).
- 2609 [48] S. Agostinelli, J. Allison, K. Amako, et al. Geant4 - a simulation toolkit. 506(3):
2610 250–303. ISSN 0168-9002. doi: 10.1016/S0168-9002(03)01368-8. URL <https://www.sciencedirect.com/science/article/pii/S0168900203013688>.
- 2611 [49] CMS Collaboration. An embedding technique to determine $\tau\tau$ backgrounds
2612 in proton-proton collision data. *JINST*, 14(06):P06032, 2019. doi: 10.1088/
2613 1748-0221/14/06/P06032.

- 2617 [50] CMS Collaboration. Search for neutral MSSM Higgs bosons decaying to a pair
2618 of tau leptons in pp collisions. *JHEP*, 10:160, 2014. doi: 10.1007/JHEP10(2014)
2619 160.
- 2620 [51] CMS Collaboration. Measurements of Higgs boson production in the decay
2621 channel with a pair of τ leptons in proton-proton collisions at $\sqrt{s} = 13$ TeV.
2622 *Eur. Phys. J. C*, 83(7):562, 2023. doi: 10.1140/epjc/s10052-023-11452-8.
- 2623 [52] CMS Collaboration. Reconstruction and identification of tau lepton decays to
2624 hadrons and tau neutrinos at CMS. *Journal of Instrumentation*, 11(01):P01019–
2625 P01019, January 2016. ISSN 1748-0221. doi: 10.1088/1748-0221/11/01/p01019.
2626 URL <http://dx.doi.org/10.1088/1748-0221/11/01/P01019>.
- 2627 [53] CMS Collaboration. Performance of τ -lepton reconstruction and identification
2628 in CMS. *Journal of Instrumentation*, 7(01):P01001, jan 2012. doi: 10.1088/
2629 1748-0221/7/01/P01001. URL <https://dx.doi.org/10.1088/1748-0221/7/01/P01001>.
- 2631 [54] CMS Collaboration. Performance of reconstruction and identification of τ lep-
2632 tons decaying to hadrons and ν_τ in pp collisions at $\sqrt{s} = 13$ TeV. *JINST*, 13
2633 (10):P10005, 2018. doi: 10.1088/1748-0221/13/10/P10005.
- 2634 [55] CMS Collaboration. Identification of hadronic tau lepton decays using a deep
2635 neural network. *JINST*, 17:P07023, 2022. doi: 10.1088/1748-0221/17/07/
2636 P07023.
- 2637 [56] CMS Collaboration. Performance of CMS muon reconstruction in pp collision
2638 events at $\sqrt{s} = 7$ TeV. *Journal of Instrumentation*, 7(10):P10002–P10002,
2639 October 2012. ISSN 1748-0221. doi: 10.1088/1748-0221/7/10/p10002. URL
2640 <http://dx.doi.org/10.1088/1748-0221/7/10/P10002>.

- 2641 [57] CMS Collaboration. Performance of electron reconstruction and selection with
2642 the CMS detector in proton-proton collisions at $\sqrt{s} = 8$ TeV. *Journal of Instru-*
2643 *mentation*, 10(06):P06005, 2015. doi: 10.1088/1748-0221/10/06/P06005. URL
2644 <https://dx.doi.org/10.1088/1748-0221/10/06/P06005>.
- 2645 [58] CMS Collaboration. Identification of b-quark jets with the CMS experiment.
2646 *Journal of Instrumentation*, 8(04):P04013–P04013, April 2013. ISSN 1748-
2647 0221. doi: 10.1088/1748-0221/8/04/p04013. URL <http://dx.doi.org/10.1088/1748-0221/8/04/P04013>.
- 2649 [59] CMS Collaboration. Pileup Removal Algorithms. Technical report, CERN,
2650 Geneva, 2014. URL <https://cds.cern.ch/record/1751454>.
- 2651 [60] CMS Collaboration. CMS Phase 1 heavy flavour identification performance and
2652 developments. 2017. URL <https://cds.cern.ch/record/2263802>.
- 2653 [61] CMS Collaboration. Performance of the DeepJet b tagging algorithm using
2654 41.9 fb^{-1} of data from proton-proton collisions at 13 TeV with Phase 1 CMS
2655 detector. 2018. URL <https://cds.cern.ch/record/2646773>.
- 2656 [62] Lorenzo Bianchini, John Conway, Evan Klose Friis, and Christian Veelken. Re-
2657 construction of the Higgs mass in $H \rightarrow \tau\tau$ Events by Dynamical Likelihood
2658 techniques. *Journal of Physics: Conference Series*, 513(2):022035, jun 2014.
2659 doi: 10.1088/1742-6596/513/2/022035. URL <https://dx.doi.org/10.1088/1742-6596/513/2/022035>.
- 2660 [63] CMS Collaboration. Evidence for the 125 GeV Higgs boson decaying to a pair
2661 of τ leptons. *JHEP*, 05:104, 2014. doi: 10.1007/JHEP05(2014)104.
- 2663 [64] CMS Collaboration. Missing transverse energy performance of the CMS detec-
2664 tor. *JINST*, 6:P09001, 2011. doi: 10.1088/1748-0221/6/09/P09001.

- 2665 [65] Artur Kalinowski. CMS AN-19-032 (internal): Reconstruction of a τ pair in-
2666 variant mass with a simplified likelihood scan, 2019.
- 2667 [66] CMS TAU POG. Tau Physics Object Group: Tau ID Recommendation
2668 For Run 2, 2024. URL <https://twiki.cern.ch/twiki/bin/view/CMS/TauIDRecommendationForRun2>.
- 2670 [67] CMS MUO POG. Muon Physics Object Group: Recommendations, 2024. URL
2671 <https://twiki.cern.ch/twiki/bin/view/CMS/MuonPOG>.
- 2672 [68] CMS MUO POG. Muon Physics Object Group: Reference guidelines and results
2673 for muon momentum scale and resolution in Run II, 2024. URL <https://twiki.cern.ch/twiki/bin/view/CMS/MuonReferenceScaleResolRun2>.
- 2675 [69] CMS HTT working group. Higgs To Tau Tau Working TWiki for the full Run-
2676 2 legacy analysis, 2024. URL <https://twiki.cern.ch/twiki/bin/view/CMS/HiggsToTauTauWorkingLegacyRun2>.
- 2678 [70] CMS ELE POG. Electron Physics Object Group: Recommenda-
2679 tions, 2024. URL <https://twiki.cern.ch/twiki/bin/view/CMS/EgammaRunIIRecommendations>.
- 2681 [71] CMS ELE POG. Electron Physics Object Group: Recommendations for
2682 2016 to 2018 UL, 2024. URL <https://twiki.cern.ch/twiki/bin/view/CMS/EgammaUL2016To2018>.
- 2684 [72] CMS TAU Embedding Group. Tau embedded samples using 2016
2685 data, 2024. URL <https://twiki.cern.ch/twiki/bin/view/CMS/TauTauEmbeddingSamples2016Legacy>.
- 2687 [73] CMS TAU Embedding Group. Tau embedded samples using 2017

- 2688 data, 2024. URL <https://twiki.cern.ch/twiki/bin/viewauth/CMS/>
2689 TauTauEmbeddingSamples2017.
- 2690 [74] CMS TAU Embedding Group. Tau embedded samples using 2018
2691 data, 2024. URL <https://twiki.cern.ch/twiki/bin/viewauth/CMS/>
2692 TauTauEmbeddingSamples2018.
- 2693 [75] Tau Lepton Run 2 Trigger Performance. 2019. URL <https://cds.cern.ch/record/2678958>.
- 2695 [76] CMS Taus High Level Trigger Studies. Tau Lepton Run 2 Trigger Performance
2696 (CMS DP-2019/012), 2024. URL <https://twiki.cern.ch/twiki/bin/view/CMSPublic/HLTTauAllRun2>.
- 2698 [77] Muon HLT Performance with 2018 Data. 2018. URL <https://cds.cern.ch/record/2627469>.
- 2700 [78] Single and Double Electron Trigger Efficiencies using the full Run 2 dataset.
2701 2020. URL <https://cds.cern.ch/record/2888577>.
- 2702 [79] Run II Trigger Performance For $e\mu$ Triggers. 2019. URL <https://cds.cern.ch/record/2687013>.
- 2704 [80] Performance of electron and photon reconstruction in Run 2 with the CMS
2705 experiment. 2020. URL <https://cds.cern.ch/record/2725004>.
- 2706 [81] CMS Collaboration. Performance of the CMS muon detector and muon recon-
2707 struction with proton-proton collisions at $\sqrt{s} = 13$ TeV. *JINST*, 13(06):P06015,
2708 2018. doi: 10.1088/1748-0221/13/06/P06015.
- 2709 [82] Piet Verwilligen. Muons in the cms high level trigger system. *Nuclear
2710 and Particle Physics Proceedings*, 273-275:2509–2511, 2016. ISSN 2405-6014.
2711 doi: <https://doi.org/10.1016/j.nuclphysbps.2015.09.441>. URL <https://www>.

- 2712 [sciencedirect.com/science/article/pii/S240560141500930X](https://www.sciencedirect.com/science/article/pii/S240560141500930X). 37th Inter-
2713 national Conference on High Energy Physics (ICHEP).
- 2714 [83] Muon tracking performance in the CMS Run-2 Legacy data using the tag-and-
2715 probe technique. 2020. URL <https://cds.cern.ch/record/2724492>.
- 2716 [84] V.M. Abazov, B. Abbott, M. Abolins, et al. A novel method for modeling
2717 the recoil in W boson events at hadron colliders. *Nuclear Instruments and*
2718 *Methods in Physics Research Section A: Accelerators, Spectrometers, Detectors*
2719 *and Associated Equipment*, 609(2):250–262, 2009. ISSN 0168-9002. doi: <https://doi.org/10.1016/j.nima.2009.08.056>. URL <https://www.sciencedirect.com/science/article/pii/S0168900209016623>.
- 2722 [85] CMS Collaboration. Search for an exotic decay of the Higgs boson to a pair of
2723 light pseudoscalars in the final state with two b quarks and two τ leptons in
2724 proton-proton collisions at $\sqrt{s} = 13$ TeV. *Phys. Lett. B*, 785:462, 2018. doi:
2725 [10.1016/j.physletb.2018.08.057](https://doi.org/10.1016/j.physletb.2018.08.057).
- 2726 [86] CMS LUMI POG. Luminosity Physics Object Group: Recommendations, 2024.
2727 URL <https://twiki.cern.ch/twiki/bin/view/CMS/TWikiLUM>.
- 2728 [87] The modeling of the top quark p_T (TWiki), 2024. URL <https://twiki.cern.ch/twiki/bin/view/CMS/TopPtReweighting>.
- 2730 [88] CMS BTV group. Methods to apply b-tagging efficiency scale fac-
2731 tors (TWiki), 2024. URL <https://twiki.cern.ch/twiki/bin/view/CMS/BTagShapeCalibration>.
- 2733 [89] CMS Collaboration. Jet energy scale and resolution in the CMS experiment in
2734 pp collisions at 8 TeV. *JINST*, 12(02):P02014, 2017. doi: [10.1088/1748-0221/12/02/P02014](https://doi.org/10.1088/1748-0221/12/02/P02014).

- 2736 [90] Garvita Agarwal. Jet Energy Scale and Resolution Measurements in CMS. *PoS*,
2737 ICHEP2022:652, 2022. doi: 10.22323/1.414.0652.
- 2738 [91] CMS JERC group. Jet Energy Corrections (TWiki), 2024. URL <https://twiki.cern.ch/twiki/bin/view/CMS/JECDataMC>.
- 2739
2740 [92] CMS JERC group. Jet Energy Resolution (TWiki), 2024. URL <https://twiki.cern.ch/twiki/bin/view/CMS/JetResolution>.
- 2741
2742 [93] CMS MUO POG. Muon Physics Object Group: Baseline muon selec-
2743 tions for Run-II, 2024. URL <https://twiki.cern.ch/twiki/bin/view/CMS/>
2744 **SWGuideMuonIdRun2**.
- 2745 [94] CMS ELE POG. Electron Identification Based on Simple Cuts, 2024. URL
2746 <https://twiki.cern.ch/twiki/bin/view/CMSPublic/EgammaPublicData>.
- 2747 [95] Jose Enrique Palencia Cortezon. Single top quark production at CMS. Technical
2748 report, CERN, Geneva, 2018. URL <https://cds.cern.ch/record/2640578>.
- 2749 [96] CMS Collaboration. Measurements of the electroweak diboson production cross
2750 sections in proton-proton collisions at $\sqrt{s} = 5.02$ TeV using leptonic decays.
2751 *Phys. Rev. Lett.*, 127(19):191801, 2021. doi: 10.1103/PhysRevLett.127.191801.
- 2752 [97] CMS Collaboration. A portrait of the Higgs boson by the CMS experiment
2753 ten years after the discovery. *Nature*, 607(7917):60–68, 2022. doi: 10.1038/
2754 s41586-022-04892-x.
- 2755 [98] CMS JERC group. Jet energy scale uncertainty sources (TWiki), 2024. URL
2756 <https://twiki.cern.ch/twiki/bin/view/CMS/JECUncertaintySources>.
- 2757 [99] TOP Systematic Uncertainties (Run 2) (TWiki), 2024. URL <https://twiki.cern.ch/twiki/bin/viewauth/CMS/TopSystematics>.

- 2759 [100] Kyle Cranmer. Practical Statistics for the LHC. In *2011 European School of*
2760 *High-Energy Physics*, pages 267–308, 2014. doi: 10.5170/CERN-2014-003.267.
- 2761 [101] Elham Khazaie, Maryam Zeinali, Hamed Bakhshiansohi, and Abideh Jafari.
2762 CMS AN-21-058 (internal): Search for exotic decays of the Higgs boson to a
2763 pair of new light bosons with two muons and two b jets in the final states at
2764 $\sqrt{s} = 13$ TeV, 2021.
- 2765 [102] CMS Higgs Physics Analysis Group. Summary of 2HDM+S searches at 13 TeV
2766 (Run 2), 2024. URL <https://twiki.cern.ch/twiki/bin/view/CMSPublic/Summary2HDMSRun2>.